STUDIES IN EQUATORIAL AERONOMY

A THESIS
SUBMITTED FOR THE DEGREE OF
DOCTOR OF PHILOSOPHY
OF THE

GUJARAT UNIVERSITY

BY

RAJESH PANDEY

JULY, 1981

PHYSICAL RESEARCH LABORATORY
AHMEDABAD 380 009
INDIA

DEDICATED

TO

THE NEAR AND DEAR ONES

CERTIFICATE

I hereby declare that the work presented in this thesis is original and has not formed the basis for award of any degree or diploma by any university or institution.

Rajesh Pandey
RAJESH PANDEY
(Author)

Certified by

Satya Prakash

SATYA PRAKASH
(Professor-in-charge)

STATEMENT

The work presented in this thesis was carried out by the author at Physical Research Laboratory, Ahmedabad, India, under the guidance of Prof.Satya Prakash.

The studies presented in this thesis can be broadly classified under two heads, namely, theoretical - pertaining to the interaction of gravity wave winds with the ionospheric plasma, and experimental - for the measurements of electron density and electric fields in the equatorial E region. The author has actively participated in designing, fabricating and testing of the payloads for the aforesaid experimental studies. He has also actively participated in the rocket launchings from Thumba Equatorial Rocket Launching Station (TERLS), India.

The electric field payload and the probe system used for the measurements of electric fields uses many novel ideas. The mutual admittance probe (MAP) system used for the measurement of electron density was an improved version of the system used earlier by Prakash and his colleagues.

Although it is generally believed that the low-latitude dynamical processes are controlled by the neutral dynamics, understanding of such a control is far from satisfactory. Thus the theoretical studies were made to assess the effects of the gravity waves in the ionosphere in generating electric field, currents and the ionization irregularities.

Experimental studies were aimed at measuring the ambient parameters, like the electric fields and electron density, of the E region plasma. The electron density measurements included the intercomparison of various techniques for such measurements. Such a comparison has not been attempted earlier. The electron density irregularity measurements by Prakash and his colleagues point toward the presence of small scale electric fields. However, fluctuating vertical electric fields at the equator have not been measured earlier.

The chapterwise breakup of the thesis is as follows. In chapter I, a brief account of various important processes in the upper atmosphere is given. Emphasis is more on the dynamics of the neutrals and charged particles as these are relevant to the studies in the subsequent chapters.

In chapter II, we have developed a three dimensional model for the interaction of gravity wave winds with the ionospheric E region plasma. The interaction effects in localised regions alone are considered in this chapter. The subject of mid latitude and equatorial sporadic E is also reviewed briefly.

Generation and transmission of small scale electric fields due to the gravity wave winds under a variety of situations is discussed in chapter III. Such studies have not been carried out earlier.

The spread F irregularities are discussed in chapter IV. A new mechanism for the production of large scale ionization irregularities is presented, which is based on the results of studies carried out in chapter III.

Chapter V is devoted to the experimental studies for the measurements of electron density and electric fields as discussed above.

Summary of the studies carried out in chapter II through V is given in chapter VI. The direction of future research is also given in this chapter.

ACKNOWLEDGEMENTS

I express, with a deep sense of gratitude, my indebtness to Prof.Satya Prakash who guided me throughout the course of the present work. His everlasting enthusiasm, unassuming and forthright nature, and inspiring outlook is gratefully acknowledged. It is, indeed, a great pleasure and privilege , to have worked with him.

Constant encouragement and interest shown by Prof.B.H. Subbaraya has been invaluable to me. I am grateful to him.

Prof.D. Lal, the Director and Prof.S.P. Pandya, the Dy.Director, have always shown keen interest and given due encouragement throughout. I am grateful to them.

The author has been greatly benefitted by the discussions with Prof.P.K.Kaw. His suggestions are greatly appreciated and acknowledged.

I have been benefitted by the healthy discussions with Mr.T.R.Rao and the members of the Solar and Planetary Physics Group. I thank, heartily, Prof.R.Raghavarao, Prof.R.V.Bhonsle, Dr.S.P.Gupta, Dr.P. Muralikrishna and Mr.Shyamlal for such discussions.

My special thanks are due to Mr.Surendra Pal and

Ms.Veena Prakash for the help in analysing the data. Thanks are also due to Dr.K.S.Rao for his assistance in computer programming.

Messrs R.C.Shah, J.T.Vinchhi, K.S.Modh, Y.B.Acharya, R.N.Misra, S.K.Banerjee, A.K.Goyal, K.S.Patel, R.I.Patel, V.K.Parmar and Ms.Anjana Shah have been very helpful in designing and fabricating the payloads. I sincerely thank them all for their efficient work.

My sincere thanks are due to Mr.V.Sudhakar, Range Manager, Thumba Equatorial Rocket Launching Station, and the members of the Integration Lab. for working tirelessly for the success of the rocket flights.

My friends have always been very kind and helping to me. My special thanks are due to Mahesh and Ashwin for the affection shown by them towards me.

Members of Prof.Satya Prakash family and of Dr.M.Misra (Saurashtra University, Rajkot) have been very kind and affectionate to me. I express my sincerest and heartiest thanks to all of them.

My family is my biggest moral support. I am grateful to my family members for their loving, passionate and warm hearted feelings towards me and also for putting up with my temperament.

Neena came into my life at the fag end of the present work. Her silent approval of me is greatly appreciated.

There are many more who have directly, or indirectly, inspired for and greatly contributed to the completion of this work. I recall them all and thank sincerely for their efforts.

Mr.M.Arvindnath needs a special mention for typing the thesis very efficiently from the handwritten manuscript. I thank him very much for the excellent job. Mr.T.T.Chacko has also assisted me during the course of the work by typing the research publications. I am thankful to him.

Thanks are also due to the P.R.L computing centre and library personnel for their helpful nature.

Rajesh Pandey

Ahmedabad 380 009 (Rajesh Pandey)

CONTENTS

Section B

CHAPTER.I

INTRODUCTION

1.1 Basics of the Earth's Upper Atmosphere:

Curious and inquisitive nature of man has resulted in the investigations of the natural systems. Earth's upper atmosphere has been one of such natural domains subjected to intensive studies. Aeronomy is the branch of physical sciences, pertaining to the study of the upper atmosphere. To systematize such studies, nomenclature and classifications have been made. Thus, the upper atmosphere can be broadly classified as the neutral atmosphere, and the ionized atmosphere - the ionosphere whose physical state is governed, largely, by the ionized species. However, the phenomena associated with neutral dynamics do have a bearing on the ionospheric processes.

The neutral atmosphere has been nomenclatured in terms of temperature variations of the neutrals in different regions and some of these regions overlap the ionospheric regions. Based on the temperature variations, the atmosphere is described in terms of troposphere (3-10 km altitude), stratosphere (10-50 km), mesosphere (50-90 km), thermosphere (90-600 km) and exosphere (600 km and beyond). The boundaries of various regions at different altitude are loosely fixed and these boundaries have been named by putting pause after the name of each region, e.g., mesopause.

Galactic cosmic rays and the ultraviolet and X-ray radiations of the sun penetrate deep into the upper atmosphere and ionize the neutrals. This ionized state is known as plasma which is characterized by the quasi-neutral state in which, number of positively and negatively charged particles is equal beyond a characteristic distance, the Debye shielding length.

Early radio propagation studies of the upper atmosphere revealed the existence of a conducting region in the upper atmosphere, the ionosphere, which has been classified in the D, E and F regions. Various regions although do not have well defined boundaries, are believed to be in the altitude range 50-90 km (D region) 90 to 150 km (E region) and 150 to about 1000 km (F region). Maximum electron density is in the F region, peak value and altitude of which is dependent on the time of the day.

The source of ionization in the D region, below 70 km is mainly cosmic rays which are protons of relativistic velocities. X-rays (2-8 A°) and Ly-α ultraviolet radiations are the source of ionization at higher altitudes (70-90 km). The major ions in the D region are O_2^+ and NO^+.

The E region ionization is mainly due to solar Ly - β (1025.7 A°), extreme ultraviolet radiation (911-1027 A°) and soft X-rays (10-170 A°). The major ions in the E region are NO^+ and O_2^+.

The F region ionization is mainly due to solar ultraviolet radiation (170-911 A°). The major ion is O^+ upto 1000 km during the daytime and upto about 400 km altitude during the nighttime. Above this, H^+ is dominant.

The loss of ionization in the E and F regions is mainly due to recombination. The transport processes contribute to the loss of ionization in one region and gain in the other. In the equilibrium state the loss rate should balance the production rate. Let q be the rate of production of ionization, L be its loss rate due to recombination etc. Transport of the ionization is given by divergence of the flux of the charged particles. If N is the density and $\underline{V}$ is its velocity then, $\nabla \cdot (N \underline{V})$ is the transport term. Hence at a given instant of time, the rate of change of density should satisfy the continuity equation, given by

$$\frac{\partial N}{\partial t} = q - L - \nabla \cdot (N \underline{V}) \qquad (1)$$

This equation is one of the basic equations investigated to describe various phenomena.

Since we are interested in loss processes only in the E and F regions, we shall discuss them in these regions only. Also, only the most important of such processes will be discussed.

In the E and F regions, dissociative recombinations is the most important loss process (Biondi 1964). Only in the upper most F region, radiative recombination is the fastest loss process. These loss processes can be expressed by the equations.

$$\text{Dissociative}: \quad XY^+ + e \xrightarrow{\alpha} X^* + Y^* \qquad (2)$$

$$\text{Radiative}: \quad X^+ + e \xrightarrow{\alpha} X^* \rightarrow X + h\nu$$

Asterisks indicate the excited state of the atoms which lose their energy by radiation or during collisions with other particles.

Since a large proportion of the ions in the E and F regions are originally atomic, dissociative recombination must be preceded by reactions involving formation of molecular ions, like

$$X^+ + YZ \xrightarrow{\gamma} XY^+ + Z \qquad (3)$$

If we assume that N is electron concentration, N_A^+ is atomic ions, N_M^+ of molecular ions and n (M) is the molecular gas concentration, then the continuity equation for electron, atomic and molecular ions is given by (Rishbeth and Garriott, 1969).

$$dN/dt = q - \alpha N N_{M^+} \qquad (4)$$

$$dN_A^+/dt = q - \gamma n(M) N_{A^+} \qquad (5)$$

$$dN_{M^+}/dt = \gamma n(M) N_{A^+} - \alpha N N_{M^+} \qquad (6)$$

charge neutrality requires that

$$N = N_{M^+} + N_{A^+} \qquad (7)$$

In the steady state $d/dt = 0$. If $\beta = \gamma n(M)$ we get,

$$N_{A^+}/N_{M^+} = \alpha N/\beta \qquad (8)$$

Using eqns.(6) and (7) we get,

$$1/q = 1/\beta N + 1/\alpha N^2 \qquad (9)$$

Hence we get,

$$q = \alpha N^2 \quad \text{if} \quad \beta >> \alpha N \quad \text{i.e.} \quad N_{M^+} >> N_{A^+} \qquad (10)$$

$$q = \beta N \quad \text{if} \quad \beta << \alpha N \quad \text{i.e} \quad N_{M^+} << N_{A^+} \qquad (11)$$

As has been pointed out earlier, in the E region, the major ions are molecular (O_2^+ and NO^+), hence the loss of ionization is determined by eqn.(10). While in the F region, where the major ion is O^+, loss is determined by eqn.(12). The coefficient α depends on the temperature and varies slowly with the altitude. Since β depends on the molecular gas concentraction, therefore, decreases rapidly with the altitude. Typical values of α and γ are, of the order of , 10^{-7} cm^3 sec^{-1} and 10^{-11} cm^3 sec^{-1} respectively.

Geomagnetic field plays a very important role in the ionosphere.

The dynamics of the D region ionization is controlled by the neutral dynamics. This is owing to the fact that the collision frequency of the charged particles with the neutrals is so large, in comparison to their gyro-frequency, that they are dragged along with the neutrals. In the E region, the collision frequency of ions with the neutrals is large compared to their gyrofrequency while for electrons, the ratio of electron neutral collision frequency to the electron gyrofrequency is very small. Hence the ion motion is governed by the winds, while the electron motion is governed, largely, by the electric fields. Hence, the E region dynamics is controlled both by the neutral dynamics and by the electric fields. In the F region, the motion of charged particles is mainly controlled by the electric fields.

1.2 Neutral Winds:

Since the ionospheric dynamics is controlled by the neutral dynamics also, we first discuss the neutral dynamics which incorporates the neutral wind motion. Neutral winds of various scale sizes and periodicities are most pertinent to such a description. We first outline various types of neutral winds and waves following Rishbeth and Garriot (1969) and then discuss a few of them in a greater length.

(i) Prevailing Winds

These are the global scale, seasonally varying winds in the mesosphere and lower thermosphere. These are driven by the seasonally varying pressure in-equalities. The averaged winds over a period of a day or two satisfactorily give these winds which are constant over a period of a few months. Typical plots of the prevailing winds have been given by Murgatroyad (1957) and by Grooves (1969) in different altitude ranges.

(ii) Planetary Waves

These waves have periods of a few days and occur in the lower atmosphere. These waves are found to be trapped, entirely, in the lower atmosphere, as a result of the mesospheric winds (Charney and Drazin 1961). However, sometimes, a fraction of their energy reaches higher altitudes (Hines 1963). The long wavelength planetary waves are produced due to the airflow over the continents and by the differential heating over the continents and oceans. The waves of smaller wavelength are generated due to the baroclinic instability.

(iii) Thermospheric Winds

These winds are driven by the pressure in equalities due to daily variations in temperatures. These are found above an altitude of about 120 km. These winds as well may be regarded tidal in nature. These have been formulated by Lindzen (1967), Kohl and King (1967) and Geisler (1966, 1967).

(iv) Tidal Winds

These are produced due to the differential heating of the sun and due to the gravitational forces of the sun and moon. These are global winds with periods related to solar and lunar days.

(v) Internal gravity waves

These are characterised by the periodicities of a few minutes to hours; having vertical wavelengths upto a few tens of km and horizontal wavelength upto thousands of km. The property which is characteristic of these waves is that the energy propagation is in opposition to the phase propagation.

1.3 Atmospheric tides - Observations:

Tidal winds in the upper atmosphere show a high degree of variability and contain contributions from several components (Evans 1978). The oscillations in the upper atmosphere can be excited by the gravitational attraction of the moon and by solar differential heating of the atmosphere. The gravitational attraction of the sun is less effective in their generation. The earth's atmosphere exhibits natural oscillations which have periods, submultiples of the lunar and solar days.

To explain the pressure variations on the ground, in the early days, tidal oscillations were sought (Kelvin 1882 , Lamb 1910). Analysing the surface pressure data, Haurwitz (1956) found that the semidiurnal tidal component was the most dominant. He gave an empirical relation between the observed pressure variations and the semi-diurnal component of the tidal oscillations. He also found solar diurnal and its higher harmonics, and the lunar semi-diurnal periodicities in the data.

As a result of extensive experimental study using various techniques, a great deal of understanding of the phenomena has been reached. However, with the advent of new techniques, a greater variability and complexity is also realised. Several techniques have been employed to infer the existence of tides in different atmospheric regions. Meteorological rockets have been used for such studies in the altitude range of 30-60 km (e.g. Reed 1967, Reed et al 1969) which have revealed a diurnal component. This component was found to have an amplitude of 10 m/sec. at an altitude of 60 km. The altitude region 60-80 km is less explored and the data is almost insignificant (Lindzen 1974). Early studies using meteor radars in the altitude range 80-105 km have been contradicting. While Greenhow and Neufeld (1961) found the semi-diurnal component to be dominant, Elford (1959) found diurnal component to be the most dominant with an amplitude of 20 m/sec.

Meteor radar observations give averaged winds over the whole height range 80-105 km and hence, suffer from a good height resolution. The meteor rate in the region above 100 km is so low that such measurements require high sensitivity of the apparatus . Recent measurements (Glass and Spizzichono 1974 Fellous et al 1975) have shown that the solar semi-diurnal component is the most dominant mode.

Radio reflection measurements of the drift of E region ionization irregularities have been employed for the determination of the E region winds (e.g. Sprenger et al 1971, Lysenko et al 1972). But the basic doubt about these studies has been that, in the presence of propagating waves and electric field induced drifts, whether the technique can be used to determine the neutral winds.

By tracking the luminous vapor trails released from the rockets, the presence of tidal modes has been identified (Rosenberg and Edwards 1964, Murphy et al 1966). Analysis of the release data (Hines 1966) showed the presence of a dominant solar diurnal tide, with an average amplitude of about 40 m/sec reaching its maximum value at 100 km. This was supported by subsequent measurements (Kochanski 1973). It was also found that the diurnal component decreased upto 130 km altitude and then increased. Recent measurements at the equator (Rees et al 1976), however, indicate that the dominant mode is semi-diurnal in the altitude range 90 to 160 km. The vapor release experiments have not been sufficient to resolve all the details as these are limited to twilight periods only.

Incoherent backscatter radar measurements in the mid-latitudes (e.g. Salah et al 1975, Evans and Salah 1975) indicate that, in the lower E region, dominant mode is solar semi-diurnal. Recent measurements at low latitude (at Arecibo) by Wand (1976) indicate that although the dominant mode is semi-diurnal, its amplitude and phase differ from those at the mid latitudes. Measurements with the backscatter radars suffer from the limitation that the good results can be obtained only during the daytime. The number of radars capable of making such measurements, at present, are very few. Therefore, it is desirable to install many of these at suitable locations.

1.3.1 Theory of tidal oscillations:

Assuming the neutral gas to be incompressible and molecular viscosity to be constant, the neutral wind velocity $\underline{W}$ is given by the equation of motion of a fluid as

$$d\underline{W}/dt + 2\underline{\Omega}\times\underline{W} = \underline{g} - \frac{1}{\rho}\nabla p - \nabla\psi + \frac{\mu}{\rho}\nabla^2\underline{W} - \nu_{ni}(\underline{W} - \underline{V}_i) \qquad (12)$$

where

$\underline{\Omega}$ = Angular frequency of the earth

$\underline{g}$ = Acceleration due to gravity

ρ = neutral gas density

p = neutral gas pressure

ψ = scalar potential describing tidal forces

μ = coefficient of molecular viscosity

ν_{ni} = collision frequency of neutrals with the ions

$\underline{V}_i$ = Ion drift velocity

The term $2\underline{\Omega}\times\underline{W}$ represents the coriolis acceleration. The operator

$$d/dt = \partial/\partial t + (\underline{W}\cdot\nabla) \qquad (13)$$

The term $(\underline{W}\cdot\nabla)$ represents the transport of momentum which makes the equation nonlinear. This term is, however, neglected usually. The last term in eqn.(12) is the ion drag term which is usually important above about 150 km.

Below an altitude of about 100 km, the last two terms in eqn.(12) are small and can be neglected. Together with the eqn.(12), the motion of neutral air must satisfy the equation of mass continuity and the equation of state describing the rate of change of temperature to the heat input (Kato, 1966).

The set of equations is solved with the assumption that the tidal oscillations introduce only small perturbations in

$\underline{W}$, ρ, p and temperature, and hence eqn.(12) can be made linear. Neglecting the ellipticity of the earth, the undisturbed atmosphere is assumed to be spherically symmetric and in hydrostatic equilibrium. Hence in the vertical direction $\nabla p/\rho$ term cancels the acceleration due to the gravity. Thus eqn.(12) reduces to

$$\partial \underline{W}/\partial t = -2\,\underline{\Omega}\times\underline{W} - \nabla\Psi \qquad (14)$$

where $\underline{W}$ is solely horizontal. Eqn.(14) can be solved by the method of separation of variables by using $\nabla\cdot\underline{W}$ as the dependent variable expressed as

$$\nabla\cdot\underline{W} = \sum_{m}\sum_{n} R_{mn}(r)\;\Theta_{mn}(\theta)\;\exp\left\{im\left(\frac{2\pi t}{\tau}+\phi\right)\right\} \qquad (15)$$

where $R_{mn}(r)$ is the tide amplitude as function of r, the radial distance from the centre of the earth, $\Theta_{mn}(\theta)$ is the tide amplitude as a function of co-latitude θ, τ is the length of the day and ϕ is the longitude. Θ_{mn} is known as Hough function, expressible in terms of Legendre polynomials. The function Θ_{mn} has ($|n| - m$) modes between the poles (save m = 1 case). A reversal of sign of amplitude implies a 180° change of phase. The oscillations must be periodic in t and ϕ and the modes with m = 1, 2, 3 etc, denote the diurnal, semi-diurnal ter-diurnal etc, oscillations respectively.

The divergence of horizontal velocity is related to the temperature and pressure fluctuations generated by tides and hence, these quantities may also be represented as a sum of solutions as in eqn.(15). When the method of separation of variables is applied to solve eqn.(14), an eigen value equation is obtained in which, the eigen values h_{mn} have the dimensions of length, termed as equivalent depth. Thus the vertically propagating waves due to the tides have wavelength given by

$$k^2_{mn} = \frac{1}{H h_{mn}} \left\{ \frac{(\gamma - 1)}{\gamma} + \frac{dH}{dz} \right\} - \frac{1}{4H^2} \qquad (16)$$

where H = scale height of the atmosphere

γ = ratio of specific heats

z = altitude

The amplitude of these waves would grow exponentially because in the atmosphere the density decreases exponentially. To conserve the energy, the amplitude must grow in the same fashion.

The theory of tides has been discussed in great detail by Chapman and Lindzen (1970). Tarpley (1970), and Volland and Mayr (1972 a,b) have developed an analytical method of studying propagation of tides upward in the thermosphere. Volland and Mayr (1977) have also reviewed the subject in detail. Detailed computations including the effects of background wind, temperature variation with the altitude, ion drag and viscosity have been carried out using the full wave solutions (e.g. Lindzen and Hong 1974, Forbes and Garrett 1976). Numerical results have been obtained by Mayr and Harris (1977).

In the lower most part of the thermosphere (100-125 km), solar heating due to EUV and X-ray radiations appears to be less important in establishing winds than upward propagating energy from the mesosphere in the form of tides. Above about 130 km, the amplitude of pressure fluctuations induced by the upward propagating tides is diminished as a result of viscous dissipation of the wave energy and the solar heating becomes more important. This source gives rise to winds that are weakly coupled to those produced at the lower altitudes by the upward propagating tidal energy via the dynamo effects (Lindzen 1967, Murata 1968, Hines 1974). This conslusion is supported by the observations (e.g. Kochanski 1973) as noted earlier.

1.4 Gravity Waves:

Radar observations of drifting meteor trails (Greenhow and Neufeld 1956) used for the measurements of thermospheric winds showed an irregular scattering of speeds about the smooth tidal oscillations. Prior to 1960, these irregular variations were thought to be due to the turbulence. With the fixing of the turbopause level, need for another mechanism to generate the irregular wind variations was realised. Hines (1960) gave the first theoretical explanation to these in terms of the internal atmospheric gravity waves. Hines (1960) has discussed a number of observations to reach at the conclusion that for the small scale irregular variations in the thermospheric winds, a wave interpretation is essential. He developed the theory on the following assumptions.

(i) In the absence of the waves, the atmosphere is stationary.

(ii) The atmosphere is uniform in both temperature and composition.

(iii) Super imposed variations have only perturbation magnitudes.

(iv) Since the waves are of scale sizes smaller than the earth's radius, the coriolis term is negligible.

(v) The perturbations occur adiabatically.

(vi) The effects of molecular viscoisity and heat conduction are negligibly small.

Thus the basic quantities p, ρ, $\underline{W}$ can be expressed as

$$\begin{aligned} p &= p_0 + p_1 \\ \rho &= \rho_0 + \rho_1 \\ \underline{W} &= \underline{W}_0 + \underline{W}_1 \end{aligned} \qquad (17)$$

where the quantities with subscript zero are unperturbed values and the quantities with subscript 1 are perturbation in them. By choosing a reference frame that moves with the neutral wind, we have $\underline{W} = 0$. The various perturbed magnitudes are expressed as

$$\frac{p_1}{p_0 P} = \frac{\rho_1}{\rho_0 R} = \frac{W_{1h}}{h_0} = \frac{W_{1z}}{Z} = A_0 \exp\{i(\Omega t - k_h h - k_z z\} \qquad (18)$$

The terms P, R, h_0 and Z are the polarization terms which determine the phase relationship between various quantities. K's are the complex wave numbers which determine the amplification or attenuation of the wave. h denotes the horizontal direction of phase propagation, and z is upward. The basic equations to be solved are the equation of motion, equation of mass continuity and the adiabatic equation of state, which are

$$\frac{\partial \underline{W}}{\partial t} = -\frac{1}{\rho}\nabla p + \underline{g}$$
$$\frac{\partial p}{\partial t} = c^2\left(\frac{\partial \rho}{\partial t} + \underline{W}\cdot\nabla\rho\right) \tag{19}$$
$$\partial\rho/\partial t = -\nabla\cdot(\rho\underline{W})$$

where C is the velocity of sound in the medium. Linearlising these equations one gets a matrix equation which gives the following dispersion relation

$$\Omega^4 - \Omega^2 c^2 (k_h^2 + k_z^2) + (\gamma-1) g^2 k_h^2 + i\Omega^2 \gamma g k_z = 0 \tag{20}$$

since the attenuation or growth of the wave should occur either in the horizontal direction or in the vertical, both K_h and K_z cannot be complex. Assuming that there is no variation in the horizontal direction, K_h is real i.e. $K_h = k_h$. The real part of eqn.(20) is then given by,

$$\Omega^4 - \Omega^2 c^2 \{k_h^2 + k_z^2 - (I_m k_z)^2\} - \Omega^2 \gamma g I_m(k_z) + (\gamma-1) g^2 k_h^2 = 0 \tag{21}$$

Imaginary part is given by

$$-\Omega^2 \gamma g R_e(k_z) - 2\Omega^2 c^2 R_e(k_z) I_m(k_z) = 0 \tag{22}$$

If $\Omega \neq 0$, it is implied from eqn.(23) that either

$$R_e(k_z) = 0 \tag{23}$$

$$\text{or} \quad I_m(k_z) = \gamma g/2c^2 = 1/2H \tag{24}$$

where $$c^2 = \gamma g H \tag{25}$$

If $R_e(k_z) = 0$, it implies that waves have no vertical phase variation. Only exponential growth or decay is accompanied which is characteristic of the surface waves and the evanescent waves.

The waves which have $\mathrm{Im}(k_z) = 1/2H$ can be grouped into two separate classes. The one which have frequencies greater than the sound waves in the medium are known as the acoustic waves. The lower frequency cut off of the acoustic waves is given by

$$\Omega_a = \gamma g / 2H = c / 2H \tag{26}$$

The other set of waves have the Brunt-Vaisala frequency as the cut off frequency, given by

$$\Omega_B^2 = (\gamma - 1) g^2 / c^2 \tag{27}$$

These waves are the low frequency long period waves and are commonly known as the internal gravity waves. For these waves, it is found that the vertical phase and group velocity are oppositely directed. The group velocity represents the direction of energy flow. Hence, the phase propagation is in opposition to the energy propagation for these waves.

The acoustic gravity waves have periods less than about 4.4 minute while the gravity waves have periods greater than 4.9 minute. Hines (1960) has given the range of scale sizes associated with the gravity waves in different regions. At the E region heights, the dominant vertical scale size is about 10 km while the horizontal scale size could be more than an order of magnitude larger.

Dissipation of gravity waves has been discussed by Hines (1960) and in detail by Pitteway and Hines (1963). The minimum vertical scale size, as predicted theoretically

(Hines 1964) are nearly consistent with the observed one (e.g.Zimmerman 1964). Reflection and ducting of the gravity waves due to the temperature gradients and the windshears has been discussed by Pitteway and Hines (1965). Detailed account of the gravity waves has been given by Hines and Colleagues (1974), and in the review articles (e.g. Rivah 1969, Francis 1975).

Direct observations on the gravity waves in the upper atmosphere have not been satisfactory. Very few observations on the power spectrum of the gravity waves are available. Notable power spectrum calculations have been made by Spizzichino (1970). He found that the average power spectrum decreased with increasing Ω in a fashion $\Omega^{-\delta}$; where δ was 0.82 at 90 km and 0.47 at 100 km. Incoherent radar observations in the equatorial lower atmosphere have also shown the existence of gravity waves (Rastogi and Bowhill 1975). By observing the airglow emission from OH clouds, Moreels and Herse ('77)have indicated the existence of gravity waves in the atmosphere. Physical Research Laboratory has also undertaken such a programme to photograph these emissions using Space Lab (an ESA-NASA joint venture) under ISRO (India) - CNES (France) collaborative programmes.

The effects of gravity waves on the ionosphere are manifested in several ways. It is now believed that the travelling ionospheric disturbances are due to the gravity waves (e.g. Hines 1960, Francis 1973). Ionization perturbation due to the passage of a gravity wave have been studied by several authors (e.g.Hooke 1969, Beer and Moorcraft 1972). Gravity waves have been invoked to explain the large scale size irregularities in the equatorial F region (Rottger 1976, Klostermeyer 1978, Booker 1979). Their effects on the equatorial E region have also been studied (Kato 1973, Anandarao et al 1977, Prakash and Pandey 1979). Midlatitude sporadic E phenomena has been accounted for by using the shears in the gravity wave winds (Whitehead, 1961; Hines 1964). However, the electrodynamic effects due to the gravity wave winds have not been satisfactorily understood especially in the equatorial E region.

1.5 Dynamics of Charged Particles:

It has been pointed out earlier that the motion of a charged particle in the ionosphere is governed by the electric and magnetic fields and by the neutral dynamics. We have already given an account of the neutral dynamics. The electric fields in the ionosphere can be of two types, the large scale and the small scale. While the large scale electric fields decide the global current pattern, the small scale fields contribute to the localised phenomena. Generation of large scale electric fields can be explained on the basis of the dynamo theory which we will discuss later.

Besides the electric and magnetic fields and the neutral air motion, the plasma diffuses under the action of gravity and due to the gradients in its own partial pressure. The electrical forces keep the diffusion of both types of charged particles with the same velocity, resulting in ambipolar diffusion which, due to the collisions of charged particles with the neutrals is mostly along the geomagnetic field lines.

The equation of motion for ions and electrons in the equilibrium state can be written as (Rishbeth and Garriott 1969)

$$m_i \frac{dV_i}{dt} = 0 = m_i \underline{g} - \frac{1}{N_i} \nabla (N_i k T_i) + e(\underline{E} + \underline{V}_i \times \underline{B}) - m_i \nu_{in} (\underline{V}_i - \underline{W}) - m_i \nu_{ie} (\underline{V}_i - \underline{V}_e) \quad (28)$$

$$m_e \frac{dV_e}{dt} = 0 = m_e \underline{g} - \frac{1}{N_e} \nabla (N_e k T_e) + e(\underline{E} + \underline{V}_e \times \underline{B}) - m_e \nu_{en} (\underline{V}_e - \underline{W}) - m_e \nu_{ei} (\underline{V}_e - \underline{V}_i) \quad (29)$$

where Ni = Ne = N = plasma density

T = Temperature of the particle

k = Boltzmann's constant

m = mass of the charged particle

e = charge of the particle

V = velocity of the charged particle

ν = collision frequency between particles (i.e. ν_{in} denotes collisions of ions with the neutrals etc.)

1.6 Conductivities:

Eqns.(28) and (29) can be solved using simplifying assumptions (viz. neglecting terms with gravity, partial pressure). The simplified equations can then be solved for

$\underline{V}_i$ and $\underline{V}_e$ to give current, given by

$$\underline{J} = Ne(\underline{V}_i - \underline{V}_e) \tag{30}$$

Using Ohm's law we get

$$\underline{J} = \underline{\underline{\sigma}} \cdot \underline{E}^W \tag{31}$$

where $\underline{\underline{\sigma}}$ is the tensor conductivity, and $\underline{E}^W$ is the total electric field given by

$$\underline{E}^W = \underline{E} + \underline{W} \times \underline{B} \tag{32}$$

The conductivity is anisotropic due to the presence of the geomagnetic field.

Eqn.(31) can be solved in a chosen coordinate system (Fejer 1965) to obtain the relationship between various current components and the total electric field in that direction. These relations give the components of the tensor conductivity, which are σ_0, σ_P and σ_H, in the direction parallel to the magnetic field, in the direction of the electric field $\underline{E}$ and in the $\underline{B} \times \underline{E}$ direction, respectively. The conductivity components are given by

$$\begin{aligned} \sigma_0 &= \frac{Ne}{B}(1/R_i + 1/R_e) \\ \sigma_P &= \frac{Ne}{B}\left\{ R_e/(1+R_e^2) + R_i/(1+R_i^2) \right\} \\ \sigma_H &= \frac{Ne}{B}\left\{ 1/(1+R_e^2) - 1/(1+R_i^2) \right\} \end{aligned} \tag{33}$$

where

$$\begin{aligned} R_i &= \nu_i / \Omega_i \\ R_e &= \nu_e / \Omega_e \end{aligned} \tag{34}$$

Ω being the gyrofrequency of the charged particle and

$$\begin{aligned} \nu_i &= \nu_{in} + \nu_{ie} \\ \nu_e &= \nu_{en} + \nu_{ei} \end{aligned} \tag{35}$$

In terms of conductivity components of eqn.(33), $\underline{\underline{\sigma}}$ is expressed as

$$\underline{\underline{\sigma}} = \begin{pmatrix} \sigma_P & -\sigma_H & 0 \\ \sigma_H & \sigma_P & 0 \\ 0 & 0 & \sigma_0 \end{pmatrix} \qquad (36)$$

1.7 Dynamo Theory:

The dynamo theory was proposed by Stewart (1882) to account for the daily variations of the geomagnetic field, observed on the ground. The dynamo theory was developed, quantitatively, by Schuster (1908). Despite the difficulties associated with the theory, the basic mechanism proposed is on a sound footing. We give a brief account of the theory, based on the lucid treatment given by Rishbeth and Garriott (1969).

At latitudes above about 35^o, tidal winds in the ionosphere blowing horizontally across the vertical component of the earth's magnetic field, generate currents which tend to flow at certain longitudes towards the geomagnetic equator and away from it along other meridiaus. Equivalently, a wind $\underline{W}$ blowing across the geomagnetic field induces a field $\underline{W} \times \underline{B}$ which in turn drives a current $\underline{\underline{\sigma}}(\underline{W} \times \underline{B})$. The current produced by the wind alone need not satisfy $\nabla\cdot\underline{J}=0$ everywhere at a given instant of time. At any point where $\nabla\cdot\underline{J}\neq 0$, the charges accumulate to produce a polarization field $\underline{E} = -\nabla\phi$, which modifies the current flow until $\nabla\cdot\underline{J}=0$ is satisfied. At low latitudes the closure of current system is provided by flow along the parallels of the latitudes. The modified current, which is non divergent and horizontal, is expressed in terms of the layer conductivity tensor $\underline{\underline{\sigma}}'$ and the total electric field $(\underline{E} + \underline{W} \times \underline{B})$, by

$$\underline{j}' = \underline{\underline{\sigma}}' \cdot (\underline{E} + \underline{W} \times \underline{B}) \qquad (37)$$

The above mechanism of generating fields and currents is termed dynamo theory because the mechanism is similar to that of dynamo, in which the earth it self is a magnet, the moving air is the armature, of which windings are represented by the convected conducting ionosphere.

The dynamo field (which is large scale field) can be mapped into the F region through the conducting lines of geomagnetic field. This field causes the plasma to drift in the F region. The drift of plasma in the F region is analogous to an electric motor running without a load. Thus E region is the "dynamo region" and F region is the "motor region".

There is a "motor effect" in the dynamo region itself, since the currents also flow in the earth's magnetic field. This might be said to be the result of forces analogous to the "armature action" in a commercial dynamo.

The dynamo theory, as proposed above, is over simplified and hence idealized. There are numerous difficulties, both in the assumptions and the results obtained, with the theory, The theory has been improved upon and suggestions have been made to make it compatible with the observations (e.g.Murata, 1974; Stening 1970; Schieldge et al 1973; Lindzen and Forbes, 1976; Richmond et al 1976 etc).

1.8 Equatorial Electrojet:

Since the vertical extent of the conducting E layer is limited, Baker and Martyn (1953) have used the height integrated layer conductivities to describe the theory of magnetic variations. A horizontal electric field $\underline{E}$ will give rise to an electric current $\underline{\underline{\sigma}} \cdot \underline{E}$ which will have an east-west as well as a vertical component. Since the current cannot flow in the vertical direction, the charges will accumulate at the boundary giving rise to a polarization field. This polarization field, in turn, modifies the horizontal current. By imposing the condition of zero vertical current, the conductivity tensor reduces to a 2 x 2 matrin given by

$$\underline{\underline{\sigma}}' = \begin{pmatrix} \sigma_{xx} & \sigma_{xy} \\ \sigma_{xy} & \sigma_{yy} \end{pmatrix} \qquad (38)$$

where x and y are due magnetic south and east respectively and

$$\sigma_{xx} = \frac{\sigma_0 \, \sigma_p}{(\sigma_0 \sin^2 I + \sigma_p \cos^2 I)}$$

$$\sigma_{xy} = \sigma_0 \sigma_H \sin I / (\sigma_0 \sin^2 I + \sigma_p \cos^2 I) \qquad (39)$$

$$\sigma_{yy} = \sigma_H^2 \cos^2 I / (\sigma_0 \sin^2 I + \sigma_p \cos^2 I)$$

I is the dip angle. At the equator we get,

$$\sigma_{xx} = \sigma_0 \,, \quad \sigma_{xy} = 0 \qquad (40)$$

$$\sigma_{yy} = \sigma_H^2 / \sigma_p + \sigma_p = \sigma_3$$

Thus the east-west conductivity at the equator is very large, equal to σ_3, the cowling conductivity. In the electrojet region, σ_3 is comparable to σ_0. The highly conducting strip along the magnetic equator is known as the equatorial electrojet, which is confined to a width where

$$\sigma_0 \sin^2 I << \sigma_p \cos^2 I \qquad (4.1).$$

Suguira and Cain (1966) developed the electrojet model based on assumption of the Layer conductivity model, viz, zero vertical current and the absence of electric field in the north south direction. It was shown by Untiedt (1967) that these assumptions were inconsistent as they lead to strongly divergent currents in the north-south direction. The model of Untiedt (1967) took into account, the meridional currents. This model was further extended by Suguira and Poros (1969). Richmond (1973) developed a numerical model of the equatorial electrojet.

The equatorial electrojet has been subject of extensive studies. A host of electron density irregularities are known to be associated with the equatorial electrojet and the equatorial E and F regions. Generation mechanisms of these are not, as yet, fully understood; as will be discussed in the following chapters.

CHAPTER II

INTERACTION OF GRAVITY WAVES WITH THE IONOSPHERIC E REGION PLASMA AND GENERATION OF ELECTRIC FIELDS AND CURRENTS.

2.1 Introduction:

This chapter is devoted to the studies of electron density irregularities in the E region, with an emphasis on the equatotial E region irregularities. Experimental observations on the irregularities are discussed in the light of theoretical explanations put forward and their deficiencies are pointed out. The main emphasis in the chapter is on the three dimensional model, developed to study the effects of gravity wave winds on the E region plasma. The sectionwise breakup of this chapter is as follows.

Experimental and theoretical studies on the temperate zone sporadic E are discussed in section 2.2 .

Section 2.3 is on the equatorial sporadic E in which, observations and theoretical explanation to these observations are discussed.

In section 2.4, earlier studies on the effects of the gravity wave winds on the equatorial E region are briefly discussed.

In section 2.5, a three dimensional model of the interaction of the gravity wave winds with the E region plasma is developed, detailing its basic concept and the theory.

Section 2.6 details the results of these studies in which electric field, currents and the plasma convergence rates are calculated. These results are discussed to bring out several new features of these studies.

In section 2.7, the conclusions of the studies carried out in this chapter are given.

The E region has been a subject of active study from the early days of ionospheric research. Ground based ionosonde were used to determine the electron density profiles in the E region. Appleton (1930) using the ground based ionosonde observed the abnormal layers in the electron density around 100 km in the nighttime. Later studies showed the presence of dense layers or patches of ionization in the E region, at heights of about 100-120 km, which didnot relate to the normal daytime layers. Because of the irregularity of its behaviour, this phenomenon has been known as sporadic E or Es. Sometimes E_s appears as sheets of ionization blanketing the overlying F layer on the ionograms. At other times it may be patchy and partially transparent. Much of statistical data has been accumulated over the past decades on various aspects of the sporadic E phenomena. These studies have helped in establishing that E_s is a world wide phenomena. Smith (1957) has classified E_s into equatorial, temperate and auroral zone type, although the boundaries are not so clearly defined. It is now believed that the causative mechanisms of the sporadic E, in the three different zones are different. A detailed review of the sporadic E phenomena has been given by Whitehead (1970).

2.2 Temperate Zone Sporadic E

Using the groundbased ionosonde and radars the occurrence statistics of the sporadic E, that is, its variation with the time of the day, season and sunspot cycle; and various features like the height, its variation with the strength of the magnetic field etc; have been studied extensively. The altitude region of their occurrence has been studied using the in-situ techniques (Pfister and Ulwick 1950; Aono et al 1961; Seddon 1962; Aurby et al 1966; Smith 1966; Bowhill 1966; Smith and Mechitly 1972).

The Wind Shear Theory

Several theories have been proposed to explain the formation of sporadic E layers. Dungey (1956, 1959) proposed that the north south shears in the north south wind can compress the ionization to give the appearance of a layer. This mechanism was found to be ineffective in the E region and hence given up.

Whitehead (1961) proposed that a height varying east west wind, that is, the vertical shears in the east west wind, can redistribute the E region ionization and produce the ionization layers.

In the E region, the neutral wind drags the ions along with it because the collision frequency of ions with the neutral (ν_{in}) exceeds the ion gyrofrequency (Ω_i). The ions experience a Lorentz force $\underline{W} \times \underline{B}$, where $\underline{W}$ is the neutral wind velocity and $\underline{B}$ is the geomagnetic field, in the vertical direction. Under the combined action of these forces, the ions move in a vertical direction determined by $\theta = \tan^{-1}(\Omega_i/\nu_{in})$. If the wind changes the direction with the altitude, then the ions are compressed within the shear to give the appearance of a layer. Since the electrons are constrained to move only along $\underline{B}$ in the E region ($\nu_{en} << \Omega_e$), the neutralization of space charge takes place due to the flow of electrons along the geomagnetic field lines which are inclined in the mid latitudes.

It is this mechanism which is now believed to be responsible for the formation of ionization layers and has been known as the wind shear theory of sporadic E. However, this theory is also not without difficulties. Several objections and advancements have been made in the original wind shear theory of whitehead. Axford (1961, 1963) developed the theory along similar lines considering the effects of diffusion and recombination. He pointed out that the theory should not work at the geomagnetic equator. He also proposed the cork screw mechanism for the downward transport of the plasma. The theory was developed in detail by Chimonas and Axford (1968). Hines (1964) gave the physical picture of the mechanism as discussed above and pointed out that the ionization converges at the point where the wind shear has a maximum negative value. Layzer (1964) objected that the recombination coefficient of the major ions, as demanded by the wind shear theory was an order of magnitude smaller in value than the experimentally verified values. He also pointed out that, in contradiction to the theory, while the peak electron densities were several times the back ground, the minimum densities did not seem to be less than the background. Axford and Cunnold (1966) suggested the meteoric ions of long life times to overcome the objection raised by Layzer. Mac Leod (1966) took into account, both the wind shears and the height variation of the ion neutral collision frequency. Kato et al (1966) considered the effect of a superimposed electric field on a gravity wave motion.

It is now believed that the metallic ions are very important to the formation of ionization layers.

2.3 Equatorial Sporadic E:

Early ionosonde studies of the equatorial E region revealed that the equatorial sporadic E occurs during the daytime almost every day (Matsushita 1951; Rawer 1953; Smith 1957; Ratcliff 1962). Rawer (1960) found that around the dip equator, sporadic E becomes transparent over a wide range of frequencies. A decrease in occurrence of the blanketing E_s from 6° dip down to the equator was reported by Knetch and Schlitt (1961) and Bandyopadhyay and Montes (1963). It is now known that the equatorial sporadic E consists of blanketing type, called E_{sb}, and transparent type, called E_{sq}. Matsushita (1951) showed that the intensity of the E_{sq} is well correlated with the electrojet strength.

VHF forward radar studies (Cohen and Bowles, 1963) over transequatorial path showed their generation in the altitude range of 95 to 100 km, a range agreeing well with the electrojet current system (Singer et al, 1951). With an oblique looking radar at Huancayo, Peru, it was found that the E region irregularities are strongly field aligned (Egan 1960), confirming an earlier prediction. The equatorial electrojet irregularities are associated with the east west electric field which drives the electrojet. The irregularities are present both during the day and night when the electron density are greatly reduced.

Significant contributions to the equatorial electrojet irregularities have been made by the VHF backscatter radar at Jicamarca, Peru. These studies have helped to determine the spatial distribution and drift velocity of the irregularities besides their various features. The Jicamarca backscatter radar operates at 50 MHz which corresponds to 3 m irregularity scale size. On the basis of the spectral characteristics, the irregularities have been classified as Type I and Type II (Bowles, 1967; Balsley 1967; Balsley 1969). Recently, the equatorial electrojet irregularities have been studied using the backscatter radars at Thumba, India (Prakash et al 1973; Muralikrishna 1975) and at central and east Africa also (Crochet et al 1976; Crochet 1977; Hanuise and Crochet 1977, 1978).

The type I spectra are characterised by a narrow returned power band of frequencies, Doppler shifted from the transmitted frequency by about 130 Hz. This Doppler shift corresponds to the drift velocity of the echoing region, close to the ion acoustic velocity in the medium. The Doppler shift was found to be independent of the antenna elevation angle. The type I spectra are observed only when the electrojet currents exceed a critical value.

Power spectrum of the type II irregularities is broader than the type I and these irregularities were found to drift horizontally (Balsley 1967). The type II spectra dominates the type I when the electrojet currents are weak and also when the antenna is pointed in the vertical direction. A detailed study of the region of occurrence of the type II irregularities was carried out by Fejer et al (1975) using the range time intensity diagrams. These studies showed that while during the daytime the echoes came from more or less one continuous region; in the evening and nighttime they came from different altitude regions.

2.3.1 Rocket Results:

With the establishment of the rocket range at Thumba, India, near the dip equator, a new dimension to the study of the equatorial electrojet irregularities has been added. A comprehensive study of the ionization irregularities in the D and E regions has been carried out by Prakash et al (1970, 1971, 1977, 1979). These studies are basic to the understanding of various physical processes responsible for the generation of different ionization irregularities. The groundbased studies, using ionosonde and backscatter radar, are inadequate in this respect as these studies, by themselves, do not give the localised parameters of the medium which have a direct bearing on the generation processes of various types of irregularities. Thus the ground based and insitu studies are complementary to each other.

The rocketborne studies of the irregularities using Langmuir probe, resonance frequency probe and magnetometers (Prakash et al loc.cit) have given the shape, size, spectrum of the irregularities and their relationship with the ambient parameters like the electron density and gradients in it, electric fields and streaming velocity of charged particles. These studies have been very helpful in the development of various theories of the electrojet irregularities. However, there are many rocket observations which are not fully explained theoretically (Prakash et al 1979). A classification of the irregularities, based on their scale size and generation mechanisms, has been made by Prakash et al (1973) in which type M irregularities have a scale size range of 30-300 m and type S have the range 1-15 m. The classification is listed below.

(i) Large scale irregularities type L, (scale size>300 m).
(ii) Due to cross field instability mechanism (type Mc and Sc).
(iii) Due to streaming of electrons (type Ss).
(iv) Due to neutral turbulence (type Mn and Sn).
(v) Rocket induced irregularities.

2.3.2 Theories of the Equatorial Electrojet Irregularities:

To explain the type I radar echoes, a theory of two stream plasma instability was proposed (Farley 1963; Bunneman 1963) which requires that the relative drift between the ions and electrons should exceed the ion acoustic velocity in the medium. However, the rocket observations (Prakash et al 1971) show that the threshold criterion for the excitation of two stream plasma instability was not satisfied, yet the irregularities were observed.

Several theories have been proposed to explain various features of these irregularities (Rogister 1971; Sato 1972; Wein Stock and Sleeper 1972; Kaw 1972; Lee 1972).

11260

The type Mc (Rocket borne) irregularities are believed to be due to the gradient drift instability (or cross field instability). This instability mechanism was first proposed by Simon (1963) and Hoh (1963) in a different context. The gradient drift instability operates in a plasma, if the gradients in the electron density are in the direction of the field. Rocket observations by Prakash et al (1970) confirm this feature of the irregularities. The linear theories of gradient drift instability, in application to the equatorial E region irregularities, have been developed by many authors (Maeda et al 1963; Knox 1964; Tsuda et al 1966; Reid 1968; Rogister and D'Angelo 1970). These theories could explain the type Mc irregularities alone. To explain the type Sc and type II irregularities, Sudan et al (1973) developed a two step theory. But this theory suffers from the use of unrealistic parameters for the calculations as has been pointed out by Sinha (1976). Me Donald (1974, 1979) performed 2-dimensional computer simulation of the type II irregularities. Non linear effects have been considered by Sudan and Keskinen (1977).

2.3.3 Other features of equatorial E region irregularities:

Rocket experiments for the study of nighttime equatorial E region have revealed the existence of layered structures in the electron density profiles (Sinha 1976). The most illustrative example of such layers of ionization (Prakash et al 1970) is shown in figure. 2.1. In some of these layers the electron density varied by over an magnitude. The vertical half width

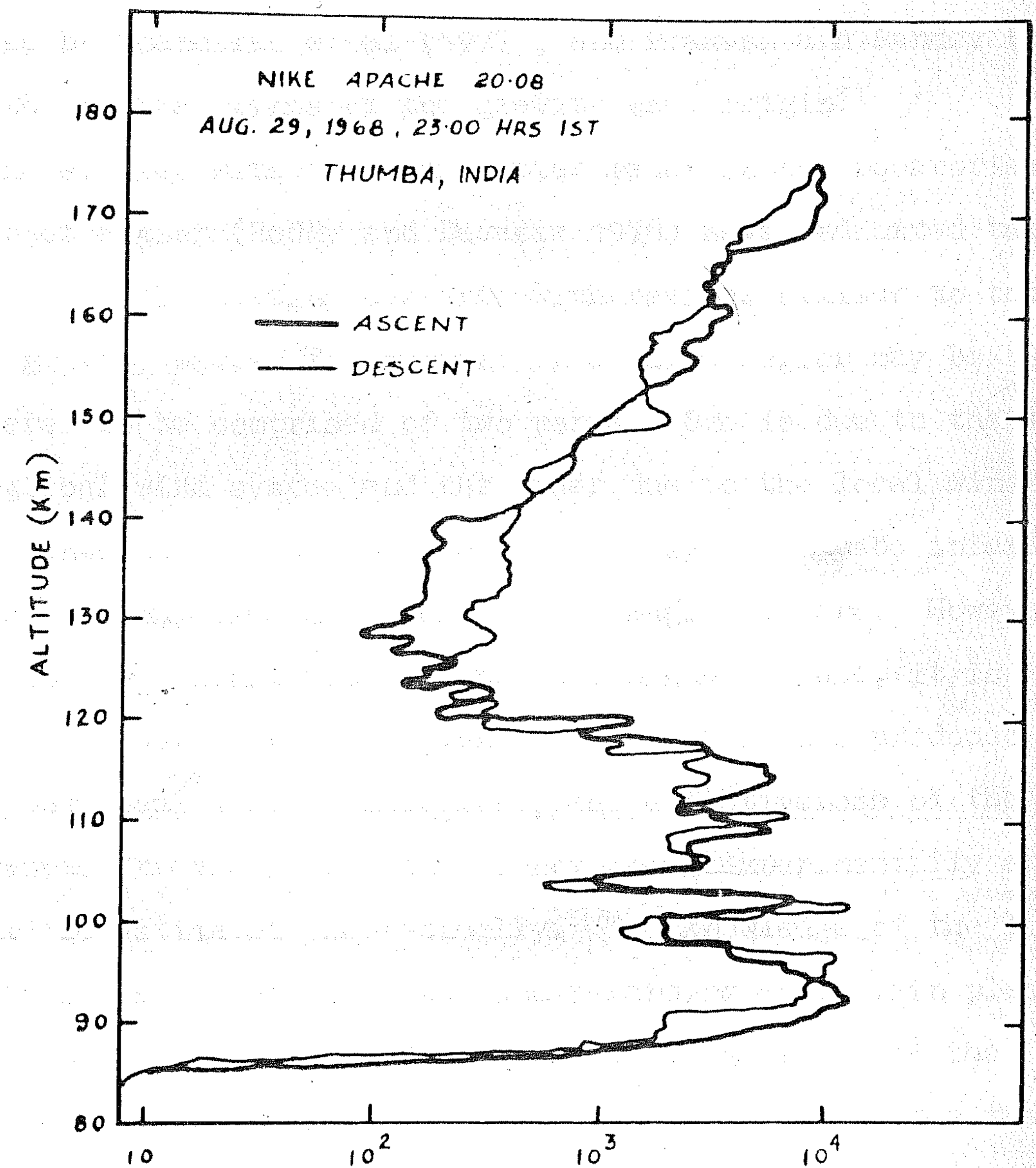
NIKE APACHE 20·08
AUG. 29, 1968, 23·00 HRS IST
THUMBA, INDIA
ASCENT
DESCENT
ALTITUDE (Km)
180
170
160
150
140
130
120
110
100
90
80
10
10^2
10^3
10^4
ELECTRON DENSITY / CC

FIG. 2·1

of these layers was 3-4 km, with a horizontal extent of more than 50 km in the east-west direction. Such layered structures in the electron density profile at the equator were not reported earlier. Attempts to explain the formation of ionization layers in the equatorial E region were initiated by Kato (1973), followed by Anandarao et al (1977), and Prakash and Pandey (1979) using the neutral winds of the gravity wave origin.

The studies with the backscatter radar in the equatorial electrojet region (Reddy and Devasia 1976) have indicated the existence of fluctuating currents with periods similar to those of the gravity waves. The current in a given region may be considered to be comprised of two parts. One is due to the large scale global wind system and the other due to the local winds. The currents due to the large scale wind system may be inferred from the ground based and rocket borne magnetometers. However, due to inherent limitations of the techniques in use, it is difficult to determine experimentally, the currents produced due to the local winds. Therefore, the effectiveness of the local winds in driving current is not known experimentally and can only be estimated theoretically. The knowledge of the local currents is very crucial to the understanding of certain plasma instability processes responsible for the generation of the ionization irregularities. One such mechanism is the the theory of two stream plasma instability (Farley, 1963; Bunemann, 1963) which has been considered to be the likely candidate for explaining type-I radar spectra . For this mechanism to be operative, the relative velocity between ions and electrons should exceed $V_s(1+\Psi)$, where V_s is the ion acoustic velocity in the medium and $\Psi = R_i R_e$ (Rogister and D'Angelo, 1970).

The studies with the rocket borne probes have shown that the average velocity of the electrons relative to the ions was not sufficiently large as to meet the threshold requirement for the generation of two stream instability (Prakash et al, 1971). It is therefore necessary to look for the processes which could give rise to localised streaming of the charges (or currents) in addition to that due to the large scale electrojet currents.

2.4 Gravity Wave-Ionosphere Interaction:

The gravity waves play very important role in the upper atmosphere and these have been used to explain many experimental observations of ionospheric D, E and F regions (Hines, 1960). In recent years, the problem of interaction of neutral winds with the ionospheric plasma has received increased attention and their effects on the equatorial electrojet have been evaluated using various models (Richmond 1973; Forbes & Lindzen 1976; Anandarao 1976; Reddy & Devasia 1977; Prakash & Pandey 1979).

The wind shear~~y~~ theory (Whitehead 1961; Axford 1963) which is usually invoked to explain the formation of ionization layers at the mid-latitudes has previously been considered to be not applicable at the equator because of the special configuration of the magnetic field lines there. It was believed that, at the equator, the shorting of the polarization field $\underline{E}$, does not take place and hence the field gets fully developed. Such a polarization field would cancel out the wind induced field $\underline{W} \times \underline{B}$, (in the frame of reference of the wind) i.e. the total electric field $\underline{E}^W = \underline{E} + \underline{W} \times \underline{B} = 0$ where $\underline{E}^W$ is the electric field in the frame of reference of the wind, $\underline{W}$ is the wind and $\underline{B}$ is the geomagnetic field. From the following equation for the ion velocity (Kato, 1965)

$$\underline{V}_i = \frac{R_i}{B(1+R_i^2)} \left\{ R_i \underline{E}^W + \frac{\underline{E}^W \times \underline{B}}{R_i} + \frac{(\underline{E}^W . \underline{B})\underline{B}}{R_i B^2} \right\} + \underline{W} \qquad (1)$$

where $\underline{V}_i$ is the ion velocity and R_i is the ratio of ion neutral collision frequency and ion gyro-frequency (Equation (1) is valid for electrons also when R_i is replaced by $- R_e$), it can be seen that for a constant plasma density, the ion convergence rate, when $\underline{E}^W = 0$ is given by $\nabla \cdot \underline{V}_i = \nabla \cdot \underline{W}$ (2)

since the winds of gravity wave origin are nearly non divergent (Hines, 1960) hence

$$\nabla . \underline{V}_i = 0 \qquad (3)$$

therefore, when $\underline{E}^W = 0$, the winds will not give rise to the accumulation of ionization. Later on Kato (1973), taking into account the curvature of the geomagnetic field lines, pointed out that the vertical polarization field E_Z would not be fully developed even at the equator due to the partial shorting of the polarization field by the electron currents along the magnetic field lines. The partial shorting of the wind induced polarization fields at the equator would mean that the gravity wave winds would give rise to electric current, the importance of which has been emphasized earlier. Using the winds of gravity wave origin, he calculated an efficiency factor-R, given by

$$R = \left| (\underline{E} + \underline{W} \times \underline{B})_z / (\underline{W} \times \underline{B})_z \right| \qquad (4)$$

for the production of the net vertical field in the frame of reference of the wind. He found that R has a non zero value even at the equator. Its value is zero when $\lambda_z = 0$ and reaches an asymptotatic value for $\lambda_z \geqslant 20$ kms. He, therefore suggested that the wind shear theory, in forming the ionization layers, is applicable even at the equator, though with much lesser efficiency as compared to that in the mid-latitudes.

Anandarao et al (1977) developed a two dimensional model of the interaction and calculated the parameter R(as defined above) and the ion convergence rates at 100 km. They concluded that the results of Kato (1973) were an over estimate. Kato (1973) has neglected the horizontal wavelengths, both north-south and east-west, while Anandarao et al (1977) have not considered the north-south wavelenth, Kato (1973) also neglected the north-south and vertical velocities. Inclusion of the wavelength along the geomagnetic field line is very important, as was demonstrated by Prakash and Pandey (1979) and is discussed in detail in the following sections.

The gravity wave induced electric fields, at a given place, can have their origin

(a) due to the local gravity wave winds

(b) due to the gravity wave winds present in some other region of the ionosphere

(c) due to a combination of situations (a) and (b).

We treat the situation (a) and (b) separately. In this chapter, effects of the local gravity wave winds, situation (a), alone are discussed. The problem of generation and transmission of electric fields, the situation (b), is discussed in chapter III, separately.

In what follows, the interaction of local winds (gravity wave winds) with the ionospheric plasma is studied using a three dimensional model. The electric field, current, streaming velocity of electrons relative to ions and the plasma convergence rates resulting from this interaction have been calculated using the winds of gravity wave origin. The results of these calculations which are applicable to the gravity waves of medium scale sizes are different, both qualitatively and quantitatively, from those obtained earlier(Kato 1973; Anandarao et al 1977) .

2.5 The Three Dimensional Model:

2.5.1 The field line geometry

The present model has been developed assuming the magnetic field to be homogeneous i.e. the magnetic field lines are straight everywhere. Although the geomagnetic field lines are curved, these can be assumed to be straight if the bending of the field lines (h) over half the wavelength ($\lambda_x/2$) along the magnetic field is much less, say an order of magnitude, than half the vertical wavelength $\lambda_z/2$.

TABLE - 2.1

Bending of field lines (h) over half the wavelength ($\lambda_x/2$) along the magnetic field. Vertical wavelengths for which the bending of the field lines can be ignored is also listed.

Sr.No.	$\lambda_x/2$ (km)	h (km)	$\lambda_z/2$ (km)
1	50	0.1	>1.0
2	100	0.4	>4.0
3	200	1.6	>16.0

The bending of the geomagnetic field lines was calculated using the formula given by Alfven and Falthammer (1963) and its value is listed in Table-I for various values of $\lambda x/2$. Correspondingly, the lower limit of $\lambda z/2$ for which the bending of the field lines can be ignored is also listed. Noting the wavelength ranges which can exist in the ionosphere (e.g.Beer, 1974), the restrictions put on the values of $\lambda z/2$ for various values of horizontal wavelengths are not at all serious. According to the earlier theories, the homogeneous magnetic field will be most favourable for the full development of the polarization field, thereby making R = 0 at the equator. However, the following discussion shows that in the case of a 3-dimensional model, this is not true.

We choose a cartesian system of coordinates in which x-axis is along the magnetic field, y-axis is horizontal and is toward magnetic west and z-axis is perpendicular to both x and y axes. It may be pointed out that the x-axis will not be horizontal except at the equator. The gravity wave winds are generally defined in the cartesian coordinate system where two axes are horizontal and the third one is vertical. Let such a reference system be denoted by x', y' and z'. Let y'-axis be same as the y-axis, z'-axis is in the vertical direction and x' towards magnetic north. The gravity wave wind, in this coordinate system can be written as

$$\underline{W} = \underline{W}_0' \exp\{i(\Omega t - k_x' x' - k_y' y' - k_z' z')\} \qquad (5)$$

where $\underline{W}_0'$ is the wind vector having components $W_{0x}', W_{0y}', W_{0z}'$ and k_x', k_y' and k_z' are the components of the wave vector in the respective directions.

2.5.2. Transformation of the gravity wave winds:

The wind given by eqn.(5) can be easily transformed into the x, y, z coordinate system by rotating the x', z' axes in the plane perpendicular to y-axis and is given by

$$\underline{W} = \underline{W}_0 \exp\{i(\Omega t - k_x x - k_y y - k_z z)\} \qquad (6)$$

where

$$W_{0x} = W_{0x}' C - W_{0z}' S$$
$$W_{0z} = W_{0z}' C + W_{0x}' S$$
$$k_x = k_x' C - k_z' S$$
$$k_z = k_z' C + k_x' S$$
$$C = \cos I, \quad S = \sin I$$

I is the dip angle, positive in the northern hemisphere. In the ionosphere, the ratio of the collision frequency to the gyrofrequency for electrons is much smaller than that for the ions. Therefore, the neutral wind in the ionosphere gives rise to charge separation and the re-distribution of the charges. If the polarization fields thus produced are assumed to be electrostatic then

$$\underline{E} = -\nabla\phi \qquad (7)$$

As the plasma parameters and the magnetic field have been assumed to be uniform, the potential ϕ can be assumed to be of the same form as the wind and can be written as

$$\phi = (\phi_{01} + i\phi_{02}) \exp\{i(\Omega t - k_x x - k_y y - k_z z)\} \quad (8)$$

where ϕ_{01} and ϕ_{02} are real constants. From the equns.(7) and (8) it can be seen that electric field will be present in all the three directions. The presence of an electric field along the magnetic field may look surprising. However, its presence can be visualised from the following discussion.

The gravity wave winds given by eqn (6) can be resolved in two directions, one parallel to B, and the other perpendicular to it. This can be achieved by rotating the y and z axes in the plane perpendicular to x by an angle α such that $\alpha = \tan^{-1}\left(\frac{W_{0z}}{W_{0y}}\right)$. If x, ξ, η is the new set of axes, then the transformed components of the wind will be given by

$$W_x = W_{0x} \exp\{i(\Omega t - k_x x - k_\xi \xi - k_\eta \eta)\}$$
$$W_\xi = (W_{0y} \cos\alpha + W_{0z} \sin\alpha) \exp\{i(\Omega t - k_x x - k_\xi \xi - k_\eta \eta)\}$$
$$W_\eta = 0 \quad (9)$$

Thus the wind velocity in the plane perpendicular to B is only along ξ axis, however its amplitude changes sinusoidally as one moves along any of the three axes.

2.5.3 The ion motion:

Let us consider the effect of a neutral wind on the motion of ions and electrons when the polarization fields are small. It can be seen from eqn.(1) that the wind along B does not result in any charge separation because both ions and electrons

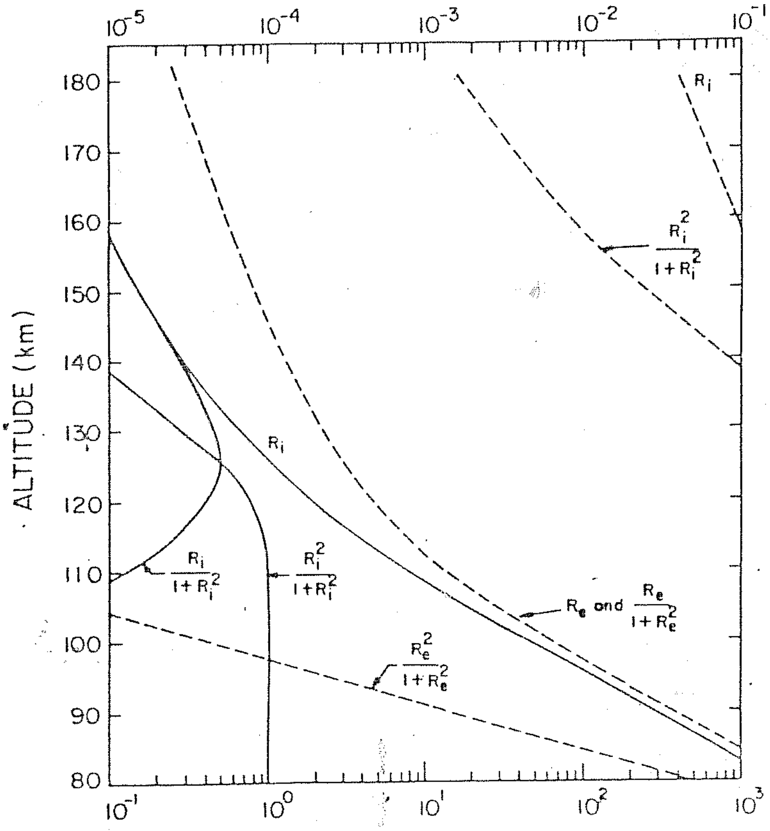

Fig. 2.2: Variation of $(R_{i,e})$, $[R_{i,e}/(1+R^2_{i,e})]$, $[R^2_{i,e}/(1+R^2_{i,e})]$ with altitude. Values of R_i and R_e have been taken from Richmond (1972). The scale on top of the figure is for curves drawn with dashed lines. The lower scale is for the curves drawn with solid lines.

move with the same velocity in that direction.

As can be seen from fig.2.2 that Re$\ll$ Ri. Hence from eqn.(1), the motion of electrons in the plane perpendicular to B, is negligible compared to that of the ions. Also, due to the wind W_ξ the ions move with velocity $W_\xi R_i^2/(1+R_i^2)$ and $-W_\xi R_i/(1+R_i^2)$ along ξ and η directions, respectively. The resultant direction of the ions will therefore make an angle θ with the ξ axis where $\theta = \tan^{-1}(-1/R_i)$. Therefore, if the axes ξ and η are further rotated by an angle θ around the x-axis, then the ion velocity components in the new set of axes x, ξ', η' can be written as

$$V_x = V_{0x} \exp\{i(\Omega t - k_x x - k_\xi' \xi' - k_\eta' \eta')\}$$
$$V_\xi' = (V_{0\xi} \cos\theta + V_{0\eta} \sin\theta) \exp\{i(\Omega t - k_x x - k_\xi' \xi' - k_\eta' \eta')\}$$
$$V_\eta' = 0 \qquad (10)$$

Therefore, in a plane perpendicular to <u>B</u>, the ions move only in the ξ' direction. It can be seen that although the motion of ions is only along ξ', its amplitude varies sinusoidally as one moves along any of the three axes x, ξ' and η'. As is evident the ion convergence takes place at the nodal points of these sinusoidal variations. In fig.2.3(a) the horizontal and vertical lines are drawn every $\lambda\xi'/2$ and $\lambda x/2$ distance and the direction of motion of the ions is shown by arrows in the $x\xi'$ plane. A similar picture is valid for the $\xi'\eta'$ plane, though not shown in the diagram. It can be clearly seen that the regions with excess and deficiency of positive charges

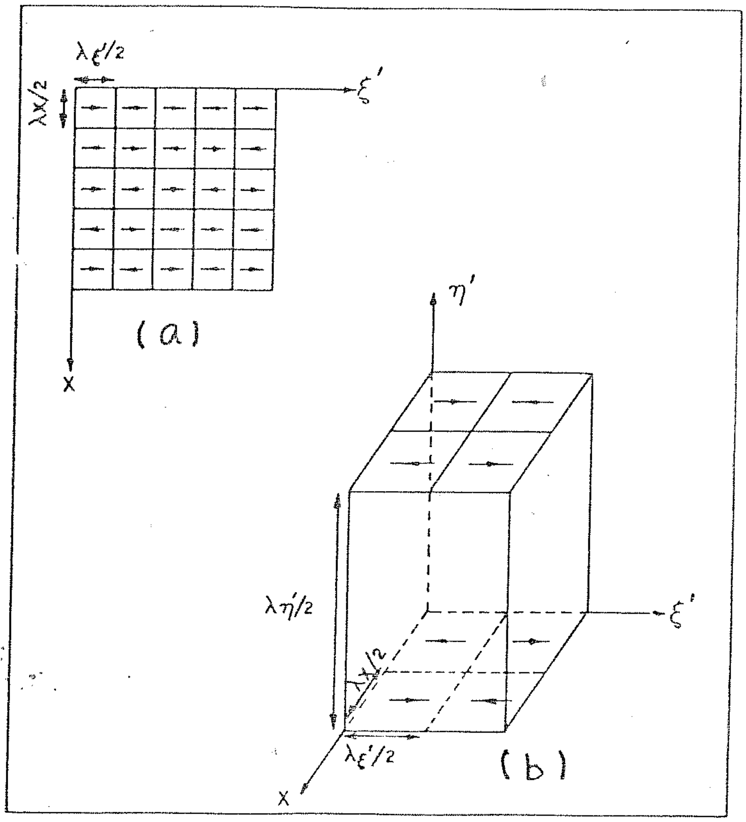

Fig. 2.3: Schematic of ion motion in the $x\xi'$ plane is shown in Fig. 2.3 a. The dividing lines are at half the wavelength in the respective directions. The ion motion in two $x\xi'$ planes separated by $\lambda\eta'/2$ is shown in Fig. 2.3 b. The arrows show the direction of motion of ions.

occur every half wavelength as one moves along the magnetic field axis x and the axis ξ'. The ion motion in two x-ξ' planes separated by $\lambda\eta'/2$ is also shown in fig.2.3 b. Here also, the excess and deficiency of charges occurs every half the wavelength along the respective directions. This excess and deficiency of charges gives rise to an electric field not only along ξ' and η' but also along x which is the magnetic field direction. The electric field along **B** will result in an electron current along the magnetic field lines due to very large parallel conductivity for electrons. This current will thereby reduce the polarization fields. The electric fields in the perpendicular plane will give rise to a small electron and ion current in that plane. These currents will modify the direction of the conventional current in the plane perpendicular to B from direction ξ' to some other direction, say ξ_1. The argument as given above still remains valid if a proper set of orthogonal axes is chosen.

The current density $\underline{J}$, in terms of the total electric field $\underline{E}$ is given by

$$\underline{J} = \sigma_0 \underline{E}_{\parallel} + \sigma_P \underline{E}_{\perp}^{W} + \frac{\sigma_H}{B}\left(\underline{B} \times \underline{E}^{W}\right) \qquad (11)$$

where σ_0, σ_P and σ_H are the parallel, Pederson and Hall conductivities respectively. $\parallel$ and $\perp$ denote the components parallel and perpendicular to the magnetic field. Also

$$\nabla \cdot \underline{J} = 0 \qquad (12)$$

using equations (6, 7, 8, 11 and 12) we get

$$\phi_{01} = 0 \tag{13}$$

$$\phi_{02} = B\left\{\frac{\sigma_P(k_y W_{0z} - k_z W_{0y}) + \sigma_H(k_y W_{0y} + k_z W_{0z})}{\sigma_0 k_x^2 + \sigma_P(k_y^2 + k_z^2)}\right\} \tag{14}$$

using the condition $\nabla \cdot \underline{W} = 0$ (Hines, 1960), ϕ_{02} can be rewritten as

$$\phi_{02} = -\frac{BW_{0y}}{k_z}\left\{\frac{\sigma_P(k_y^2 + k_z^2 + k_x k_z \gamma) + \sigma_H k_x k_z \gamma}{\sigma_0 k_x^2 + \sigma_P(k_y^2 + k_z^2)}\right\} \tag{15}$$

where $\gamma = W_{0x}/W_{0y}$

In deriving the above expressions we have ignored the gradients in the electrical conductivities.

The electric field components can then be obtained using equation (7) which reduces to

$$\left.\begin{aligned} E_x &= -k_x \phi_{02} \exp\{i(\Omega t - k_x x - k_y y - k_z z)\} \\ E_y &= -k_y \phi_{02} \exp\{i(\Omega t - k_x x - k_y y - k_z z)\} \\ E_z &= -k_z \phi_{02} \exp\{i(\Omega t - k_x x - k_y y - k_z z)\} \end{aligned}\right\} \tag{16}$$

From eqn.(15) and (16) we get

$$E_{0z} = BW_{0y}\left\{\frac{\sigma_P(k_y^2 + k_z^2 + k_x k_y \gamma) + \sigma_H k_x k_z \gamma}{\sigma_0 k_x^2 + \sigma_P(k_y^2 + k_z^2)}\right\} \tag{17}$$

As Kato (1973) has retained vertical field E_z only, the factor R in his case can be used to determine extent of shorting. In our model calculations, the factor R does not have a unique value as the field is present in all the three directions and the factor R does not convey the same meaning as is conveyed in his case. Nevertheless, for comparison we have calculated the ratio of the Z – component of the field and it is given by

$$R_z = \frac{E_z^W}{(\underline{W} \times B)_z} = \frac{k_x(\sigma_0 k_x - \sigma_P k_y \gamma - \sigma_H k_z \gamma)}{\sigma_0 k_x^2 + \sigma_P(k_y^2 + k_z^2)} \qquad (18)$$

Similarly,

$$R_y = \frac{E_y^W}{(\underline{W} \times \underline{B})_y} = -\frac{k_x}{k_z W_{oz}} \left\{ \frac{k_y W_{oy}(\sigma_0 k_x - \sigma_P k_y \gamma - \sigma_H k_z \gamma)}{\sigma_0 k_x^2 + \sigma_P(k_y^2 + k_z^2)} + W_{ox} \right\} \qquad (19)$$

It can be seen from eqn.(18) and (19), the factors $R_y \neq R_z$. When $k_x = 0$, $R_z = 0$ and $R_y = 0$. Thus when $k_x = 0$, the polarization fields, E_y and E_z, are fully developed. The electric currents due to the gravity wave winds can be obtained using eqn.(11) and are given by

$$\begin{aligned} J_x &= \sigma_0 E_x \\ J_y &= \sigma_P(E_y + BW_z) - \sigma_H(E_z - BW_y) \\ J_z &= \sigma_P(E_z - BW_y) + \sigma_H(E_y + BW_z) \end{aligned} \qquad (20)$$

2.6 Results and Discussion

The electric fields, currents and the drift velocity of electrons relative to ions were calculated at the equator, at each altitude separately, by assuming gravity waves with the given parameters. The envelopes of these parameters are shown in fig. 2.4 through 2.6 . In these figures, the solid and dotted portions of the curves have been used to represent the phase relationship of various parameters with the wind. These parameters are drawn with solid curves when they are in phase with the wind and with the dotted curves when they are 180° out of phase with the wind. 'r' denotes the region where a reversal of phase has taken place.

In figs. 2.7 and 2.8 , the results of the present studies are compared with those of Kato (1973) and Anandarao et al (1977). The variation of ion convergence rates per ion with altitude at varies latitudes is given in fig. 2.9 .

2.6.1 The electric fields.

The electric fields can be calculated using eqns. (15) and (16). Fig. 2.4 gives the envelope of the electric field components. For these calculations, we have assumed $\lambda_x = \lambda_y$ = 100 kms, λ_z = 5 kms and W_{oy} = 100 m/sec. Using $\nabla \cdot \underline{W} = 0$ one can calculate W_{ox} and W_{oz} which in this case would be 100 m/sec and 10 m/sec respectively. Since we have chosen $k_x = k_y$, the corresponding fields E_{ox} and E_{oy} are also equal. The field E_{oz} is greater than the field E_{ox} or E_{oy} by a constant factor k_z/k_y.

It can be seen from fig. 2.4 that the electric field components do not maintain a constant phase relationship with the wind. Above 90 km the polarization fields E_{oy} and E_{oz} are seen to be very poorly developed in comparison to the wind

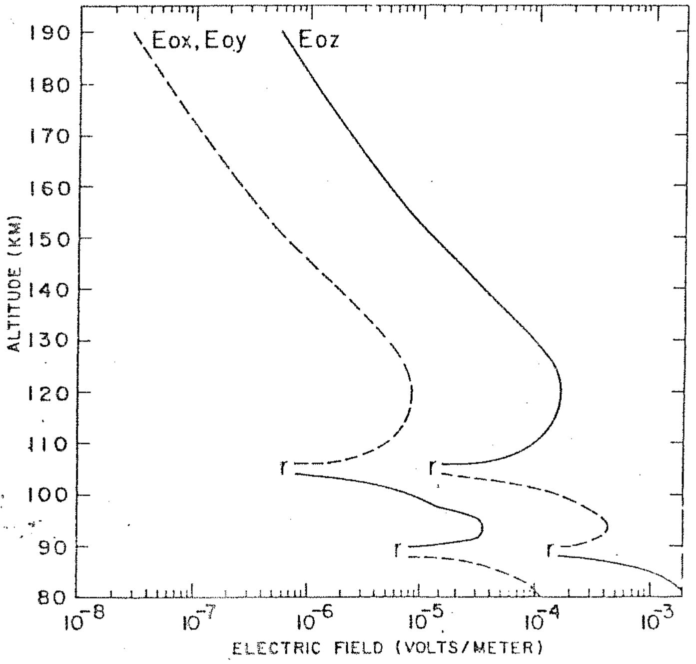

Fig. 2.4: Envelopes of electric field components with the altitude at the equator. The solid and dotted portions of the curves have been used to represent whether the field is in phase or 180° out of phase with the wind. r denotes the region where such a reversal of phase occurs. The wave parameters are $\lambda x = \lambda y = 100$ km, $\lambda z = 5$ km and $W_{oy} = 100$ m/sec.

induced fields $(\underline{W} \times \underline{B})_y$ and $(\underline{W} \times \underline{B})_z$ respectively, which are approximately 3×10^{-4} v/m and 3×10^{-3} v/m in the y and z directions respectively.

2.6.2 The electric currents:

The electric fields obtained above were used to calculate the currents due to the gravity wave winds. Fig. 2.5 gives the envelope of the amplitudes of the currents with altitude. Corresponding to these currents, the streaming velocities of electrons relative to ions are shown in fig. 2.6 .

Since the electric fields and winds have an exponential term, it can be seen that the gravity wave driven currents reverse their direction of flow at every half the wavelength as one moves in any of the three directions. From fig. 2.5 it can be seen that J_{oy} remains in phase with the wind and has a broad maximum centred around 106 km with a peak value of approximately 3 Amp/km^2.

The vertical profile of the electrojet current (J_E) obtained in American zone (Mayanard, 1967; Devis et al 1967) and in Indian zone (Maynard et al 1965; Sastry 1970) peaks around this altitude only. The peak value, was found to be 10-12 Amp/km^2 (Sampath, 1976). Therefore, the contribution of gravity wave driven current (for W_{oy} = 100 m/sec) is substantial even near the peak of electrojet current. As J_E decreases more rapidly with altitude than J_{OY}, the ratio J_{OY}/J_E will increase with the altitude. The current J_{OY} when superimposed upon the current J_E, would give rise to regions of enhanced and reduced

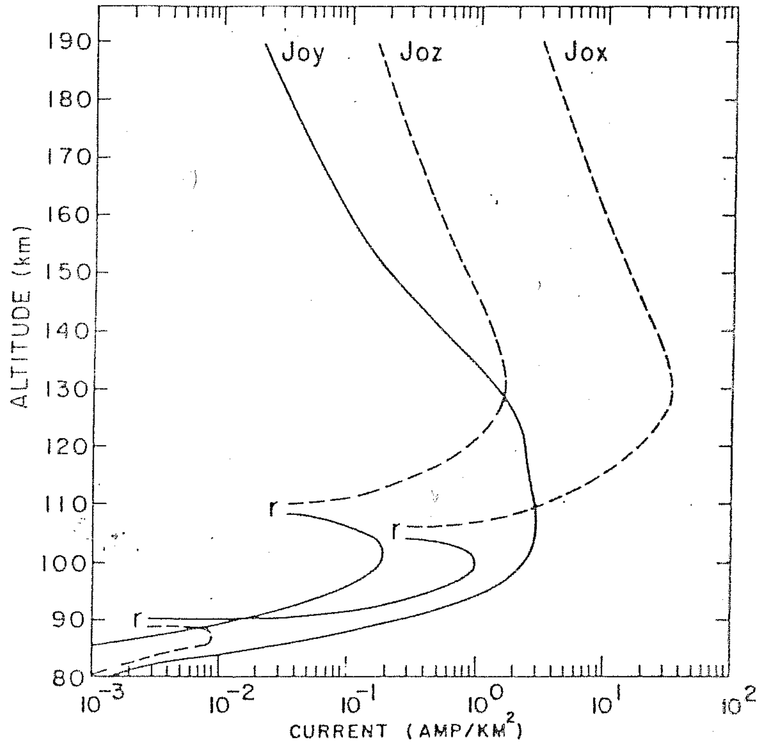

Fig.2.5: Envelopes of current components with altitude corresponding to the fields of Fig.2.4. Solid and dotted portions of the curves have the same significance as in Fig.2.4.

currents. In the regions where the current is enhanced, the streaming velocity of electrons relative to ions would be larger than what is calculated using average electrojet currents.

The variation of the current components as given in fig.2.5 can be qualitatively explained when the polarization fields E_y and E_z are negligible in comparison to the wind induced fields $(\underline{W} \times \underline{B})_y$ and $(\underline{W} \times \underline{B})_z$, respectively. From fig.2.4 it can be seen that above 96 km, the polarization fields are smaller by over an order of magnitude than the wind induced fields. Therefore, above 96 kms the equation (20), can be approximated to

$$J_x = \sigma_H B W_x + \sigma_P B W_y k_z / k_x$$
$$J_y = \sigma_H B W_y \left(1 + \frac{\sigma_P}{\sigma_H} \frac{W_z}{W_y} \right) \qquad (21)$$
$$J_z = \sigma_H B W_y \left(W_z / W_y - \sigma_P / \sigma_H \right)$$

In the present case, both W_{oy} and W_{oz} are positive and $W_{oz} = 0.1\, W_{oy}$; hence the current J_{oy} will remain positive in the region of interest. Since σ_H is fairly constant and $\sigma_P < \sigma_H$ between 105-125 kms, J_{oy} has a broad maximum centred around 106 km.

The current J_{oz} will change its direction when $W_{oz}/W_{oy} < \frac{\sigma_P}{\sigma_H}$ This condition is satisfied above 110 kms. Above 126 kms the ratio $\sigma_P/\sigma_H > 1$. Therefore, the current $|J_{oz}|$ exceeds $|J_{oy}|$. The ratio of the two current components is given by

$$|J_{oz}/J_{oy}| = \left(W_{oz}/W_{oy} - \sigma_P/\sigma_H \right) / \left(1 + \sigma_P W_{oz} / \sigma_H W_{oy} \right) \qquad (22)$$

As σ_P/σ_H increases with altitude, the limiting value will be W_{oy}/W_{oz} (10, in our case) which is achieved much above 190 kms. At an altitude of 190 kms $|J_{oz}/J_{oy}| = 7.5$.

The most striking feature of fig. 2.5 is that above 110 kms the current $|J_{ox}|$ becomes large compared to J_{oy} and J_{oz}. This can be explained from eqn.(12) which can be written as

$$J_{ox} = -k_y\left(J_{oy} + k_z J_{oz}/k_y\right)/k_x \qquad (23)$$

In our case $k_z/k_y = -20$ and $k_x = k_y$. The contribution of J_{oz} to J_{ox} becomes larger than that of J_{oy} above 115 km where $|J_{oz}| > |J_{oy}/20|$. Above this altitude the contribution of J_{oy} is negligible and hence $|J_{ox}| \simeq 20|J_{oz}|$

2.6.3 The streaming velocities:

Fig. 2.6 gives the streaming velocity of electrons relative to ions calculated using currents given in fig. 2.5 . It can be seen that the maximum parallel streaming velocity of 900 m/sec occurs around 130 km. This velocity is sufficiently large to excite the ion cyclotron instability. This instability mechanism has been invoked (D'Angelo, 1973) to explain the type III radar echoes as observed at the Auroral latitudes (Balsley and Ecklund, 1972). It was, however, pointed out (D'Angelo, 1973) that these echoes will not be observed at the equator because such large relative velocity between electrons and ions are not available. The present calculations show that this need not always be true.

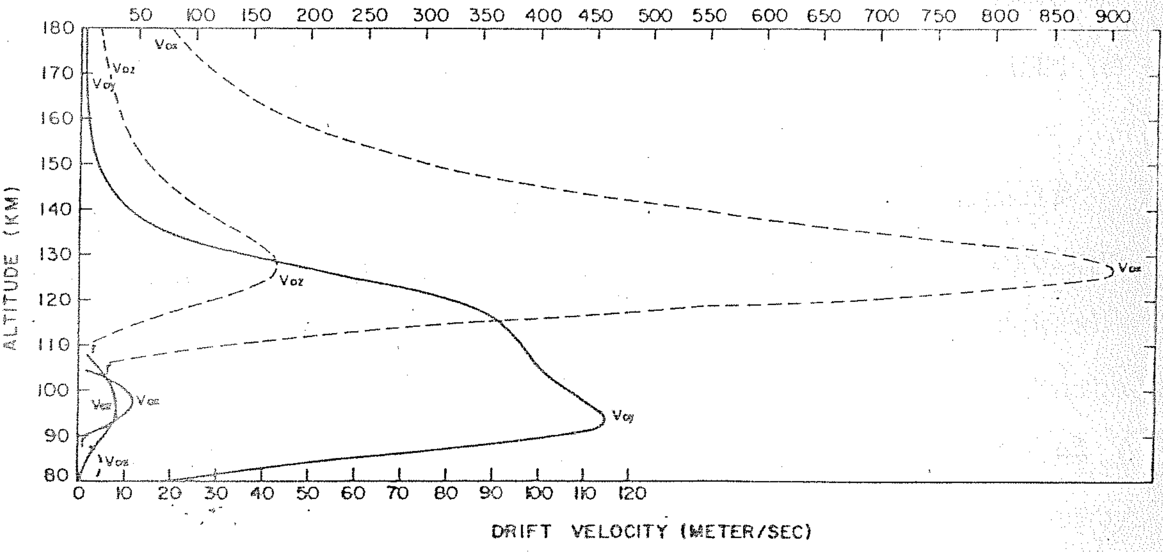

Fig. 2.6: Envelopes of streaming velocities of electrons relative to ions with altitude. The scale on the top of the figure is for V_{ox} only. The lower scale is for V_{oy} and V_{oz}. Solid and dotted portions of the curves have the same significance as in Fig. 2.5.

As has been pointed out earlier, the threshold requirement for the excitation of the two stream plasma instability is that $V_d/(1+\psi) > V_s$ where V_d is the drift velocity of electrons relative to ions. In the electrojet region $V_d/(1+\psi)$ is maximum at an altitude where $\psi = 1/3$, while at the peak of the electrojet $\psi = 1$ (Fejer et al 1975). In the E-region $V_s \sim 360$ m/sec and hence, to satisfy the threshold criterion, V_d should be greater than 480 m/sec at an altitude few km above the peak of the electrojet. At the peak of the electrojet V_d should be even larger than 480 m/sec.

Rocket borne proton procession magnetometers, Langmuir probes and resonance probes were used to determine the average streaming velocity of electrons relative to the ions (Prakash et al, 1971 and Nike-Apache flight 10.44 and 10.45 from Thumba). A maximum velooity of 340 m/sec was obtained on flight 10.44 and 380 m/sec on flight 10.45, showing that the drift velocity of electrons relative to ions never exceeded the threshold value for the excitation of the two stream instability.

It can be seen from fig.2.6 that, for the gravity waves with the assumed parameters, the additional streaming velocity of electrons relative to ions in the E-W direction is quite large, its maximum value being around 100 m/sec at 106 km. If these velocities are added to those corresponding to the electrojet currents, it is quite possible that the threshold criterion may be satisfied, at least, in some of the regions.

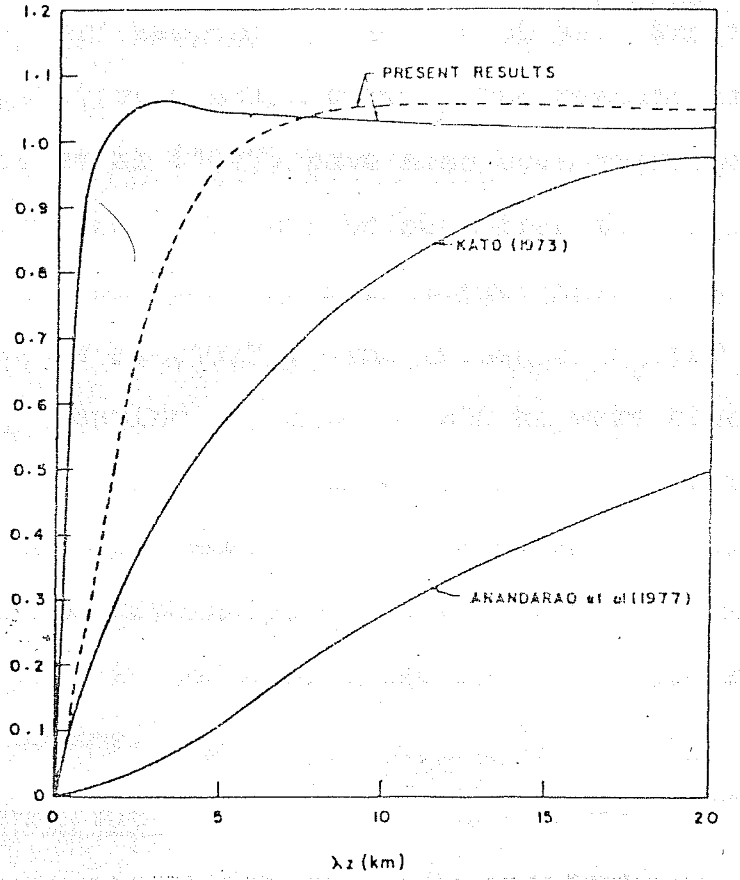

Fig 2.7 Variation of R(Or Rz) with The "Present Results" are for the cases when $\lambda_x = \lambda_y = 50$ km and 200 km respectively.

In such regions the plasma would become unstable and the ionization irregularities would be generated.

2.6.4 The parameter R

The values of R_z were calculated at the equator for parameters corresponding to 100 km altitude using various values of λ_z and keeping $\lambda_x = \lambda_y$ = 50 km. The results are given in fig.2.7 by a solid curve. The results of Kato (1973) and Anandarao et al (1977) have also been reproduced for comparison purposes. It can be seen from the fig.2.7 that the value of R_z, in our case is much larger than those of Kato (1972) and Anandarao et al (1977). The values of R_z for various values of λ_z keeping $\lambda_x = \lambda_y$ = 200 km were also calculated for 100 km altitude and are shown in fig.2.7 with dotted curve. For the case when $\lambda_x = \lambda_y$ = 50 km the value of R_z in our case remains within 1.0 ± 0.1 for $\lambda_z \geqslant 0.75$ km. The value of R_z lies in the same range for $\lambda_z \geqslant 3.0$ kms when $\lambda_x = \lambda_y$ = 200 kms.

2.6.5 Ion convergence rate:

Assuming electron density to be constant with altitude the ion convergence rate per ion can be obtained using eqns.(1) and (7). Ignoring the variation in the ion gyro-frequency and ion neutral collision frequency with altitude, the convergence rate is given by ($k_z \gg k_y, k_x$; $W_x > W_z$)

$$|\nabla \cdot \underline{V}_i| = \left| \frac{\phi_z}{B(1+R_i^2)} \left(R_i k_z^2 + \frac{k_x^2}{R_i} \right) + \frac{(R_i k_z W_y - k_x W_x)}{(1+R_i^2)} \right| \quad (24)$$

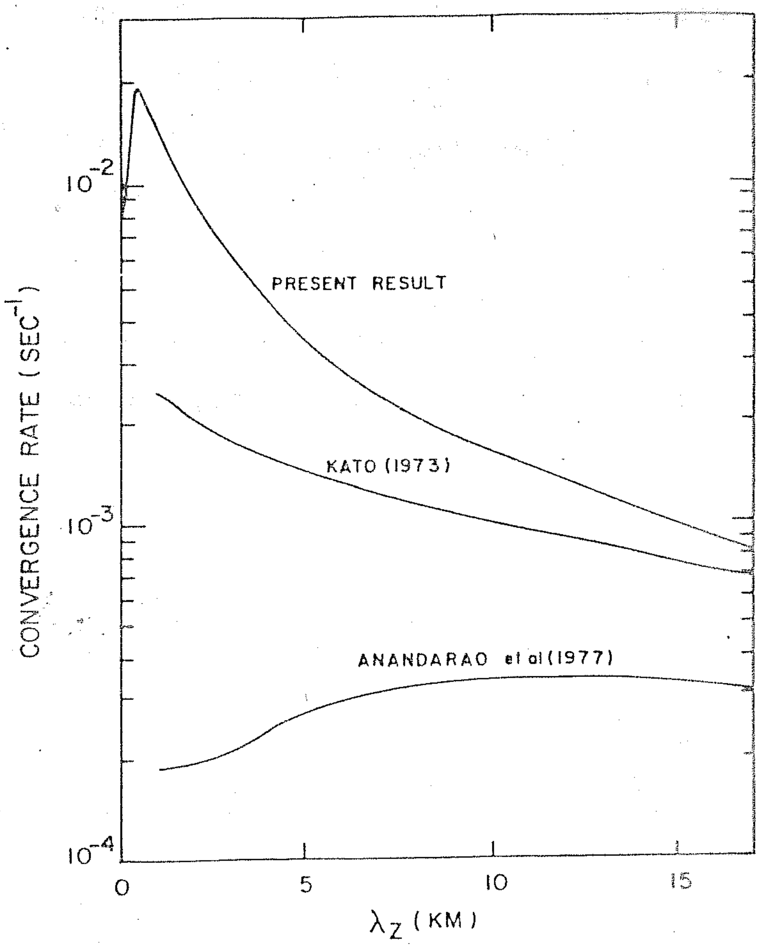

Fig.2.8. Variation of ion convergence rate with λ_Z at 100 km altitude at the equator. The value of R_i has been taken from Fig.2.2 and is approximately equal to 50.

For the sake of comparing our results with those of Kato (1973) and Anandarao et al (1977), we have calculated the convergence rates at 100 km at the equator, for various values of λ_z keeping $\lambda_x = \lambda_y = 50$ kms. The results of these calculations are given in fig.2.8 . While Kato (1973) has neglected the horizontal wavenumber in comparison to the vertical, Anandarao et al (1977) have assumed the horizontal wavelength to be wholly in the E-W direction. It should be noted here that Kato (1973) and Anandarao et al (1977) have used Ri $\backsim$ 10 for their calculations. We have taken Ri $\backsim$50 (following Richmond, 1972) and have re-calculated the convergence rates using appropriate equations for their cases also. It can be seen from fig.2.8 that the convergence rates obtained with our model are much larger compared to those of Kato (1973) and Anandarao et al (1977). For $\lambda_z = 1$ km, the convergence rate in our case is approximately 5 times larger than that of Kato (1973) and 60 times than that of Anandarao et al (1977). With increasing λ_z this ratio decreases. The present calculations show that even the gravity waves with small vertical wavelengths can give rise to appreciable convergence rates.

Fig.2.9 shows the altitude variation of the ion convergence rates at various dip angles, calculated using eqn.(24). The gravity wave parameters used for this purpose were $\lambda_x = \lambda_y = 100$ km, $\lambda_z = 5$ kms and $W_{oy} = 100$ m/sec. It can be seen from these curves that the ion convergence rate below 120 km is maximum at the equator and minimum at the poles.

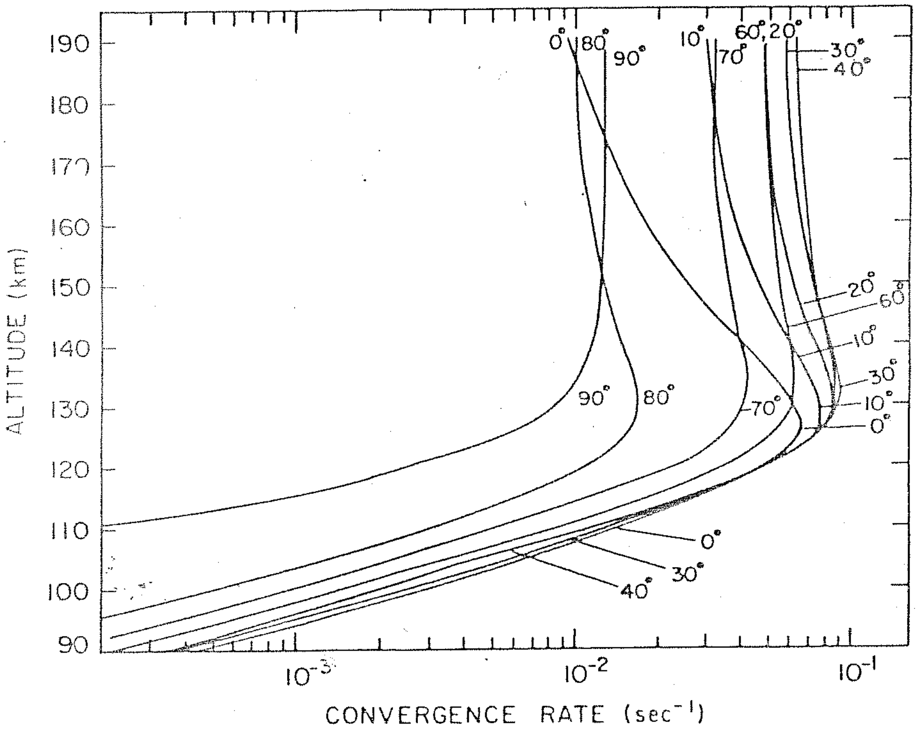

Fig. 2.9: Variation of ion convergence rate with altitude at various latitudes. The gravity wave parameters used for these calculations are $\lambda x' = \lambda y' = 100$ km, $\lambda z' = 5$ km and $W_{oy} = 100$ m/sec.

This is contrary to the results of the earlier workers (i.e.Axford 1963) which predicted zero or smaller convergence rates at the equator compared to that in the mid-latitudes. Above 130 km however, there is a marked difference in the convergence rates. The convergence rates increases from the equator to 40° dip latitude and thereafter it decreases and becomes minimum at 80° dip latitude.

Hence when a three dimensional model of gravity wave winds is used, the ion convergence rates below 130 kms at the equator are quite large even when the geomagnetic field lines are assumed not to be curved as is essential for the models of Kato (1973) and Anandarao et al (1977).

The formation of the ionization layers in the E-region would be possible if and only if the ion convergence rate is much larger than the rate of recombination. While the ion convergence depends upon the gravity wave parameters, the geometry of the geomagnetic field lines and Ri, the recombination rate depends on the recombination constant α_R and the electron density, n_e.

The normally assumed value of α_R in the E region is 3×10^{-7} cm^{-3} sec^{-1}. In the 100 km region, $n_e \sim 10^5$ cm^{-3} during day time and 5×10^3 cm^{-3} during nighttime. It can therefore be seen that during the nighttime the recombination rate $\sim 1.5 \times 10^{-3}$ sec^{-1}. This is less than the calculated value of the convergence rate which is 6×10^{-3} sec^{-1}. (It should be again pointed out here that Kato (1973) and

Anandarao et al (1977) have used $R_i \sim 10$ at 100 km whereas we have used $R_i \sim 50$; hence their values of the convergence rates should be divided by a factor of 5 for comparison with our results). Hence during nighttime the formation of the ionization layers through gravity wave winds is feasible. During daytime, the recombination rate is $\simeq 3 \times 10^{-2}$ sec^{-1} which is larger than the calculated convergence rate and hence, during the day time, the formation of the ionization layer is not feasible with the normally assumed value of α_R. It should be noted here that, to explain the formation of the ionization layers during daytime in the midlatitudes, the presence of metallic ions having a much smaller recombination constant than what is assumed here has been resorted to.

We will now discuss the convergence rates in the following two limiting eases:

1. When $k_x = 0$ i.e. the wavelength along $\underline{B}$ is infinitely large. As $\nabla \cdot \underline{W} = 0$ we get from eqn.(15)

$$\phi_{0z} = -BW_{0y}/k_z = BW_{0z}/k_y \qquad (25)$$

Substituting these values in eqn.(24) we get $\nabla \cdot V_i = 0$. Therefore when wavelength along $\underline{B}$ is very large the convergence rate is very small or zero.

2. In the lower E region $R_i \gg 1$. As $k_z \gg k_x, k_y$ and $W_{0z} < W_{0x}, W_{0y}$; eqn.(24) can be greatly simplified and we get

$$\nabla \cdot \underline{V}_i = |k_z(BW_{0y} - E_{0z})/BR_i| \qquad (26)$$

The field E_{0z} when calculated for various combinations of wave parameters was found to be much smaller than the wind induced field $(\underline{W} \times \underline{B})_z$. Above 87 kms for the wave parameters assumed here it was found to be smaller than the wind induced field, at least by a factor of eight. Therefore, in such cases the polarization field can be neglected in comparison to the wind induced field and we get

$$\nabla \cdot \underline{V}_i = \left| k_z W_{oy} / R_i \right| \qquad (27)$$

Using the transformations given by eqn.(16) required to go from the coordinate system x', y', z' to x, y, z ; the eqn.(27) becomes

$$\nabla \cdot \underline{V}_i = \left| (k_z' C + k_x' S) W_{oy} / R_i \right| \qquad (28)$$

At equator this expression is similar to the one obtained in the wind shear theory and we recover the result that in the lower E region, the ion convergence is due to the vertical shears in the E-W wind. However, the ion convergence in our case is maximum near the equator as pointed out earlier also.

2.7 Conclusions:

A three dimensional model, for the interaction of small and medium scale size gravity waves with the ionospheric E region, was developed. In the model calculations, the east west and north south winds were assumed to be equal, with their velocity amplitude equal to 100 m/sec. The high lights of the present studies are as follows.

(i) For the medium and small scale size gravity waves with the wavelength λ_x, along the geomagnetic field lines less than about 200 km, the curvature of the geomagnetic field lines can be ignored and hence, the geomagnetic field can be assumed to be homogenous.

(ii) The wavelength, λ_x of the gravity waves, parallel to the geomagnetic field, is very important to the generation of net electric field $\underline{E}^W$ in the wind frame of reference. The polarization fields $\underline{E}$, above 90 km are substantially shorted, even at the equator, if λ_x is finite, implying $\underline{E}^W$ to be large.

(iii) The efficiency factor R, for the generation of net electric field, was found to be much larger than that obtained earlier.

(iv) The gravity wave driven currents in the east west direction were found to be a significant fraction of the main electrojet currents, even at the peak of the electrojet. These currents, together with the electrojet current, may satisfy the threshold requirement for the excitation of the two stream plasma instability in localised regions.

(v) The gravity waves give rise to strong field aligned currents which were found to peak around 130 km altitude. The streaming velocity of the electrons was found to be sufficiently large as to excite the ion cyclotron instability in the 130 km altitude region.

(vi) The gravity waves can converge the ionization at the equator also, giving rise to the ionization layers in the nighttime. The ion convergence rates below 120 km at the equator, were found to be larger than those in the mid latitudes. Therefore, the gravity wave winds would be, at least, as effective at the equator as they are believed to be in the mid latitudes in forming the ionization layers.

(vii) The ion convergence in the lower E region was found to be due to the vertical shears in the east west wind. The ion convergence rates at 100 km at the equator due to the gravity wave winds were found to be much larger than those given earlier.

CHAPTER III

GENERATION AND TRANSMISSION OF SMALL SCALE ELECTROSTATIC FIELDS IN THE IONOSPHERE

3.1 Introduction

Electron density irregularities in the equatorial F region has been a topic of great interest ever since the discovery of Spread-F was made by Berkner and Wells (1934). Dagg (1957) proposed that these irregularities are first generated in the E-region and transmitted to the F-region via highly conducting geomagnetic field lines. This suggestion was intimately connected to that of Martyn (1955) who proposed that the large scale electric fields in the E-region are transmitted to the F-region via the highly conducting geomagnetic field lines. Farley (1959, 1960) studied the dynamical coupling between the E and F-regions for electric fields of small scale sizes. To account for the source of electric fields of small scale sizes, he used a system of horizontal winds which were derivable from a stream function. The source region was assumed to have a very small vertical extent such that the parallel conductivity within the source region was assumed to be constant. The electrostatic coupling between the equatorial F region and low latitude E region was provided through the geomagnetic field lines which were assumed to be parabolic. His studies showed that

(i) Electrostatic coupling between the E and F region may exist at all latitudes, the effect being weakest at the equator.

(ii) The electrostatic source field strength will usually be considerably less than the $\underline{W} \times \underline{B}$ field where $\underline{W}$ is the neutral wind and $\underline{B}$ is the geomagnetic field. The source field is maximum at 45° dip latitude and decreases on either side of it.

(iii) No electron density variations could be produced at the poles. At lower latitudes some fluctuations in electron density could be produced, but they would probably be too weak to be significant.

Hence he concluded that the Dagg's suggestion is not at all satisfactory.

Farley assumed, in the determination of these solutions that the distribution of the electrostatic potential is symmetric about the equatorial plane. This condition corresponds to apriori assumption that no current flows across the equatorial plane, and requires that the field generating mechanism operative in the dynamo region produces identical electric fields at the conjugate points in the two hemispheres of the earth. This condition was much too unrealistic, as was realised by Sprieter and Briggs (1961); for their is no qualifying reason to believe that the small scale electric fields produced by irregular winds be symmetrical with respect to the equator. Sprieter and Briggs (1961) considered that the mechanisms that operate to generate electric fields at the conjugate points function independently and the linearity of the equations assures that the properties of the fields generated in each hemisphere can be treated separately. The appropriate boundary condition for the other hemisphere being that owing to a very small conductivity at the base of the ionosphere, current vanishes at the bottom of the ionosphere.

But they did not propose any mechanism for the generation of small scale electric fields in the source region. Their calculations were only for the attenuation of the electric fields during their transmission.

Reid (1968) proposed that the Dagg's suggestion may still work if the source region is considered to be "thick". He proposed that if the whole region from 100 km to 140 km altitude is considered as the source region, it could generate electric fields which are essentially in phase. So that the short circuiting effect, to be expected from the varying winds, does not arise. However, he did not examine the idea quantitatively.

Thus the earlier studies could not establish the efficiency of neutral winds in generating small scale electric fields on a strong footing. In the previous chapter we have summarized the works of Kato (1973) and Anandarao et al (1977) in generation of electric fields due to the gravity wave winds. Also, pointing out the short comings of these model we developed a three dimensional model for the interaction of gravity wave winds with the ionosphere plasma. These studies showed that the electric fields can be generated by the gravity wave winds under certain conditions. In that, the importance of the wavelength parallel to the geomagnetic field lines was realised for the generation of the electric fields. In this chapter, we investigate rigorously, the problem of generation of electric fields due to the three dimensional gravity wave winds in the low latitude ionosphere, and the transmission of these fields to the other regions of the ionosphere. In the present investigations, the geomagnetic field line curvature has been taken into account. The following is the brief outline of this chapter.

In section 3.2 the geometry of the geomagnetic field line is described.

In section 3.3, the variation of wave numbers k_x and k_z with the dip angle is given. It is found that the wave number (k_x) parallel to the field line varies rapidly with the dip angle, going from positive to negative. The variation in k_z is, however, negligibly small over a large range of dip angles.

In section 3.4, the nature of the gravity wave winds has been studied. It is found that, on a given field line, the wind varies symmetrically around the point where $k_x = 0$. The wind remains in the same direction over a large distance along $\underline{B}$ around the point where $k_x = 0$, and further away from it, it varies sinusoidally with decreasing wavelength on either side of this region.

In section 3.5, it is shown that the region where $k_x \sim 0$ defines the source region of the electric field. It is found that the vertical wave length of the gravity wave winds determines the extent of the source region.

In section 3.6, the theory of generation of electric fields due to the gravity wave winds is developed using the assumed form of the potential and the generalised Ohm's law. A set of second order partial differential equations in potential (corresponding to the real and imaginary parts) is thus obtained. On the basis of physical arguments, this set of equations is reduced to a single equation. Boundary conditions and the numerical method employed for solving these equations are also discussed in this section.

In section 3.7, the conductivity profiles (for different times of the day) used for the calculations are given.

In section 3.8, approximate solutions, giving information on the generation and attenuation of electric fields are obtained.

In section 3.9, by meeting the condition $k_x = 0$ in different regions of the ionosphere, the electric field in the source region is calculated for a variety of cases. Thus the condition for the most efficient generation of the electric fields is obtained.

In section 3.10, a comparison is made of the results obtained using the sinusoidal winds (which are present everywhere) of section 3.4 with the constant winds present only around the region where $k_x = 0$. The results of the two cases are found to be in good agreement.

In section 3.11, detailed calculations have been made on the generation and attenuation of electric fields due to the gravity wave winds of different vertical wave lengths under a variety of situations.

Fig.3.1 defines the coordinate systems used in this investigation. The coordinate system x' y' z' is such that x' and y' are horizontal pointing towards magnetic north and magnetic west respectively, and z' is in the vertically upward direction. In this coordinate system, the gravity wave winds are normally defined. In another coordinate system, x axis is along $\underline{B}$, y axis is parallel to y' axis and z axis is in the plane perpendicular to the xy plane and is upwards.

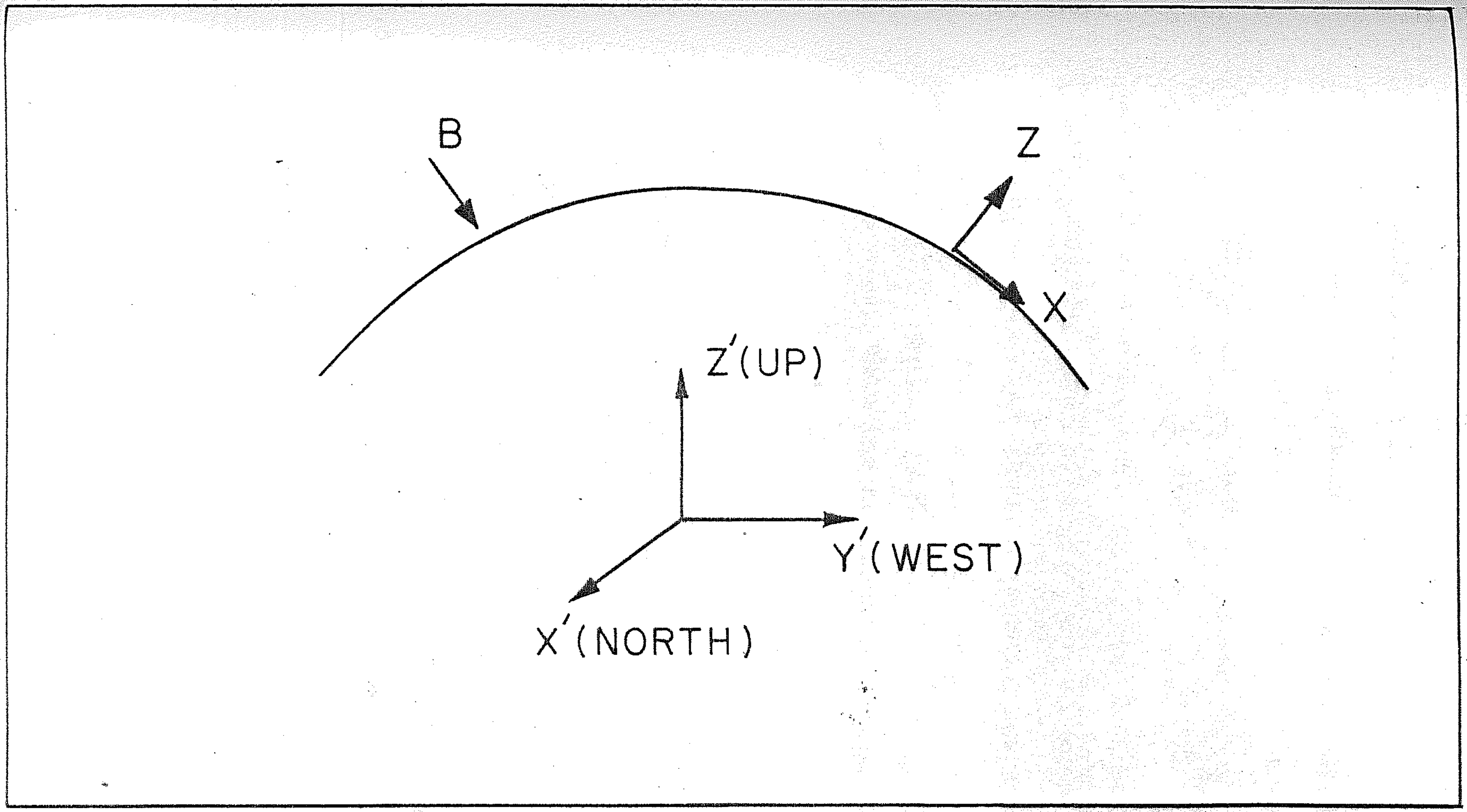

FIG. 3·1

3.2 Geomagnetic Field Line Geometry

We use the geomagnetic field line geometry as envisaged by Farley (1960). From the dipole approximation of the field line we have

$$\tan I = 2 \tan L \tag{1}$$

where I is the dip angle and L is the latitude. The latitude L is given by $L = x'/R$, where x' is the horizontal distance from the equator and R is the radius of the earth. Thus for small L we get,

$$\tan I = 2x'/R \tag{2}$$

If I is small then the horizontal distance x' is equal to the distance x along the field line. Using these facts we get

$$dx = \frac{R}{2} dI \tag{3}$$

The equation of the field line is given by

$$Z_f - Z = x^2/R \tag{4}$$

where Z_f is the altitude of the field line at the equator and Z is the altitude which it crosses at a distance of $x'(x)$ from the equator.

3.3 Variation of Wave Numbers with Latitude

Variation of the wave vector components with the latitude can be studied using the expression (see chapter II),

$$\begin{aligned} k_x &= k_x' C - k_z' S \\ k_z &= k_z' C + k_x' S \\ k_y &= k_y' \end{aligned} \tag{5}$$

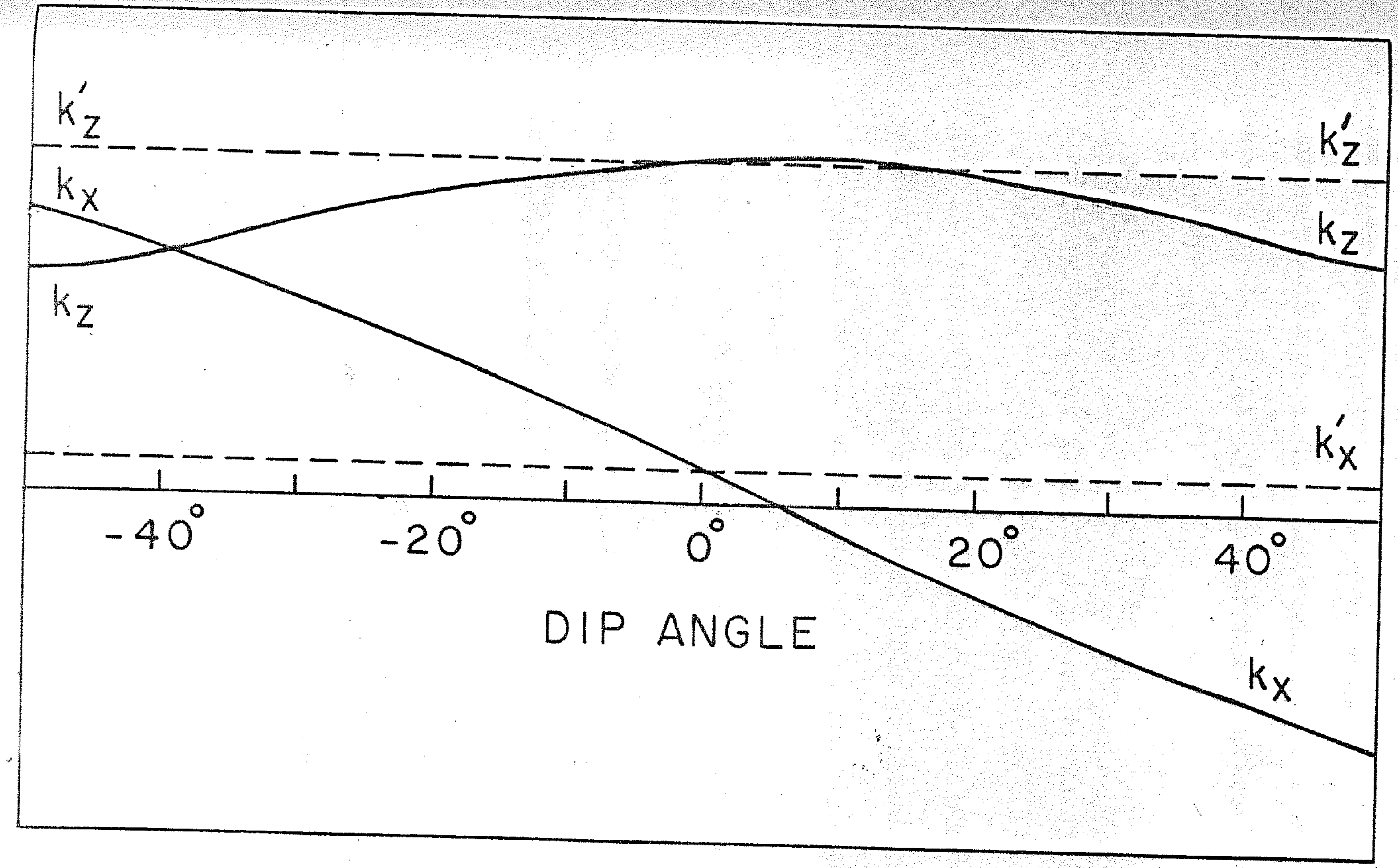

FIG. 3·2

where C = $\cos I$ and S = $\sin I$, I is the dip angle. From the above expressions, it can be seen that for a gravity wave, with given wave vector components k'_x and k'_z, there is always a dip angle where $k_x = 0$. Let this dip angle be I_0. At this point (here after referred to as point S) we have

$$\tan I_0 = k'_x / k'_z \qquad (6)$$

As one moves away from this point k_x is finite. Since the ratio k'_x / k'_z can have practically any value for different gravity waves(Hines, 1960), it is possible to realise $k_x = 0$ at any desired dip latitude. For a fixed ratio of k'_z and k'_x equal to 10, variation of k_x and k_z with dip angle is shown in fig.3.2. It can be seen from this figure that while variation of k_x from -30° to + 30° dip angle is quite large, variation of k_z over the same range of dip angle is quite small and can be neglected.

3.4 The Nature of the Winds

Therefore the wind, say W_y, has the form

$$W_y = W_{0y} \exp\left\{ i \left(\int k_x dx + k_y y + k_z z - \Omega t \right) \right\} \qquad (7)$$

In the neighbourhood of point S, the concept of wavelength along B is lost. To study the wind pattern around the point S, it is quite instructive to study the phase of the wind W_y at various points along a field line with respect to its phase at the point S. This can be done by evaluating

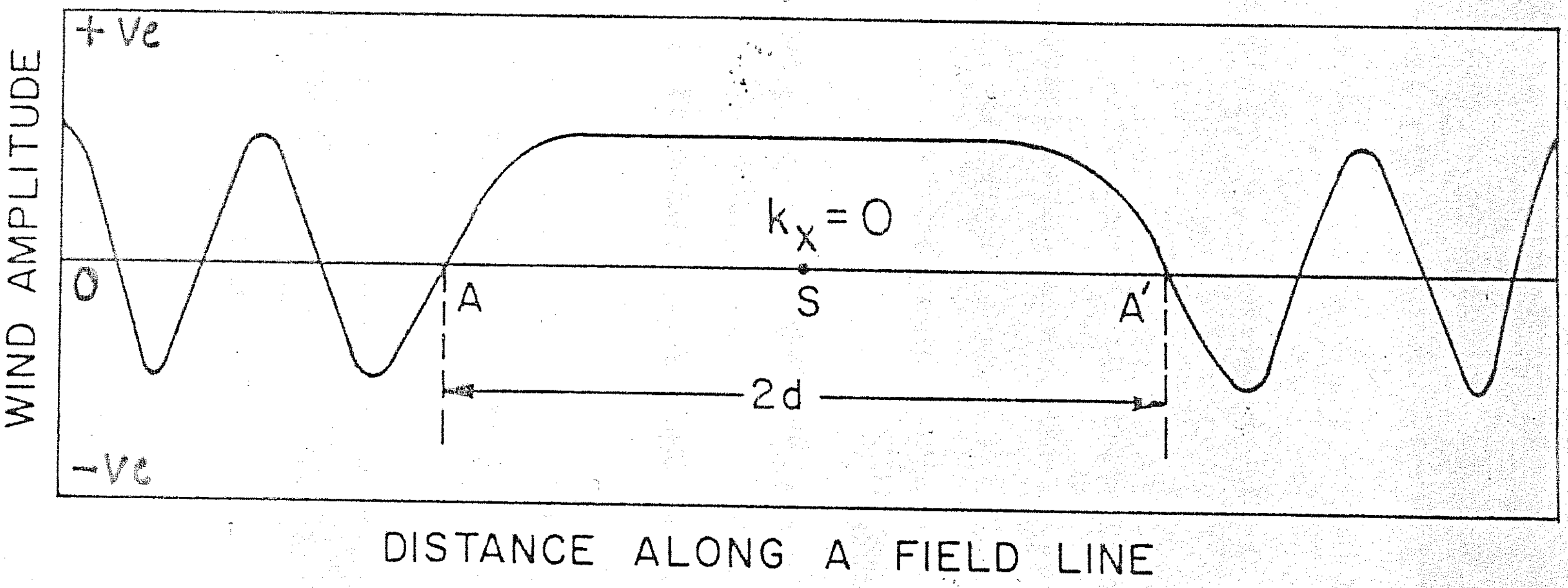

Fig. 3.3: Schematic variation of wind amplitude around $k_x = 0$ point on a given field line.

the expression $\int_{x_0}^{x} k_x\,dx$, where x_0 and x are the distance of the point S and the given point respectively, with respect to some reference point on a given field line. Using eqns. (3) and (5) we get,

$$\int k_x dx = \int R(k'_x c - k'_z s)\,dx \qquad (8)$$

$$\therefore \int k_x dx = \frac{k_z R}{2}\,|\mathrm{Sec}\, I_0|\,(I_0 - I)^2 \qquad (9)$$

It can be seen from eqn (9) that the phase of the wind varies symmetrically around the point S, or in other words around the dip angle I_0 where $k_x = 0$. For an initial phase of zero at the point S, the wind pattern around the point S is shown in fig.3.3. It can be seen from this figure that the wind around the point S remains in the same direction over a large distance and then it varies sinusoidally with decreasing wavelength on either side of the point S.

The same situation is realised, more clearly, from fig.3.4. In this figure, different wave fronts at a given time with $k_x = 0$ and phase of $(n\pi + \pi/2)$, where n is an integer are drawn intersecting a pair of field line at different points. The solid areas enclosed by the pair of the field lines denote that the wind is positive in these regions. Blank areas denote that the wind is in opposite direction, that is, negative.

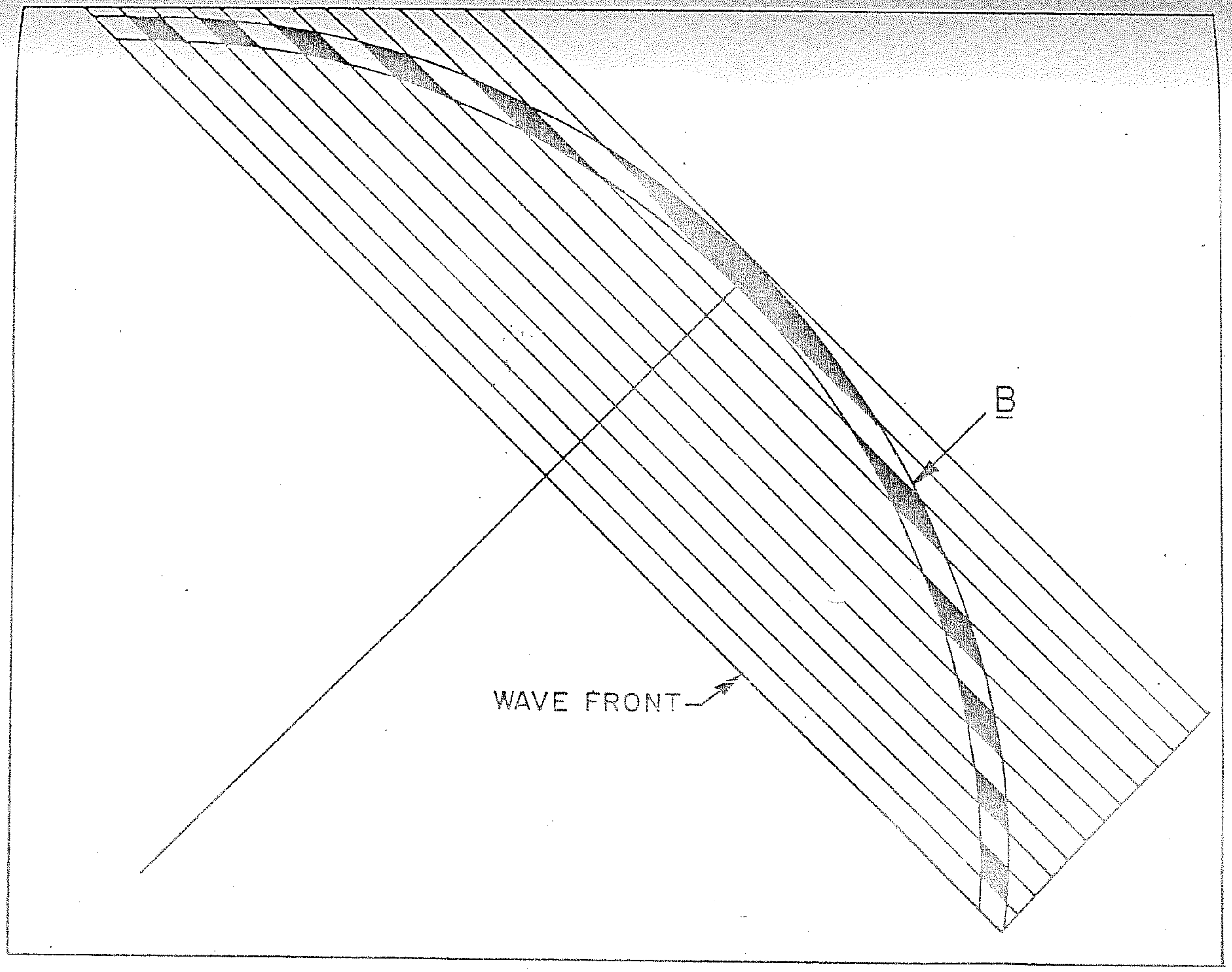

WIND PATTERN ALONG $\underline{B}$ (SCHEMATIC)

Fig. 3.4

3.5 The Source Region

The distance 2d (± d on either side of the point S) over which the phase of the wind remains within $\pi/2$ with respect to its initial phase at the point S, can be calculated using eqn.(9) and is given by

$$2d = \left\{ R\lambda_z |\cos I_0| \right\}^{1/2} \qquad (10)$$

$$\lambda_z = 2\pi \left(k_x'^2 + k_z'^2 \right)^{-1/2} \qquad (11)$$

For small I_0 eqn.(10) can well be approximated to

$$2d = (2R\lambda_z)^{1/2} \qquad (12)$$

Thus for R = 6400 km and λ_z = 16 km we get

$$2d = 320 \text{ km} \qquad (13)$$

As has been discussed in chapter II, although the alternating winds give rise to alternating electric field along B, they get shorted due to the fact that the ratio σ_0/σ_P is very large. σ_0 and σ_P are the parallel and Pedersen conductivities, respectively.

Since the undirectional winds in the region AA′ (see fig. 3.3) do not have their counter part anywhere on the given pair of field lines, they alone contribute to the production of an electric potential. Thus, the winds in the region AA′ serve as the source of an electric field, that is, the region AA′ is the dynamo region. The complete region of the ionosphere connected with the field lines serves as a load to this potential. Hence, the distance 2d, over which the winds are unidirectional around the point S, defines the extent of the source region along $\underline{B}$. From eqn.(12) it can be seen that the perpendicular wavelength Λ_z is very important in determining the extent of the source region. Since the vertical wavelength of the gravity wave winds expected to be present in the E and F regions is, of the order of 10 to 100 km, the dynamo region can extend to hundreds of kms along the field line.

3.6 Theory

As has been pointed out earlier, that the charge excess along $\underline{B}$ due to the variational winds tends to short out, the electric potential produced due to such a wind will not have the same variational form along $\underline{B}$ as that of the wind. The electric potential due to such a wind can therefore be assumed to be of the form

$$\phi = \phi_0(x) \exp\{i(k_y y + k_z z - \Omega t)\} \qquad (14)$$

where $\phi_0(x)$ varies monotonically with x. If the polarization fields are assumed to be electrostatic then,

$$\underline{E} = -\nabla\phi \qquad (15)$$

The electric current due to an electric field $\underline{E}$ and wind $\underline{W}$ is given by

$$\underline{J} = \sigma_0 \underline{E}_{\parallel} + \sigma_P\{\underline{E}_{\perp} + (\underline{W} \times \underline{B})_{\perp}\} + \frac{\sigma_H}{|\underline{B}|}\{\underline{B} \times (\underline{E} + \underline{W} \times \underline{B})_{\perp}\} \qquad (16)$$

where $\parallel$ and $\perp$ denote the components parallel and perpendicular to $\underline{B}$, and σ_0 , σ_P and σ_H are the parallel, Pedersen and Hall conductivities respectively. Using the above set of equations and imposing the condition

$$\nabla \cdot \underline{J} = 0 \tag{17}$$

the following second order partial differential equation is obtained

$$\begin{aligned} \sigma_0 \frac{\partial^2 \phi_0}{\partial x^2} + \frac{\partial \sigma_0}{\partial x} \frac{\partial \phi_0}{\partial x} &= \left\{ \sigma_P (k_y^2 + k_z^2) - i \left(k_z \frac{\partial \sigma_P}{\partial z} + k_y \frac{\partial \sigma_H}{\partial z} \right) \right\} \phi_0 \\ &+ B \left\{ i \sigma_P (k_y W_{0z} - k_z W_{0y}) - i \sigma_H k_x W_{0x} - W_{0y} \frac{\partial \sigma_P}{\partial z} \right. \\ &\left. + W_{0z} \frac{\partial \sigma_H}{\partial z} \right\} \exp (i \textstyle\int k_x dx) \end{aligned} \tag{18}$$

wherein we have used the fact that $\nabla \cdot \underline{W} = 0$ (19). Eqn.(18) can be further simplified if the terms with gradients in Pedersen and Hall conductivities are ignored in comparision to k_z . This requires that

$$k_z > \frac{1}{\sigma_P} \frac{\partial \sigma_P}{\partial z} \tag{20}$$

Even if the σ_P scale length during the day time and the night time is taken to be 50 km and 6 km respectively, these are smaller than the wave number k_z corresponding to a wavelength of 25 km. If the wavelength is smaller, then the neglect of these terms is more justified. Neglecting these we get,

$$\sigma_0 \frac{\partial^2 \phi_0}{\partial x^2} + \frac{\partial \sigma_0}{\partial x}\frac{\partial \phi_0}{\partial x} = \sigma_P (k_y^2 + k_z^2) + B\{ i\sigma_P (k_y W_{0z} - k_z W_{0y}) - i\sigma_H k_x W_{0x}\} \exp(i\int k_x dx) \qquad (21)$$

If $\phi_0 = \phi_{01} + i\,\phi_{02}$ (22)

From eqn.(21) we get following two equations

$$\sigma_0 \frac{\partial^2 \phi_{01}}{\partial x^2} + \frac{\partial \sigma_0}{\partial x}\frac{\partial \phi_{01}}{\partial x} = \sigma_P (k_y^2 + k_z^2)\phi_{01} - B\{\sigma_P (k_y W_{0z} - k_z W_{0y}) - \sigma_H k_x W_{0x}\} \sin(\int k_x dx) \qquad (23)$$

$$\sigma_0 \frac{\partial^2 \phi_{02}}{\partial x^2} + \frac{\partial \sigma_0}{\partial x}\frac{\partial \phi_{02}}{\partial x} = \sigma_P (k_y^2 + k_z^2)\phi_{02} + B\{\sigma_P (k_y W_{0z} - k_z W_{0y}) - \sigma_H k_x W_{0x}\} \cos(\int k_x dx) \qquad (24)$$

Since $k_z >> k_y$ and $W_{0y} > W_{0z}$ for the gravity wave winds, eqns.(23) and (24) can be further simplified and we get,

$$\frac{\partial^2 \phi_{01}}{\partial x^2} + \frac{1}{\sigma_0}\frac{\partial \sigma_0}{\partial x}\frac{\partial \phi_{01}}{\partial x} = \frac{\sigma_P}{\sigma_0} k_z^2 \phi_{01} + B\left\{\frac{\sigma_P}{\sigma_0} k_z W_{0y} + \frac{\sigma_H}{\sigma_0} k_x W_{0x}\right\} \sin(\int k_x dx) \qquad (25)$$

$$\frac{\partial^2 \phi_{02}}{\partial x^2} + \frac{1}{\sigma_0}\frac{\partial \sigma_0}{\partial x}\frac{\partial \phi_{02}}{\partial x} = \frac{\sigma_P}{\sigma_0} k_z^2 \phi_{02} - B\left\{\frac{\sigma_P}{\sigma_0} k_z W_{0y} + \frac{\sigma_H}{\sigma_0} k_x W_{0x}\right\} \cos(\int k_x dx) \qquad (26)$$

Representing the potential in terms of a dimension less quantity ψ , such that

$$\psi = \psi_1 + i\,\psi_2 \tag{27}$$

$$|\psi| = (\psi_1^2 + \psi_2^2)^{1/2}$$

where

$$\psi_1 = k_z\,\phi_{01}/BW_{0y} \tag{28}$$

$$\psi_2 = k_z\,\phi_{02}/BW_{0y}$$

Equations (25) and (26) thus reduce to

$$\frac{\partial^2\psi_1}{\partial x^2} + \frac{1}{\sigma_0}\frac{\partial\sigma_0}{\partial x}\frac{\partial\psi_1}{\partial x} = \frac{\sigma_P}{\sigma_0}(k_y^2 + k_z^2)\,\psi_1 + k_z\left\{\frac{\sigma_P}{\sigma_0}(k_z - k_y W_{0z}/W_{0y}) + \frac{\sigma_H}{\sigma_0}k_x W_{0x}/W_{0y}\right\} \sin\left(\int k_x\,dx\right) \tag{29}$$

$$\frac{\partial^2\psi_2}{\partial x^2} + \frac{1}{\sigma_0}\frac{\partial\sigma_0}{\partial x}\frac{\partial\psi_2}{\partial x} = \frac{\sigma_P}{\sigma_0}k_z^2\,\psi_2 - k_z\left\{\frac{\sigma_P}{\sigma_0}(k_z - k_y W_{0z}/W_{0y}) + \frac{\sigma_H}{\sigma_0}k_x W_{0x}/W_{0y}\right\}\cos\left(\int k_x\,dx\right) \tag{30}$$

The dimensionless quantity ψ represents the ratio of the vertical polarization field to the wind induced field in that direction. At the point S, since $k_x = 0$ using eqn.(19) we get,

$$k_z/W_{0y} = -k_y/W_{0z} \tag{31}$$

From the above expression it is clear that ψ_1 and ψ_2 can also be used to represent the electric field in the y direction. Thus E_y and E_z both can be determined from ψ_1 and ψ_2 .

Further simplification for the solution of eqns.(29) and (30) can be sought on the following physical reasoning. Since it is the wind around the point S which contributes predominantly to the generation of electric field, the wind effect being cancelled out in the other regions due to its variational form; it may as well be assumed that a constant wind is present only in the region around the point S which is as effective in generating electric field as is the variational wind of fig.3.3. Therefore, if we consider the constant wind only around the point S where $k_x \sim 0$, we get only one equation corresponding to eqn.(30) which contains the source term (wind term) and is given by

$$\frac{\partial^2 \psi_2}{\partial x^2} + \frac{1}{\sigma_0}\frac{\partial \sigma_0}{\partial x}\frac{\partial \psi_2}{\partial x} = \frac{\sigma_p}{\sigma_0}(k_y^2 + k_z^2)\psi_2$$
$$- k_z \left\{ \frac{\sigma_p}{\sigma_0}(k_z - k_y W_{0z}/W_{0y} \right\} \qquad (32)$$

The equation in ψ_1 corresponding to eqn.(29) is not significant as it does not contain the source term. This equation gives information only on the attenuation of the field. To justify this approach, results obtained with the set of eqns.(29) and (30) were compared with those obtained using eqn.(31) alone. It was found that the results obtained with the latter case were closely representing the results obtained with the former set of equations, as will be discussed later. It may be remarked here that this approach is fully justified for gravity waves having large vertical wavelengths.

3.6.1 Boundary Conditions

Eqn.(32) can be solved using a step by step numerical method if the initial conditions viz $(\psi_2)_{x=0}$ and $(\partial\psi_2/\partial x)_{x=0}$ are known. Due to very low conductivity in the lower E region, say at 90 km, it is quite reasonable to assume that the parallel current vanishes, in both the hemispheres, at and below this altitude (Sprieter and Briggs, 1961). It implies that $\partial\psi_2/\partial x = 0$ at the boundaries of the ionosphere. So the two boundary conditions are obtained with this physical argument. To make the problem an initial value problem, various values of ψ_2 were tried at the initial point (with $\partial\psi_2/\partial x = 0$) until the correct solution giving $\partial\psi_2/\partial x = 0$ at the other boundary was obtained.

3.6.2 Numerical Method

To minimise the number of steps to obtain the correct solution, a novel method was employed. It is based on the method of logrithmic fractionation. In this method the value of ψ_2 is chosen to be 1 at the initial point which is evidently the largest possible value of ψ_2. Using this as the initial value, the complete solution is obtained. Then this value is decreased in accordance with the formula

$$\psi_2 = (\psi_2)_{initial}\ 10^{(-k + l/5 - m/25 + n/125)} \qquad (33)$$

where k, l, m and n are integers with values ranging from 0 to 5. Keeping the values of l, m and n zero, the k value is increased until the sign of $\partial\psi_2/\partial x$ changes at the other boundary. This value of k is then frozen and the value of l is increased, keeping m and n zero, until $\partial\psi_2/\partial x$ at the other boundary again changes sign. Similarly, m and n values are increased keeping other variables (k,l,n or k,l and m) constant. The correct solution is intermediate to the solutions in which, with the increase of n value, the sign of $\partial\psi_2/\partial x$ changes at the other boundary. The uncertainty in the value of ψ_2 at the initial point is about 2%.

Fourth order Runga-Kutta method with Adam-Baschforth predictor - corrector for the successive values was employed to solve the differential equation. The accuracy demanded of the solution was upto the sixth decimal place. The step size, during the calculations, was automatically decreased to give the desired accuracy.

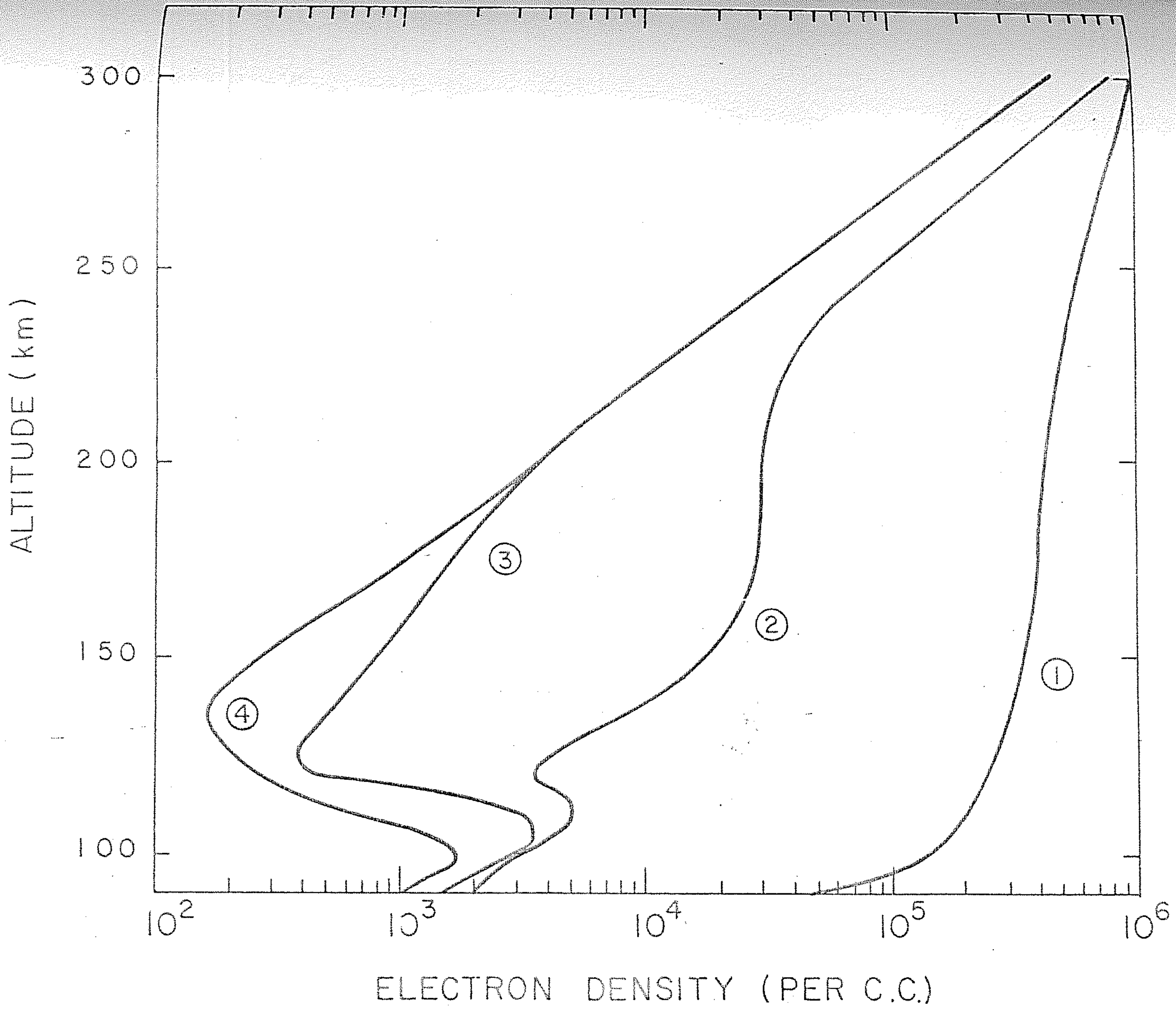

Fig. 3.5: Electron density profiles used for calculating the conductivity profiles for different times of the day.

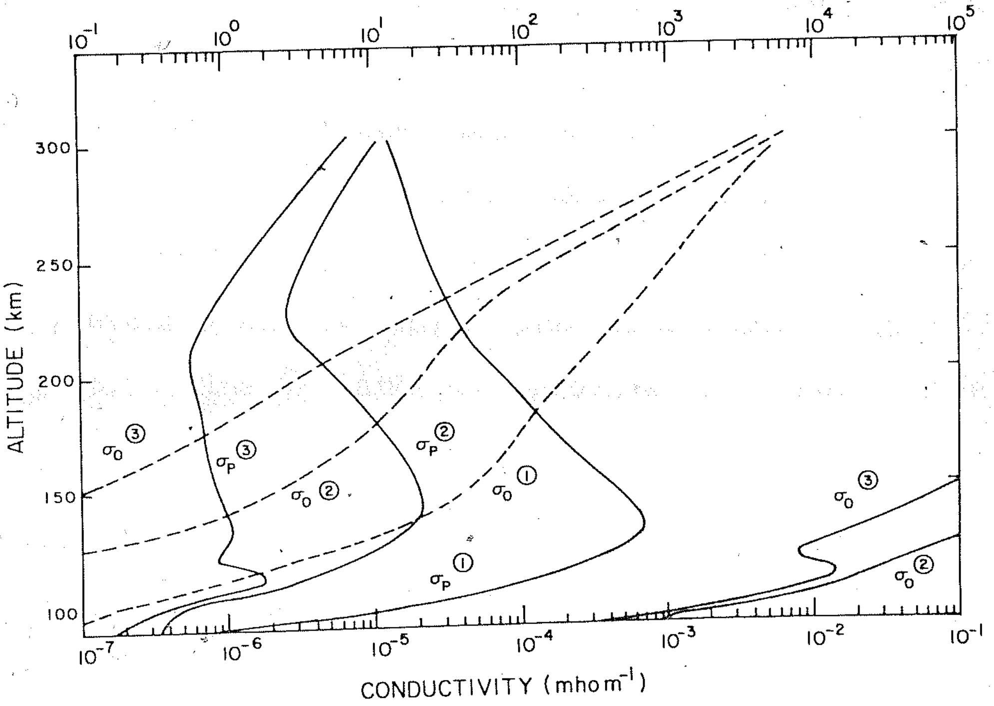
10^{-1}
10^{0}
10^{1}
10^{2}
10^{3}
10^{4}
10^{5}
ALTITUDE (km)
300
250
200
150
100
σ_0 ③
σ_P ③
σ_0 ②
σ_P ②
σ_0 ①
σ_P ①
σ_0 ③
σ_0 ②
10^{-7}
10^{-6}
10^{-5}
10^{-4}
10^{-3}
10^{-2}
10^{-1}
CONDUCTIVITY (mho m^{-1})

FIG. 3-6

3.7 The Conductivity Profiles

Calculations were carried out for the daytime, evening time and two night time conditions. As the electron density profile, on which the conductivity profiles are mainly dependent, is highly variable during the evening and night hours; no standard model of the electron density can be used. Based on various rocket launches from Thumba, India and elsewhere, and the ionosonde data available in the literature, four electron density profiles were built up representing the day, evening and two night time situations as given in fig. 3.5. The σ_0 and σ_p profiles for these different periods of the day are given in fig. 3.6.

3.8 Approximate Solutions

Before attempting to solve eqn.(32) rigorously for various cases, the general nature of the results can be studied using following approximations.

3.8.1 Attenuation

Outside the source region, dependence of ψ_2 on k_z and the attenuation length can be estimated by noting the importance of various terms in eqn.(32). In the region where $\partial\sigma_0/\partial x$ is small, i.e. around the apogee of the field line, the second term on the left hand side of eqn.(32)

can be neglected and we get

$$\frac{\partial^2 \psi_2}{\partial x^2} = k_z^2 \frac{\sigma_p}{\sigma_0} (\psi_2 - 1) \qquad (34)$$

whose solution is (ignoring the variation σ_p and σ_0 around the apogee of the file line)

$$1 - \psi_2 = (1 - \psi_0)\, \exp(\pm k_z \sqrt{\sigma_p/\sigma_0}\; x) \qquad (35)$$

Since away from the source region, the value of ψ_2 should decrease i.e. $(1-\psi_2)$ should be large, exponent in eqn.(35) should have the positive sign. The attenuation length of $(1-\psi)$ is, therefore

$$\frac{1}{L} = \frac{1}{(1-\psi_2)} \frac{\partial}{\partial x} (1 - \psi_2) = k_z \sqrt{\sigma_p/\sigma_0} \qquad (36)$$

Hence, around the apogee of the field line, for a given value of λ_z, the attenuation of the field depends on the square root of the ratio of σ_p and σ_0. If k_z is small, i.e. large λ_z, the attenuation of the field is small and vice versa.

If the first term on the left hand side of eqn.(32) is smaller compared to the second term, which is true in the E region, then the first term can be neglected and we get,

$$\frac{d \psi_2}{d x} = -\frac{\sigma_p}{\sigma_0} k_z^2 H (1 - \psi_2) \qquad (37)$$

where H is the scale height of σ_0 along B. Hence the attenuation length, in this case, is given by

$$\frac{1}{L} = \frac{1}{(1-\psi_2)} \frac{\partial}{\partial x}(1-\psi_2) = H \frac{\sigma_P}{\sigma_0} k_z^2 \qquad (38)$$

Thus for a given value of λ_z, the attenuation length of $(1-\psi)$ in the E region depends on the ratio of σ_P and σ_0 and also on the scale height of σ_0 along B.

Solution of eqn.(37) is

$$1-\psi_2 = (1-\psi_c)\, \exp\left(\int H \frac{\sigma_P}{\sigma_0} k_z^2\, dx\right) \qquad (39)$$

Sign of the exponent in eqn.(39) depends on the sign of H, which on integration yields the logrithmic ratio of σ_0 in two regions and hence, is always positive. Thus away from the source region, the value of ψ_2 should decrease which is, indeed, true.

If k_z is small, i.e. large λ_z, it is clear from eqn.(39) that ψ_2 tends to ψ_c Hence, for large value of λ_z, the attenuation of the field is small. If k_z is large, then the term on the right of eqn.(39) has a large value, implying that $(1-\psi)$ has a largest possible value. Since ψ_2 is positive, it implies that the value of ψ_2 is very small. Hence for small values of λ_z, the attenuation of the field is large.

3.8.2 Generation of fields for large values of λ_z

Since for large values of λ_z, the attenuation of the field is very small, the electric field in this case can be assumed to be constant and its value can be estimated in the following way. The derivatives of the currents J_y and J_z are given by (see chapter II).

$$\frac{\partial J_y}{\partial y} = i\sigma_p k_y (E_y + BW_z) - i\sigma_H k_y (E_z - BW_y) \quad (40)$$

$$\frac{\partial J_z}{\partial z} = i\sigma_p k_z (E_z - BW_y) + i\sigma_H k_z (E_y + BW_z) \quad (41)$$

Adding eqns.(40) and (41), and using the facts that $\nabla . W = 0$ and $k_x = 0$ we get

$$\frac{\partial J_y}{\partial y} + \frac{\partial J_z}{\partial z} = i\sigma_p \{ k_y E_y + k_z E_z + B(k_y W_z - k_z W_y) \} - i\sigma_H (k_y E_z - k_z E_y) \quad (42)$$

The form of the potential ensures that the last term on the right hand side of eqn.(42) is **zero**. Also, $k_z >> k_y$ and $W_{0y} > W_{0z}$ for the gravity wave winds, we get

$$\frac{\partial J_y}{\partial y} + \frac{\partial J_z}{\partial z} \cong i\sigma_p (k_z E_z - Bk_z W_y) \quad (43)$$

since $\nabla . \underline{J} = 0$,

$$J_x = -i \int \sigma_p k_z (E_z - BW_y)\, dx \quad (44)$$

As shown in fig.3.7, if the region bounded between x_2 and x_3 is the source region (wind region), the current **flowing** outside the wind region depends on E_z only and

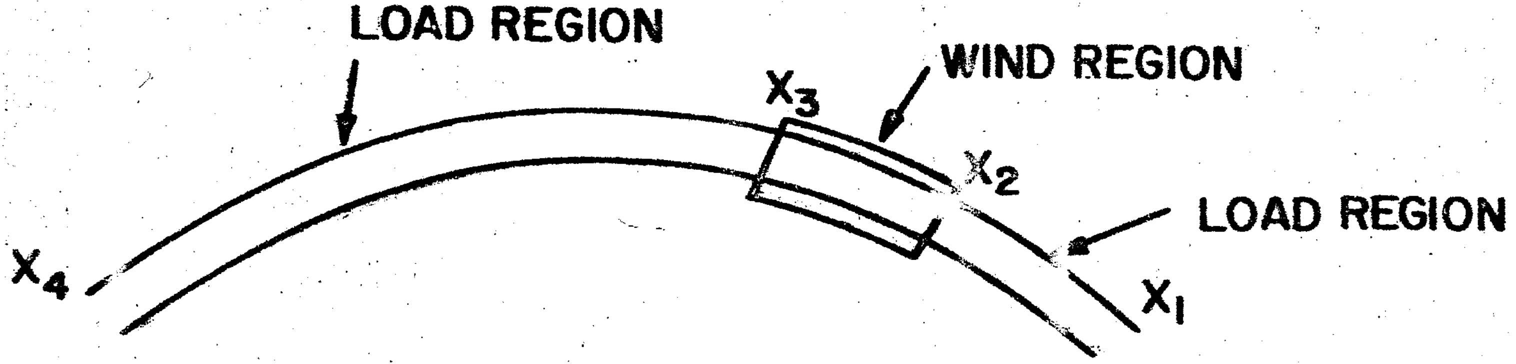

FIG. 3.7. SCHEMATIC DIAGRAM SHOWING THE WIND REGION AND THE LOAD REGION

is given by

$$J_x = -i k_z \left\{ \int_{x_4}^{x_3} \sigma_p E_z \, dx + \int_{x_2}^{x_1} \sigma_p E_z \, dx \right\} \qquad (45)$$

The current in the wind region is given by

$$J_x = -i k_z \int_{x_2}^{x_3} \sigma_p (E_z - B W_y) \, dx \qquad (46)$$

Since the current flowing outside the wind region should be equal to the current generated in the wind region, we get

$$\int_{x_4}^{x_3} \sigma_p E_z \, dx + \int_{x_3}^{x_2} \sigma_p E_z \, dx + \int_{x_2}^{x_1} \sigma_1 E_z \, dx = -B W_y \int_{x_2}^{x_3} \sigma_p \, dx \qquad (47)$$

Hence,

$$E_z = \frac{-B W_y \int_{x_2}^{x_3} \sigma_p \, dx}{\int_T \sigma_p \, dx} \; ; \quad \int_T \cdot \, dx = \int_{x_1}^{x_4} \cdots \, dx \qquad (48)$$

It is clear from eqn.(48) that, for large value of λ_z, the generated electric field depends on the ratio of integrated Pedersen conductivity in the source region to the total integrated Pedersen conductivity. If the wind region overlaps the region of maximum σ_p, larger field is generated. Also, since the extent of the wind region increases with λ_z, for large value of λ_z, the field is more.

3.9 Generation of Electric fields with $k_x = 0$ in Different Regions.

From the foregoing discussions it is clear that for large values of λ_z, E_z remains constant in the region bounded by a pair of field lines. This field is maximum when the wind region overlaps the region of maximum σ_p. An estimate of the generated field can also be made in this case. However, for small value of λ_z, the field can not be estimated and only qualitative information on the attenuation of the field can be obtained.

To ascertain the efficiency of generation of fields by the winds (of a given λ_z), calculations were carried out whence the centre of the wind region was shifted from the equator down to the region where a given field line crosses the 90 km altitude. The centre of the wind region was shifted by 100 km in successive calculations. It is worth while to point out here that the wind region, as defined in this analysis, implies the region over which $k_x \neq 0$. Two values of λ_z, namely 25 km and 4 km, were used for such calculations.

Figs.3.8 and 3.9 give the results of these calculations when the field line apogee is taken to be at 300 km and 200 km, respectively. The solid curves of these figures represent the results of the case when λ_z = 25 km while the dashed curves represent for the case when λ_z = 4 km. The curves marked 1, 2 and 3 represent the results for the day time, evening time and night time situations, as represented by the conductivity profiles of fig. 3.6. Lower scale of these figures gives the distance along field line as reckoned from the equator. For successive calculations, the winds were assumed to be present in different regions along such a field line. For a given location of the wind region, ψ_{max} denotes the maximum value of ψ for such a case. Vertical scale of these figures gives the value of ψ_{max}. Thus a point on these curves represents the maximum value of ψ (i.e. ψ_{max}) when the winds are centred around the point as obtained from the corresponding point on the lower scale. Along with the results of these calculations, a field line which drops from a given altitude (200 km or 300 km in these cases) at the equator is also plotted. Top scale of these figures gives the corresponding altitude which is crossed by this field line.

The altitude range covered by the winds when assumed to be present in different regions on a field line can be obtained using the field line geometry as given in these figures. The extent of the wind region, for a given λ_z , is given by eqn.(12). For example, if λ_z = 4 km, the wind region extends 80 km on either side of the centre of the wind region. If the apogee of the field line is at 300 km and the centre of the wind region is at 500 km, the wind region extends from 420 km to 580 km along the field line. The altitude range corresponding to this extent of the wind region is approximately 248 km to 272 km, as can be seen from fig.3.8.

3.9.1 Field line apogee at 300 km

We first discuss the results of the case when the field line apogee is taken to be at 300 km. Results of this case are shown in fig. 3.8. For the case when λ_z = 25 km, the

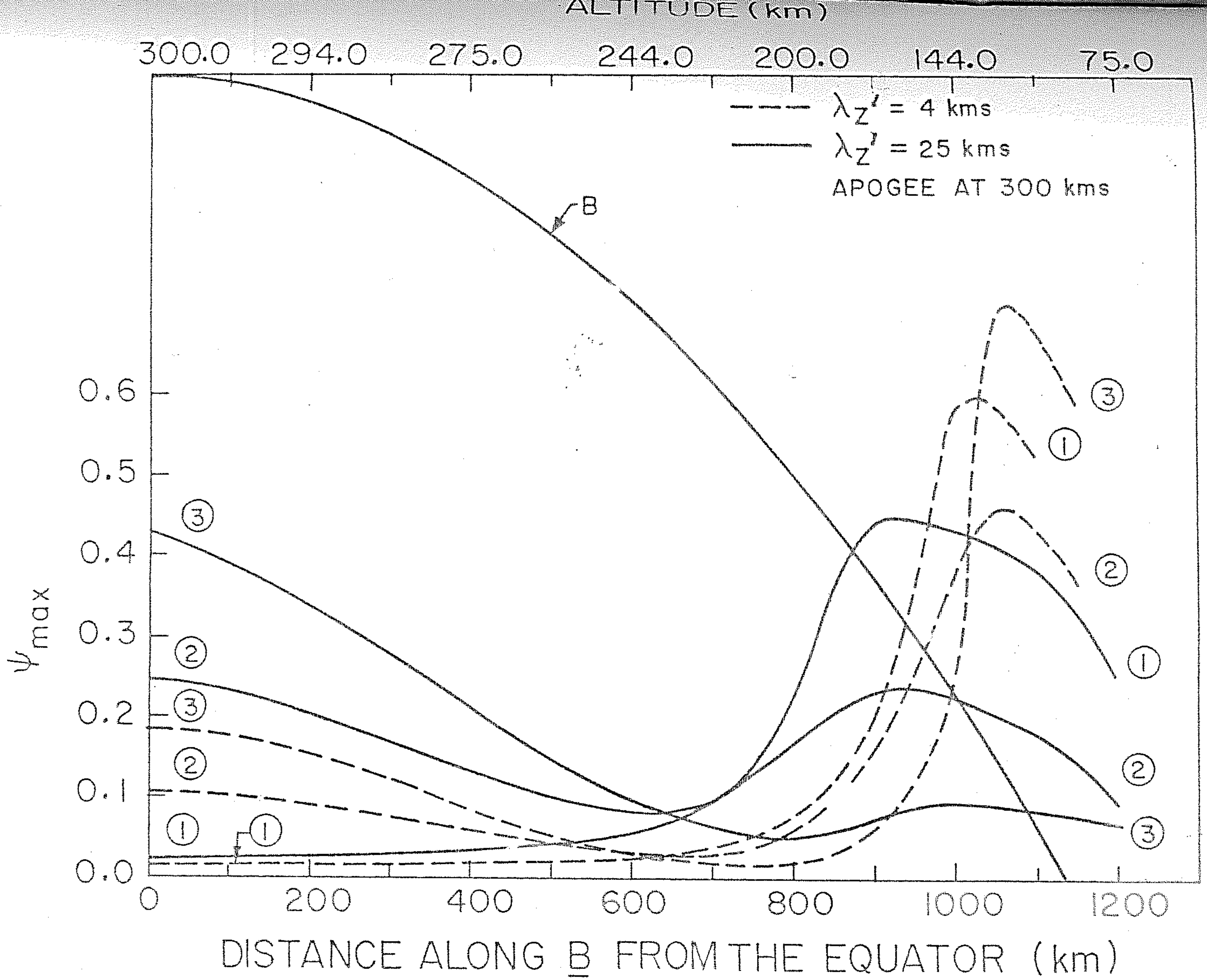

Fig. 3.8: Variation of ψ_{max} with distance along a field line. The curve marked B is the geomagnetic field line dropping from the equator at an altitude of 300 km (see top scale).

wind region has an extent of 400 km.

It can be seen from fig.3.8 that for λ_z = 25 km case, Ψ_{max} has the largest value at a distance of about 900 km from the equator (i.e.in the E region) for the daytime case whereas it is maximum around the equator (i.e. in the F region) for the night time case. The Evening time case has two maxima, in the F region and in the E region, respectively. These results are in accordance with the σ_p profiles (fig. 3.6) in which, for the daytime case σ_p is maximum in the E region while it is maximum in the F region for the night time case. For the evening time case, σ_p values in the 140 km and 300 km regions are almost equal.

For a source region with an extent of 400 km, it was found that the integrated σ_p along a field line, $\int_S \sigma_p dx$ is maximum in the region around 900 km for the day time case, around the equator and 900 km for the evening time case. The ratio of $\int_S \sigma_p dx$ to the total integrated σ_p , $\int_T \sigma_p dx$ (when the source is assumed to be situated around the regions mentioned above) comes out to be about 0.45, 0.40, and 0.25 for the day time, night time and evening time situations respectively. These values are close to the maximum value of Ψ_{max} for these situations.

Results of the case when λ_z = 4 km are also given in fig. 3.8. These results are essentially similar to the ones obtained in λ_z = 25 km case, except for the night time situation. In the night time case, Ψ_{max} has a maxima in the

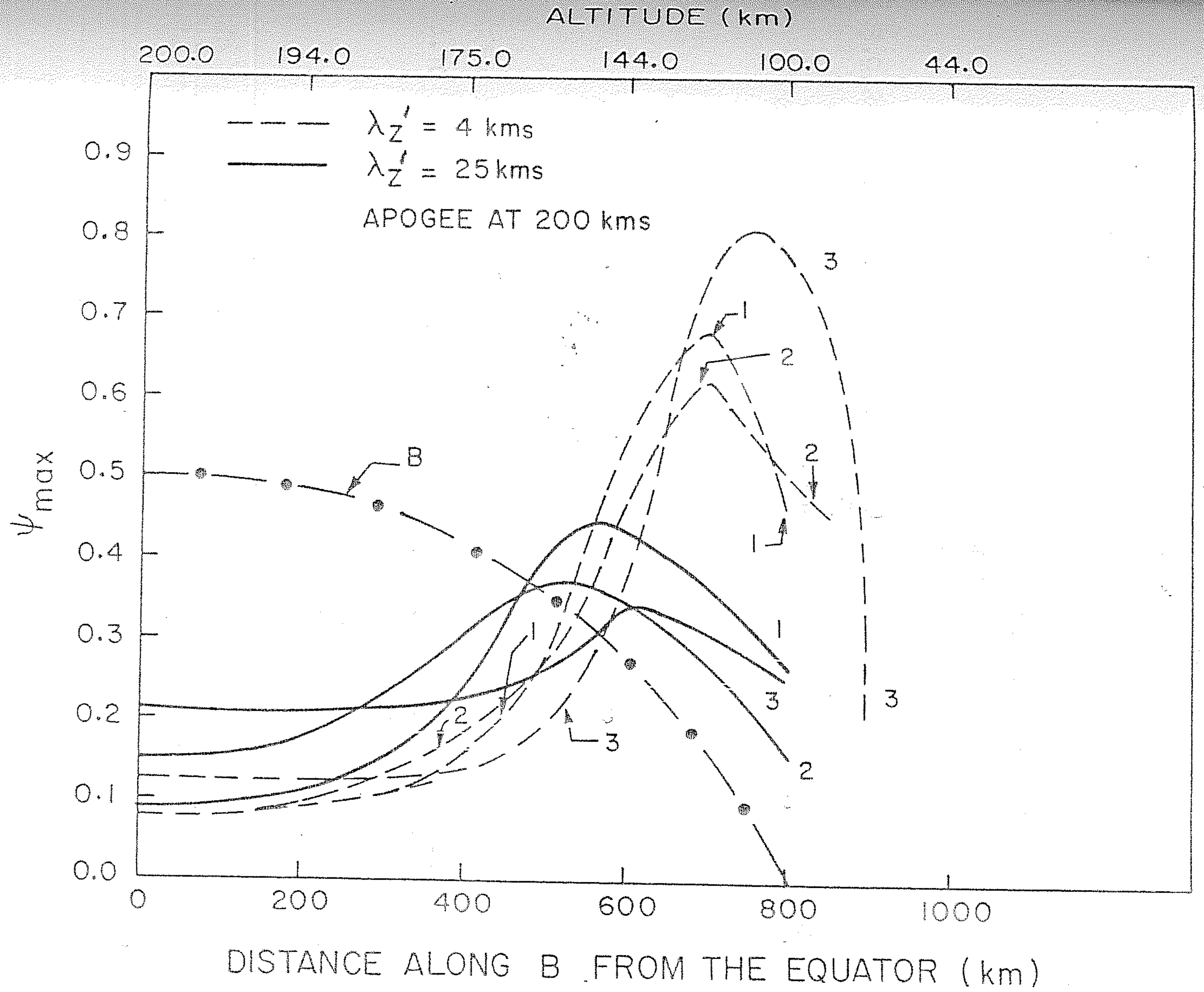

Fig. 3.9: Variation of Ψ_{max} with distance along a field line. (The field line apogee is at 200 km in this case.

E region also. This is owing to the shape of the σ_p profile in the night time, which has a peak in the E region. Effect of this shape of σ_p is suppressed (but is still visible) in λ_z = 25 case. This suppression is owing to larger length of the source region.

For λ_z = 4 km case, the maximum value of ψ_{max} for different times of the day, is more than that obtained for respective times in λ_z = 25 km case. It implies that for smaller λ_z, the field in the source region is larger.

3.9.2 Field line apogee at 200 km

Results of the case when the field line apogee is at 200 km are presented in fig. 3.9. It can be seen from fig.3.6 that σ_p has the largest value in the E region. Hence the value of ψ_{max} is expected to be largest only in the E region. It is indeed so, as can be seen in fig.3.9. Rest of the features of the results for this case are qualitatively similar to the ones obtained in section 3.9.1.

3.10 Comparison of Results - Constant Wind Case and Sinusoidal Wind Case

We now compare the results obtained using the set of eqns.(29) and (30) with those obtained using eqn.(32) alone. This comparison is necessary to show that the constant winds around the region where $k_x = 0$ are as effective in generating electric fields as are the sinusoidal winds of section 3.4 (Fig.3.3).

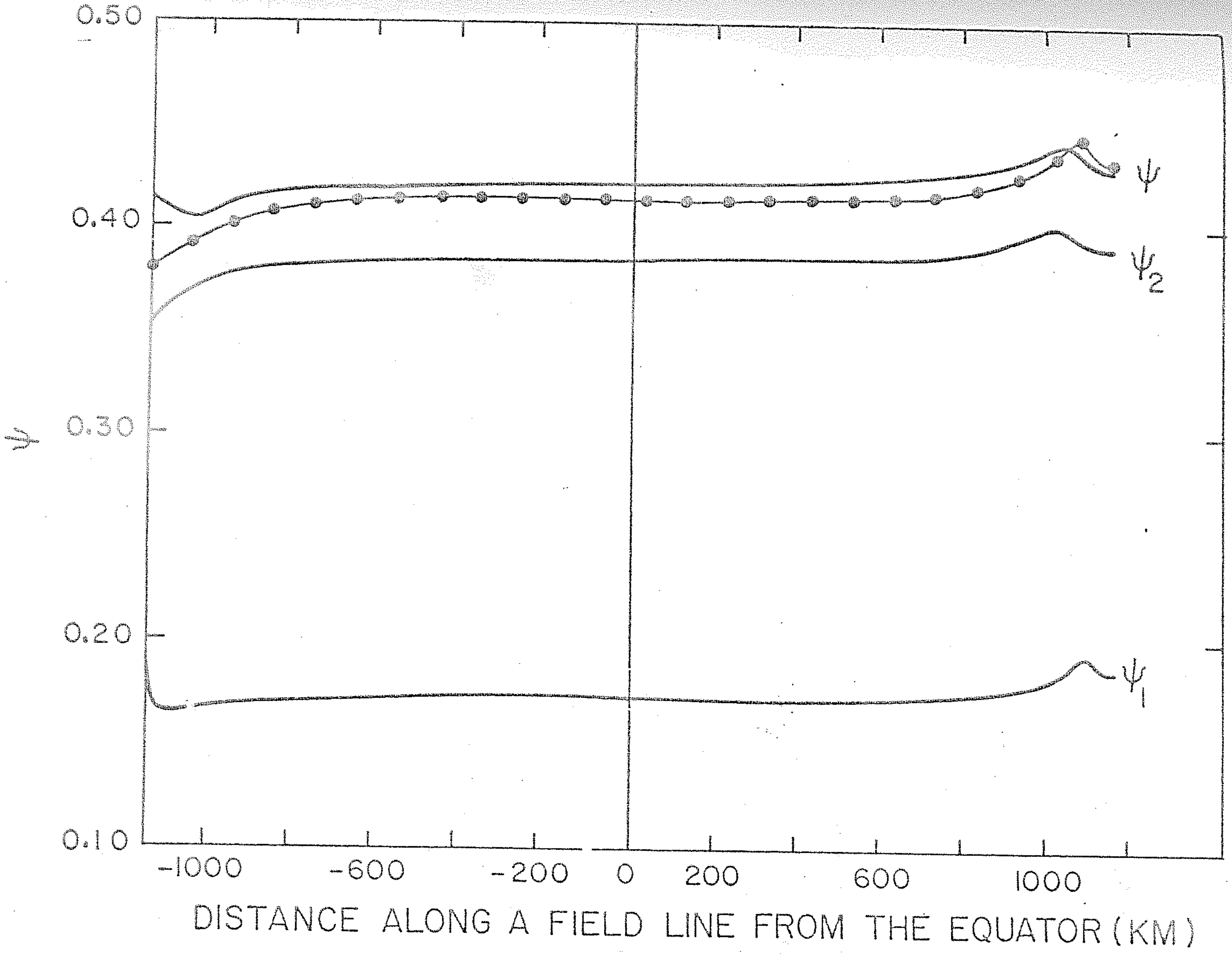

Fig. 3.10: Comparison of results obtained using the constant winds in region AA' (Fig. 2.3) with those obtained using the variational winds of Fig. 2.3. $\lambda_z' = 16$ km for both the cases. ψ is the representative of the total field.

We consider a daytime case for gravity wave winds with λ_z = 16 km. We assume that the condition $k_x=0$ is obtained at a distance of 940 km along a field line which has the apogee at 300 km. For λ_z = 16 km, the distance over which the winds are in the same direction around $k_x=0$ point is 320 km.

Results of these calculations are presented in fig.3.10 in which curves marked ψ_1 and ψ_2 correspond to the solution of eqn.(29) and (30) respectively. $|\psi|$ denotes the total field, as defined in eqn.(27) and is also plotted as solid curve.

Results of the case when constant winds are in the region from 780 km to 1100 km along the field line (centre at 940 km; $2d$ = 320 km) are also given in fig. 3.10 with dashed curve. This curve is also labelled as $|\psi|$.

A comparison of the curves marked $|\psi|$ shows that both the curves have near identical characteristics with nearly same value. Hence the constant winds around S, over the distance 2d as determined by λ_z, are as efficient in generating electric fields as are the sinusoidal winds of fig. 3.3. Hence in the following section, calculations are made with constant winds present in a limited region.

3.11 Calculations with Constant Winds in a Limited Region-Results and Discussion :

We now solve eqn.(32) for different values of λ_z, for various times of the day. A schematic of the calculations carried out is given in fig. 3.11.

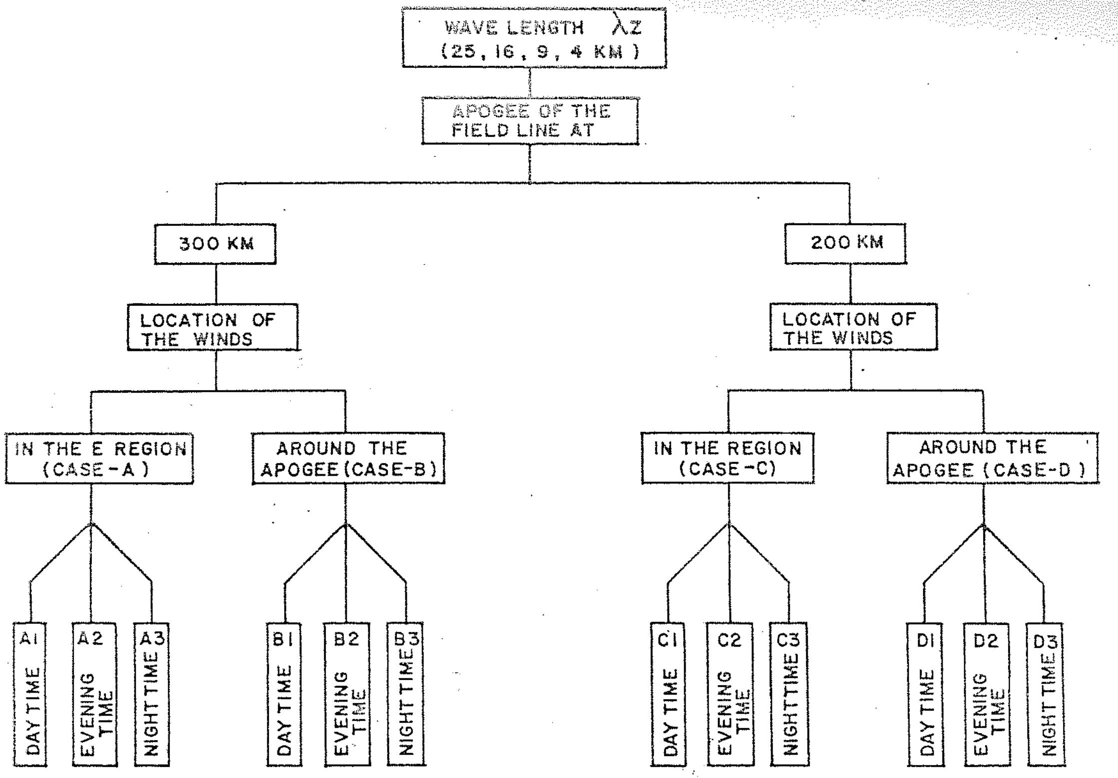

FIG. 3.11 SCHEMATIC OF CALCULATIONS

Calculations were carried out for four different values of λ_z ; 25 km, 16 km, 9 km and 4 km. For each value of λ_z , the cases with the field line apogee at 300 km and 200 km were considered. With a given apogee of the field line, two positionings of the wind regions, in the E region (Case A or Case C) and in the F region (case B or Case D), were considered. Each of these cases (Case A etc) was investigated for the daytime (A1, B1 etc), eveningtime (A2, B2 etc), and nighttime (A3, B3)etc) situations separately.

3.11.1 $\lambda_z = 25$ km:

The distance 2d, [illegible] the extent of the source region, can be calculated using eqn.(12) and is 400 km in this case.

3.11.1.1 Case A - Field line apogee at 300 km and winds in the E region:

The gravity wave winds of same velocity amplitude were assumed to be present, with centre at 940 km reckoned from the equator, extending from 740 km to 1140 km along the field line. The altitude range thus covered by the wind region is from 96 km to 214 km in one of the hemispheres. The solid curves of fig.3.12 give the results of these calculations, in which curves marked (1), (2) and (3) represent the daytime (A1) eveningtime (A2) and nighttime (A3) cases respectively. The electric field represented by parameter Ψ is plotted against the distance along the field line, reckoned from the equator.

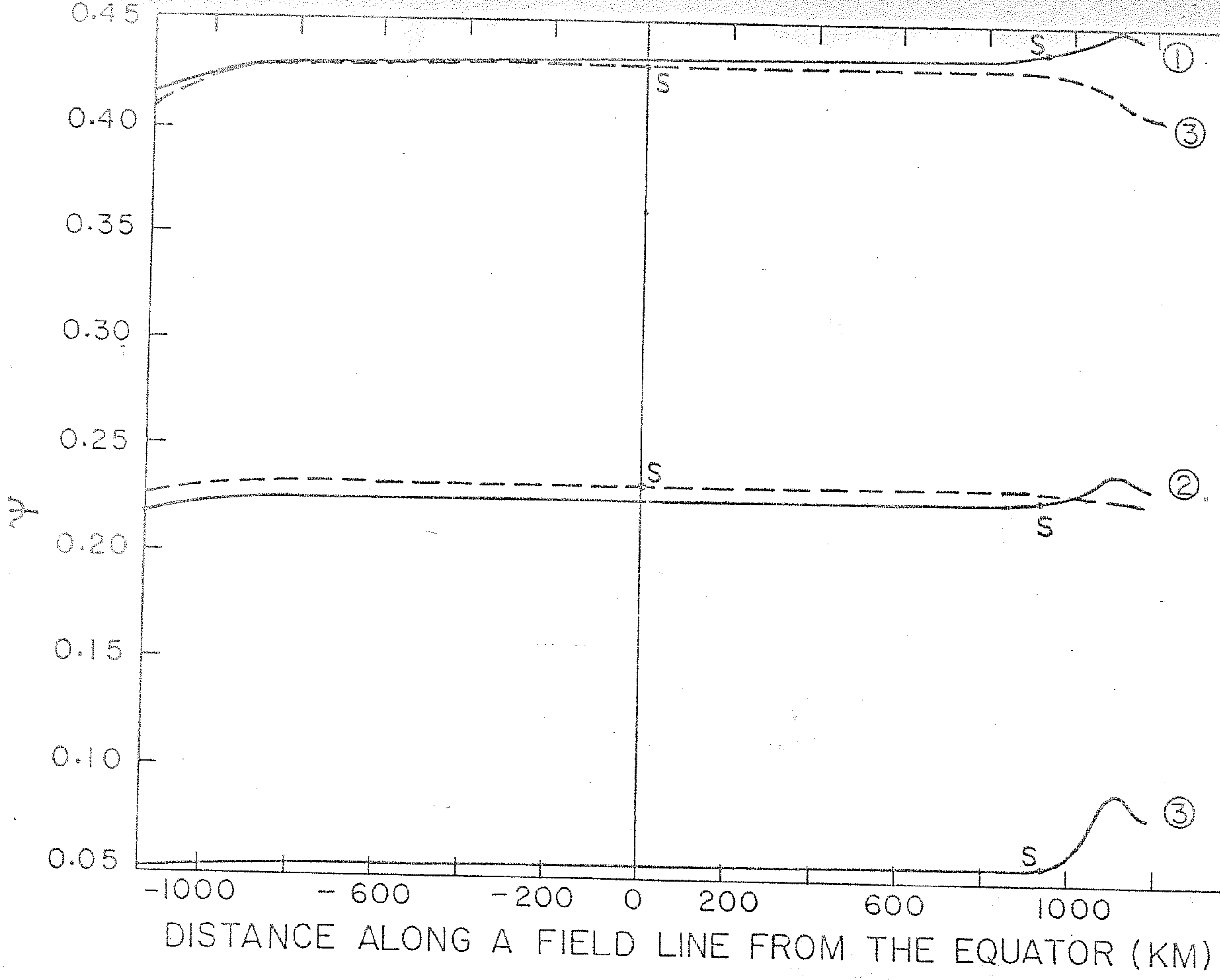
$\lambda z' = 25$ KM

Fig. 3.12: Variation of ψ with distance along B. The field line apogee is at 300 km in this case.

Generation of field in the source region:

It can be seen from fig. 3.12 that the maximum field in the source region is generated during the daytime and that the eveningtime field is larger than the nighttime field. This is because, for the daytime case, the wind region overlaps the region of maximum σ_p and outside the wind region, the conductivity σ_p is very small. For the eveningtime case, although the wind region overlaps one of the regions of maximum σ_p, its value outside the wind region is nearly same. For the nighttime case, the wind region does not overlap the region of maximum σ_p.

It can be seen from fig. 3.12 that in all the cases, the polarization field in the source region is never fully developed. The field is always less than 0.5 times the wind induced field ($\underline{W} \times \underline{B}$). For the daytime case, maximum field in the source region is about 0.45 times the ($\underline{W} \times \underline{B}$) field, while it is about 0.24 and 0.09 times the ($\underline{W} \times \underline{B}$) field for the evening and night time cases respectively.

Attenuation of the field:

Since the ionospheric regions are connected through the conducting geomagnetic field lines, the electric field generated in one region is likely to be transmitted to the other regions. It was shown earlier in section 3.8 that for large λ_z, the attenuation of the fields will be small. The results as given in fig.3.12 confirm this feature. For instance, in all the three cases, the attenuation of the field from the point S to the equator is less than 10%. That is, an appreciable fraction of the source field is transmitted to the equator.

3.11.1.2 Case-B. Field line apogee at 300 km and winds in the F region.

In this case the winds are assumed to be present in the F region, symmetrically with respect to the equator around the apogee of the field line. The extent of the wind region being ± 200 km around the equator, along the field line. The altitude range thus covered is about 6 km. Results of these calculations are presented in fig.3.12 with dashed curves (the curve for the case B1 is not plotted as its value was less than 0.05).

It can be seen from the dashed curves of fig.3.12 that while there is little difference between the results of two eveningtime cases (cases A2 and B2), the daytime (B1) and nighttime (B3) cases differ significantly from the corresponding cases of case A.

Results of the two eveningtime cases are similar because in both the cases the wind region overlaps one of the regions of maximum σ_p . This is owing to the shape of the σ_p profile for the eveningtime case (Fig.3.6). Also, the value of σ_p in the source region for the two cases in question, is almost equal. For the daytime case (B1), the wind region does not overlap the region of maximum σ_p . Thus the generated electric field is very small. For the nighttime case (B3), the winds are situated in the region of maximum σ_p . Also, due to very small Pedersen conductivity in the E region during the nighttime, most of the E region acts as an open circuit to the source field. Thus, the field is transmitted, as such, to the E region.

The attenuation of the field, for all the cases, is again less than 10%.

The results of the nighttime case (B3) bring out an important point. That is, in the nighttime, the dynamo (source of an electric field) is situated in the F region. The field generated in the F region is transmitted to the lower latitude E region in appreciable magnitude. This conclusion, on the location of the nighttime dynamo, is qualitatively similar to the one drawn by Rishbeth (1971) where he observed that the large scale east west winds in the equatorial F region during the nighttime are capable of generating electric fields in the F region. These fields can be transmitted to the E region in appreciable magnitude.

3.11.1.3 Case.C - Field line apogee at 200 km and winds in the E region:

In this case, the winds were assumed to be present in the region extending from 400 km to 800 km along $\underline{B}$, with their centre at 600 km. The altitude range thus covered by the wind region is from 100 km to 175 km. For this altitude range (by considering conductivity profiles upto 200 km altitude only), it can be seen from fig.3.6 that the region of maximum σ_P is covered in all the three cases. Hence,

$\lambda_Z' = 25$ kms

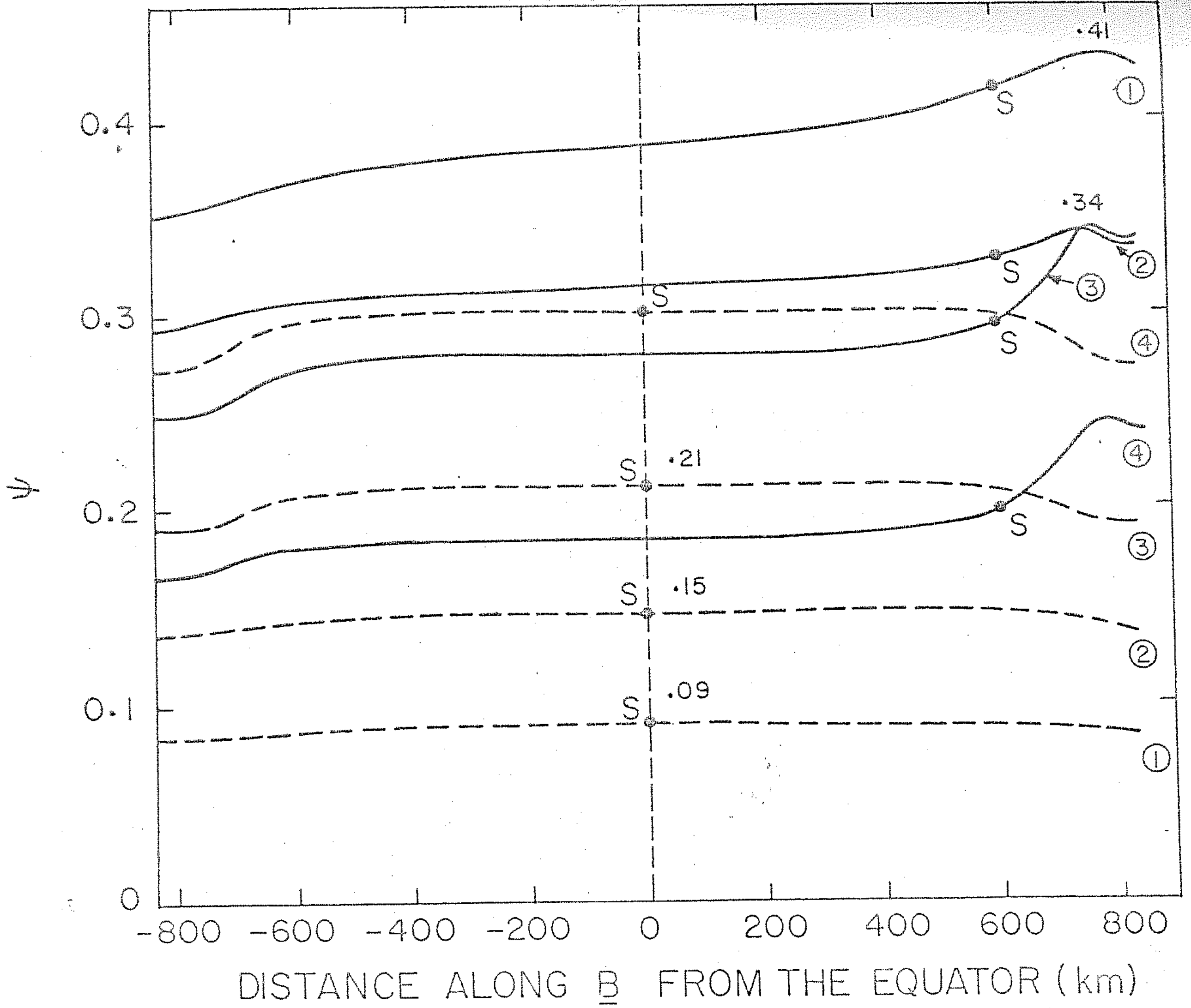

Fig.3.13: Variation of ψ with distance along B. The field line apogee is at 200 km.

large electric fields are expected to be generated in all the cases.

Solid curves of fig.3.13 give the results of the calculations for this case. Once again, the curves marked 1,2 and 3 represent the results of the daytime (C1), eveningtime (C2) and nighttime (C3) situations respectively. A curve marked 4 represents the results of the second nighttime case corresponding to the electron density profile (numbered 4) of fig. 3.5.

It can be seen from fig. 3.13 that the maximum field in the source region is developed during the daytime. Its value being 0.43 times the wind induced ($\underline{W} \times \underline{B}$) field. The field which is transmitted to the equator is about 0.39 times the ($\underline{W} \times \underline{B}$) field. It implies that about 85% of the source region field is transmitted to the equator.

Comparison of the eveningtime (C2) and nighttime (C3) results shows that, in general, the evening time field is more than the nighttime field. In the source region, the fields are generated in almost equal amount in both the cases. This is because of the particular shape of the σ_p profile for the nighttime case which has almost constant σ_p in the region where the winds are assumed to be present. The amount of the field which is transmitted to the equator is approximately 90% and 82% (of the maximum field in the source region) for the evening and night time cases respectively. The maximum field in the source region for both the cases (C2 and C3) is about 0.35 times the ($\underline{W} \times \underline{B}$) field.

The curve for the second nighttime case (C4) has the lowest value of Ψ in comparison to the other cases. This is in accordance with the electron density profile (fig. 3.5) for this case.

A comparison of the results obtained in the cases A and C reveals that the attenuation of the field is less in case A. For the daytime situation, the maximum field in the source region is almost equal in the cases A1 and C1. This is because in both the cases, the wind region covers the region of maximum σ_P, within which the integrated conductivity is essentially equal. Results of the evening and nighttime cases are, however, quite different in the two cases A and C. For Case A2, it can be seen from fig. 3.13 that the value of σ_P outside the wind region is comparable to that in the wind region. While in case C2, σ_P outside the wind region is quite small. Hence, the field in case C2 is larger than in case A2. In case A3, the value of σ_P outside the wind region is much larger than inside the wind region, while it is smaller in case C3. Hence the electric field in case A3 is much smaller than in case C3.

3.11.1.4 Case D - Field line apogee at 200 km and winds around the apogee of the field line:

The winds were assumed to be present in the region ± 200 km (along the field line) around the equator. The altitude range covered by the wind region is very narrow and

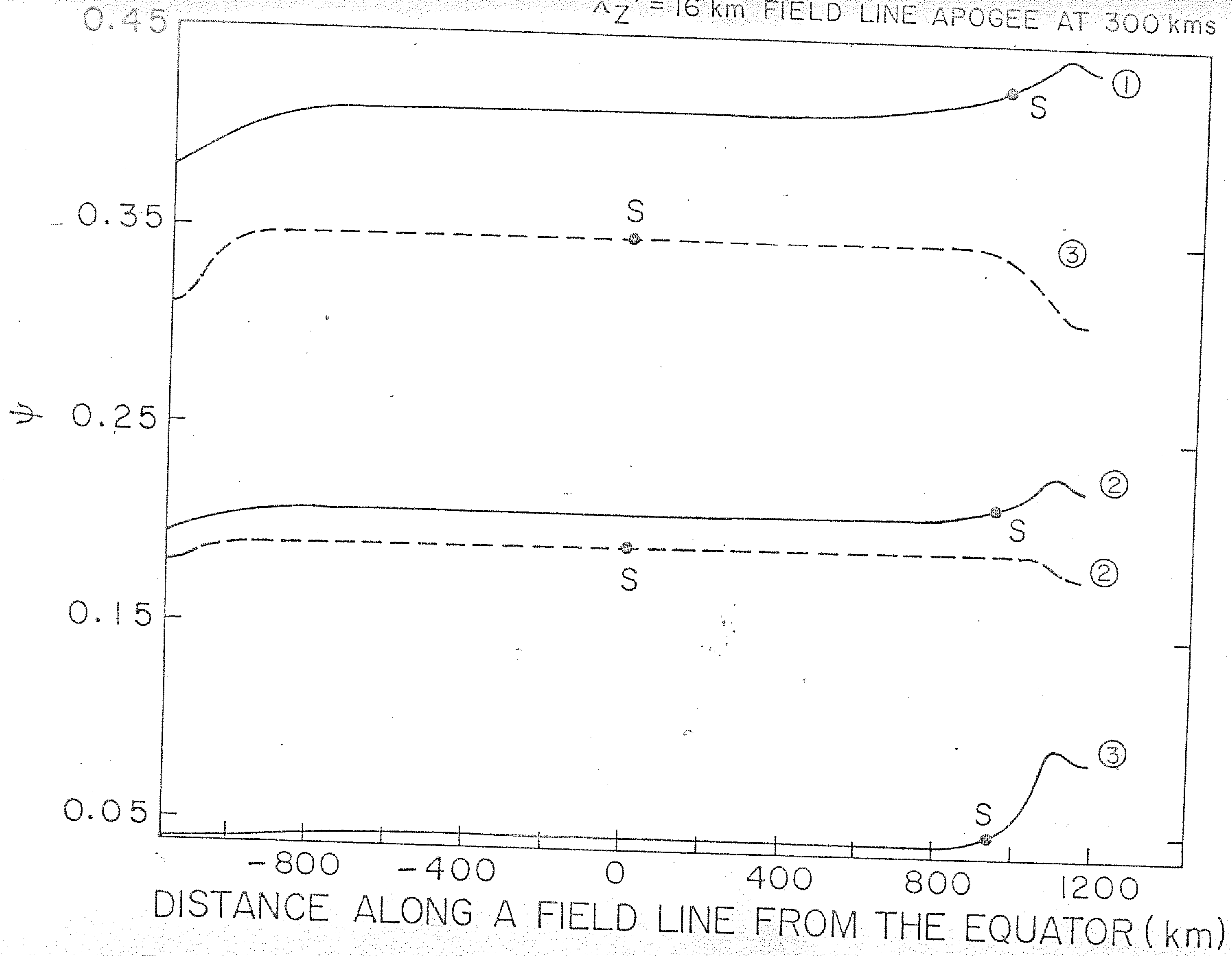

Fig. 3.14: Variation of ψ with distance along B.

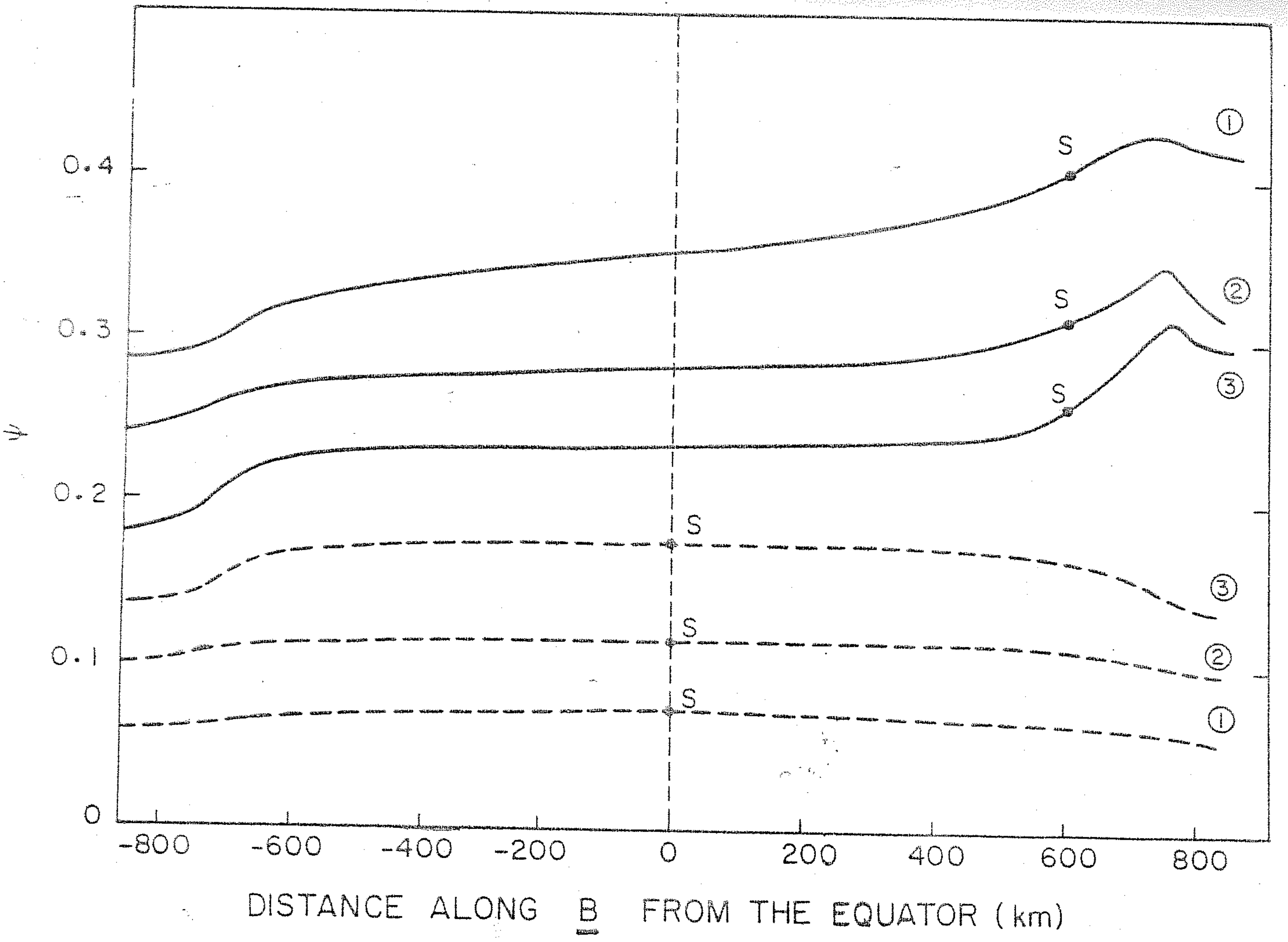

Fig. 3.15: Variation of ψ with distance along B. $\lambda_{z}' = 16$ km. The field line apogee is at 200 km.

for the practical purposes it can be assumed that the conductivities σ_0 and σ_p are constant in the wind region.

Results of the calculations for this case are presented in fig. 3.13 as the dashed curves. The general conclusions drawn from the results of case B are valid for this case also. It can be seen that the maximum field is generated in the nighttime and the least during the daytime. The field in the nighttime (D3) and eveningtime (D2) is about 0.21 and 0.15 times the wind induced field, ($\underline{W} \times \underline{B}$), respectively.

A comparison of results of cases B and D reveals that the generation of the field is more in case B. This is because of larger value of integrated σ_p in the wind region in case B as compared to that in case D.

The attenuation of the fields during the transmission is again quite small.

3.11.2 $\lambda_z = 16$ km

The extent of the source region in this case is 320 km along the geomagnetic field line.

Calculations carried out under the conditions similar to those for $\lambda_z = 25$ km case were repeated. The results of the calculations are presented in figs. 3.14 and 3.15. It can be seen from these diagrams that the results of this case are qualitatively similar to those obtained in section 3.11.1 for $\lambda_z = 25$ case.

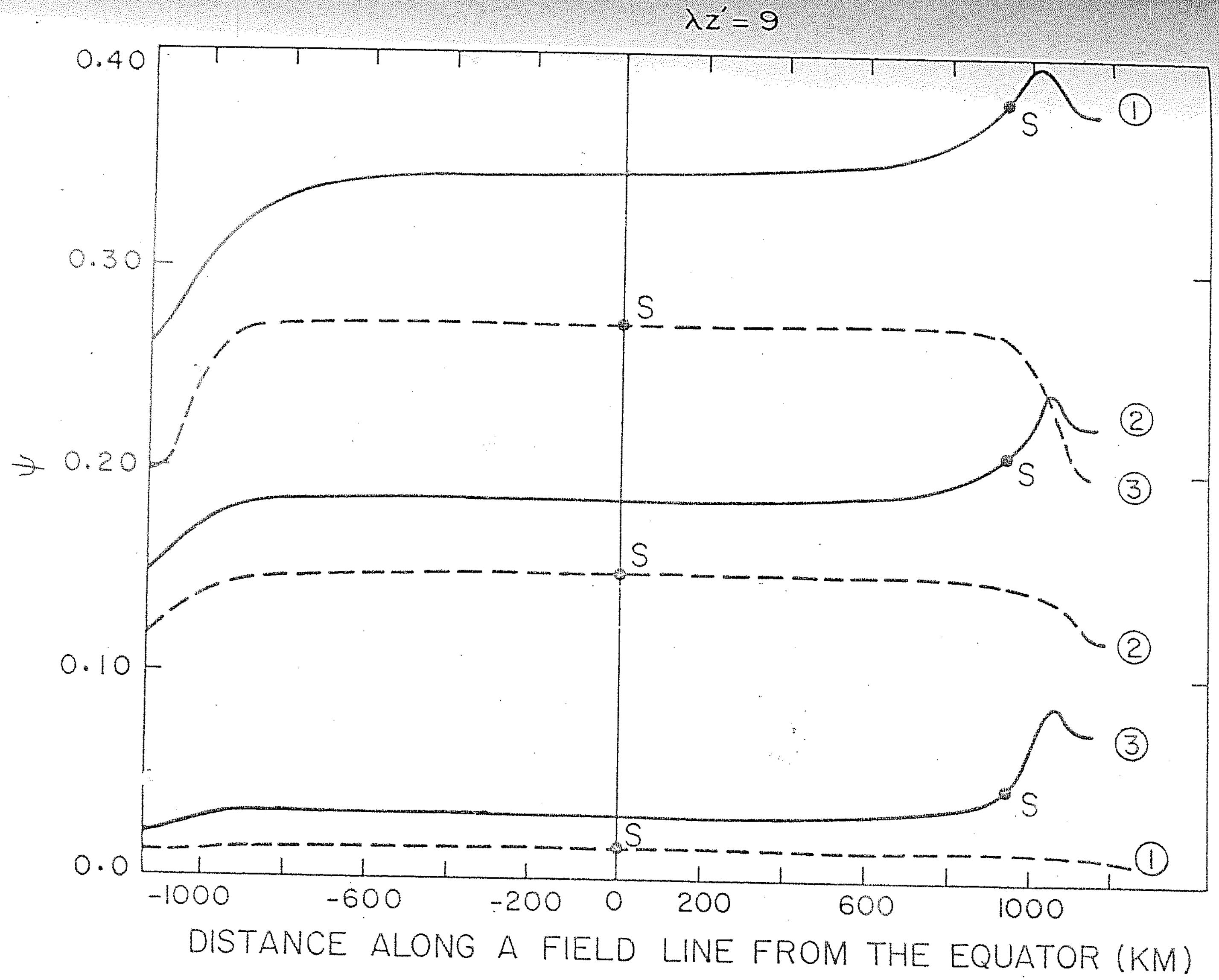

Fig. 3.16: Variation of ψ with distance along B. The field line apogee is at 300 km.

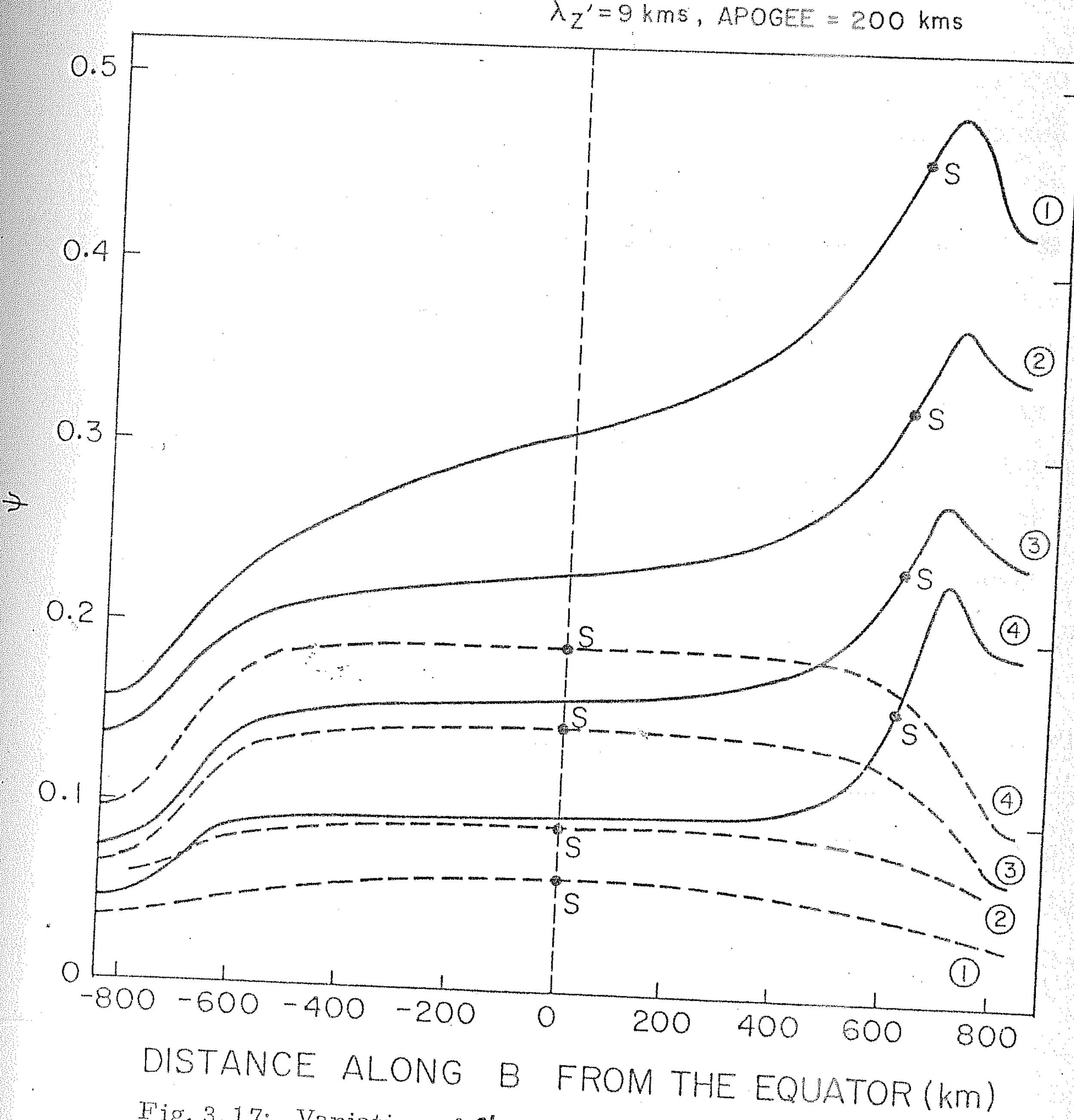

Fig. 3.17: Variation of ψ with distance along B.

Since the results of this section are not different from those of section 3.11.1, no further discussion of the results is necessary.

3.11.3 $\lambda_z = 9$ km

In this case the extent of the wind region is 240 km along $\underline{B}$ and the wind region was so situated that it does not, necessarily, overlap the region of maximum σ_p in all the cases. For example, in case A, the wind region was from 820 km to 1060 km (along $\underline{B}$) which corresponds to an altitude of range of about 125 km to 195 km in one of the hemispheres. Similarly, in case C, in which the field line apogee is at 200 km altitude, the wind region was from about 130 km to 175 km altitude.

Results of this case are presented in figs. 3.16 and 3.17 which correspond to the case with the field line apogee at 300 km and 200 km respectively. It can be seen from these figures that in this case, the attenuation of the field during transmission is larger than in the cases considered earlier in sections 3.11.1 and 3.11.2. In this case, the attenuation of the field in case C is more than in case A, and in case D is more than in case B. A good fraction of the ($\underline{W} \times \underline{B}$) field is, however, generated in the source region in cases A1, A2 and B3 and is transmitted to the other regions also.

3.11.4 $\lambda_z = 4$ km

This is the last of the cases considered for these studies. For $\lambda_z = 4$ km, wind region is 160 km along a given field line. Again, the winds were assumed to be centred around the apogee of the field line in cases B and D, and at a distance of 940 km (Case A) and 600 km (case C) from the equator along B. In cases A and C, the wind region does not overlap the region of maximum σ_p .

Results of this case are presented in figs. 3.18 (for cases A and B) and 3.19 (cases C and D). It can be seen from these figures that for all the cases, the attenuation of the field is larger in the E region.

During transmission of the source region field to the equator, the field suffers an attenuation of about 25% in case A, while the attenuation is more than 50% in case C. These results, on the attenuation of the field, are in confirmity to the conclusions drawn in section 3.8 for small value of λ_z. Although the generation of the field in the source region, in this case, is more than in the cases considered earlier in section 3.11.1 through 3.11.3, these fields suffer strong attenuations and become very small within a short distance. Hence for small λ_z , appreciable amount of the electric field can not be transmitted to the other regions.

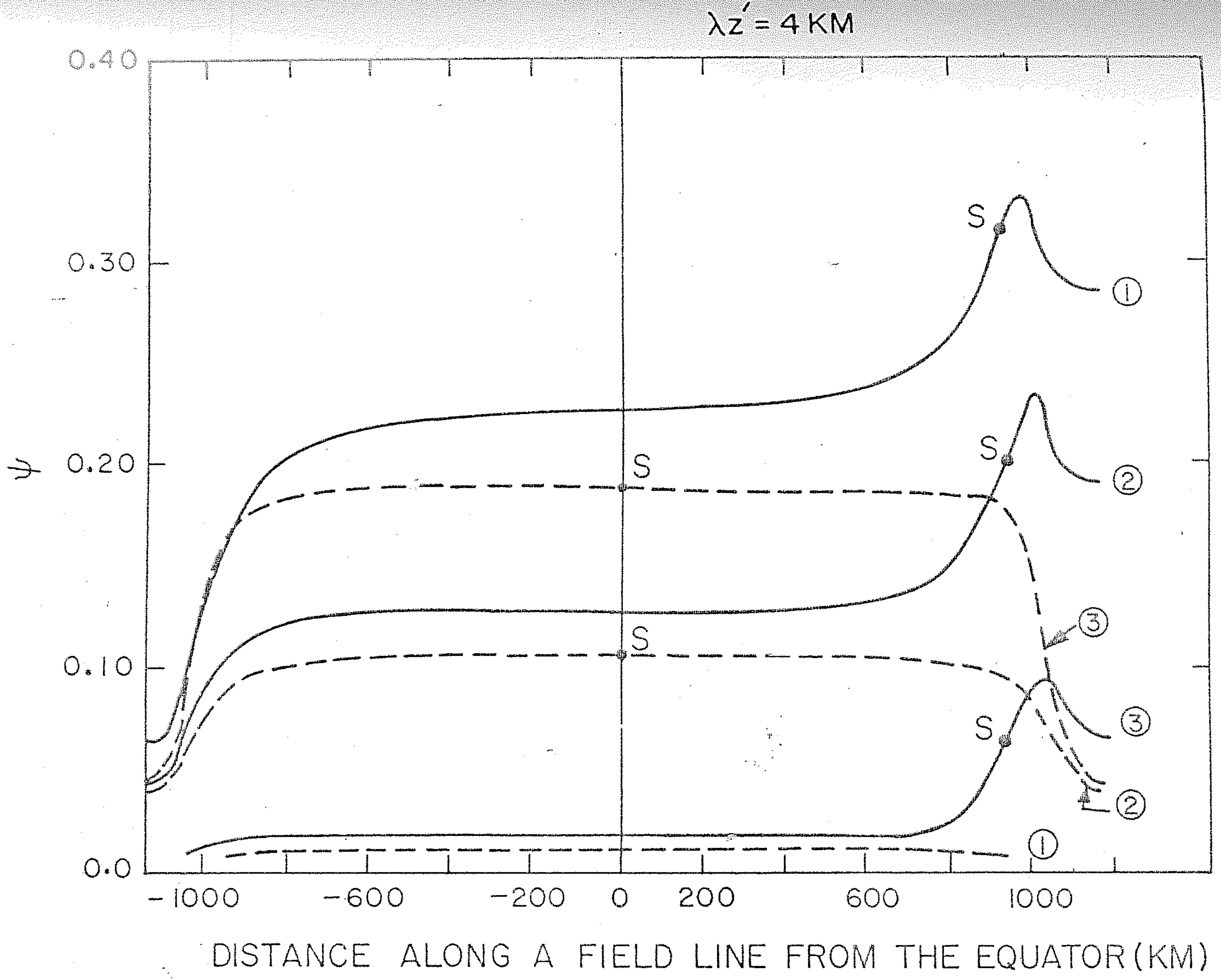

Fig.3.18: Variation of ψ with distance along B. Apogee of the field line is at 300 km.

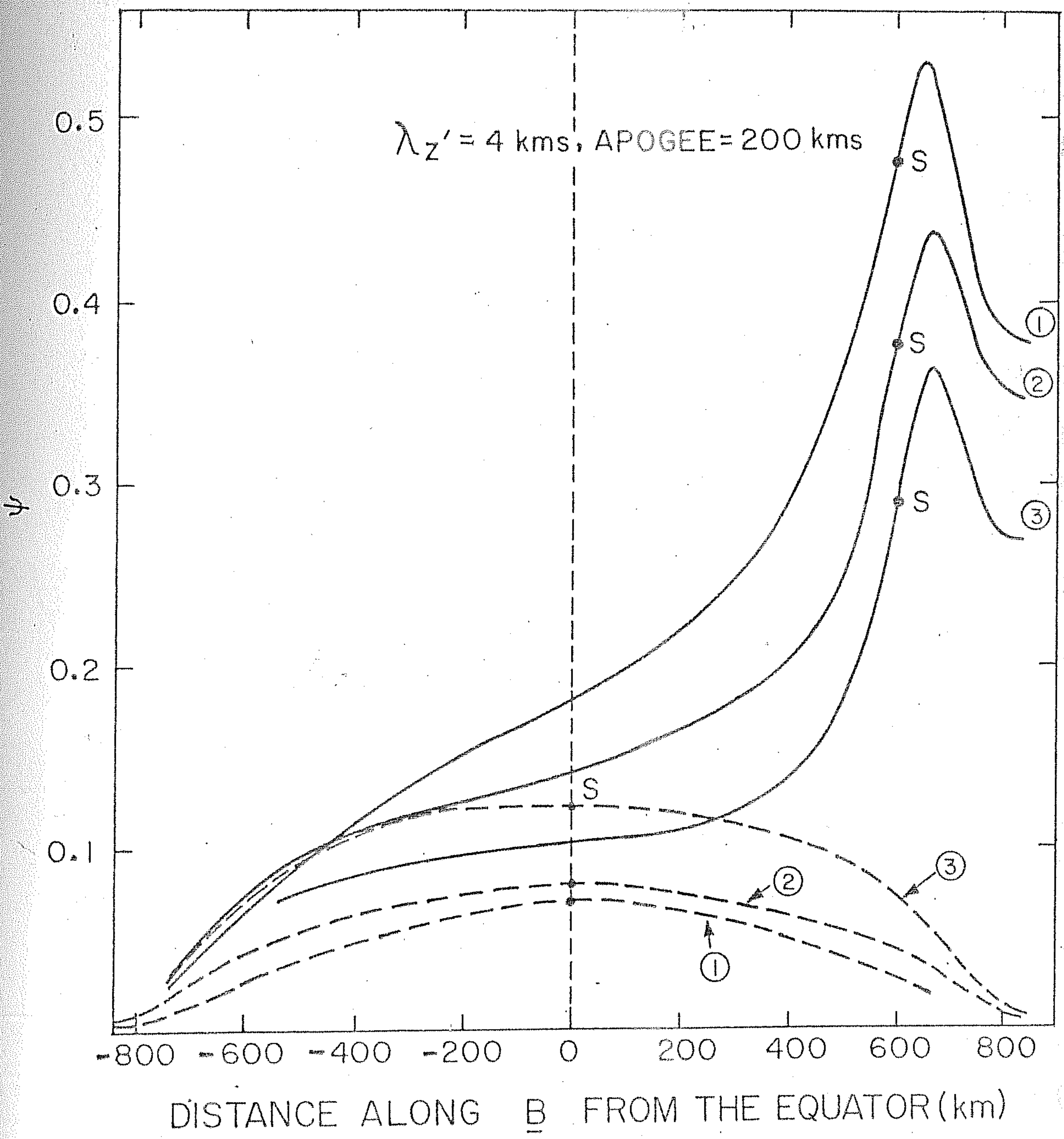

Fig. 3.19: Variation of ψ with distance along B.

3.12 Summary:

The generation of electric fields due to the three dimensional gravity wave winds and their transmission to the other regions of the ionosphere was investigated in this chapter. The gravity wave winds in different regions of the ionosphere with different vertical wavelengths were used to calculate the electric fields at different times of the day. The following are the salient features of this study.

(i) While k_z varies slowly with the dip angle, k_x varies rapidly and undergoes a change of sign (fig. 3.2).

(ii) On a given geomagnetic field line, the wind pattern around the point where $k_x = 0$ is symmetrical (figs. 3.3 and 3.4). This point has been referred to as point S. Around the point S, the winds remain in the same direction over a large distance ($2d = \sqrt{\lambda_z R}$). For example, for λ_z = 16 km, this distance is 320 km. Away from the point S, the wind varies sinusoidally with wavelength decreasing with increasing distance.

(iii) The electric fields are mainly generated due to the winds around S and hence this region has been referred to as the source region. The electric fields due to the sinusoidal winds get shorted, approximately, within a wavelength.

(iv) The geomagnetic field lines act as conductors carrying current. The rest of the region connected by these field lines to the source region acts as load.

(v) In the load region, the attenuation of the electric field increases with the decrease of λ_z. For example, for λ_z = 25 km (fig. 3.12, case A1), the attenuation of the field from the point S to the equator is less than 10%. Similarly for λ_z = 16, 9 and 4 km (Case A1 in figs. 3,14, 3.16 and 3.18 respectively) the attenuation of the field is less than 10%, about 15% and 25% respectively.

For a given λ_z, attenuation length of the field in the E and F regions can be calculated using the expressions as given in section 3.8. For λ_z = 25 km, the attenuation length in the E and F regions is of the order of 10^4 and 10^5km respectively. These values are in close agreement with the one obtained from fig. 3.12 (Case A1).

(vi) The generation of the electric field is most efficient when the source region overlaps the region of maximum σ_p. For example, for the daytime case when σ_p is maximum in the E region, the field is maximum when the source region is around 140 km. Similarly for the nighttime case when σ_p is maximum in the F region, the field is maximum when the source is in the F region (fig. 3.14, λ_z = 16 km case).

The electric field in the source region is always less than the ($\underline{W}$ x $\underline{B}$) field. However, it is a substantial fraction of (W x $\underline{B}$) field. For example, for λ_z = 25 km, 16 km, 9 km and 4 km; the field in the source region is 0.45, 0.43, 0.41, 0.33 times ($\underline{W}$ x $\underline{B}$) field, respectively.

CHAPTER IV

GENERATION OF EQUATORIAL SPREAD F IRREGULARITIES DUE TO THE GRAVITY WAVE INDUCED ELECTRIC FIELDS

4.1 Introduction:

This chapter is devoted to the electron density irregularities in the equatorial F region. The sectionwise breakup of the studies carried out in this chapter is as follows.

In section 4.2, the VHF radar studies on the equatorial spread F are summarised.

Section 4.3 gives the important results of in-situ studies on the equatorial F region.

In section 4.4, the generation mechanisms of the spread F irregularities are discussed which rely on either the plasma instability mechanisms or the neutral wind induced processes.

Short comings of these mechanisms are discussed briefly, in section 4.5.

In section 4.6, a new mechanism for the generation of spread F irregularities is proposed which is based on the studies carried out in chapter III.

In section 4.6.2 a detailed discussion on the aforesaid mechanism is given.

Section 4.7 gives the conclusions of the studies carried out in this chapter.

Appearance of diffused echoes on ionograms has traditionally been termed spread F. The spreading of F region ionogram traces was first observed by Berkner and Wells (1934). This spreading of F region traces was ascribed to the presence of large scale irregularities.

Historically, attempts to explain the equatorial spread F phenomena began with linear theories. Dungey (1956) was the first to propose that the equatorial spread F phenomena was due to Rayleigh - Taylor plasma instability, initiated on the bottom side of the F region. Dagg (1957) suggested that these irregularities were first produced in the E region and transmitted to the F region through highly conducting lines of geomagnetic flux. Martyn (1959) proposed that these irregularities were due to the $\underline{E} \times \underline{B}$ drift instability. A similar proposition, in its effect, was made by Calvert (1963).

Although the subject of equatorial spread F is more than forty years old now, untile recently only statistical data was available on it (Shimazaki, 1960; Singleton 1960, 1962; Briggs 1964; Herman 1966; Clemesha and Wright 1966; Dyson 1967; Singleton 1968). Chandra and Rastogi (1972) have classified the equatorial spread F into range and frequency type.

4.2 Recent V.H.F Radar Studies:

Spread F studies received a new impetus after Farley et al (1970) published the first comprehensive results on spread F using the coherent backscatter radar observations made at

Jicamarca, Peru. The Jicamarca radar operates at 50 MHz which corresponds to 3 m irregularity scale size. The highlights of their results were the presence of 3 m scale size irregularities below, at and above the F region peak when the F region was moving upward, downward or not at all. On the basis of these observations, Farley et al (1970) conclded that no existing theories could explain all the features of spread F irregularities.

Woodman and LaHoz (1976) using more refined 3 m backscatter radar observations at Jicamarca showed that spread F could occur at the topside, at the steep bottom side of the F region and in the valley between E and F region with no preferred direction of the large scale electric field. It was found that typically after sunset, a narrow band of returned echoes came from the region below the F peak, and sometimes within an hour time, irregularities were observed above the F peak. These structures were found to move west ward. They, sometimes, extended hundreds of km in altitude, connecting the top and the bottom side of the ionosphere. Woodman and LaHoz (1976) inferred that a Rayleigh-Taylor mechanism was at work in which bubbles or low density regions of plasma rose from the bottom side of the F region.

Altair backscatter radar observations made at Kwajalein have shown the presence of irregularities with scale sizes $\lesssim 1$ m. These irregularities were found to be associated with the regions of depleted electron density.

4.3 In-situ studies

In situ measurements of spread F irregularities have also been made to measure the electron density, fluctuations in density, chemical composition and the wide range of scale sizes associated with spread F. Mclure et al (1977) using the AE-C satellite data have observed large scale (10 to > 200 kms) depletions in the ion density of upto three orders of magnitude. Using the ISIS-I data, Dyson and Benson (1978) have found that the bubbles extended long distances along the geomagnetic field lines. Rocket measurements by Kelly et al (1976) at Natal, Brazil detected fluctuations in electron density upto a factor of two in the bottom side F region. Recent electron density measurements near the dip equator at Shri Harikota Range (SHAR), India (Prakash et al, 1981) showed the presence of large electron density depletions (Fig 4.1). The rocket was launched at 2103 hrs (LT) during a strong spread F as observed with the ground based ionosonde. The rocket reached an apogee of 350 kms. This was the first rocket launch in the Indian zone during spread F condition. A highly variable and structural electron density profile was obtained. Salient features of the electron density profile during the rocket ascent are as follows.

(i) The bottom side F layer was around 250 km in which the electron density varied by over an order of magnitude within 3-4 km.

(ii) A large valley region extending from about 140 km to

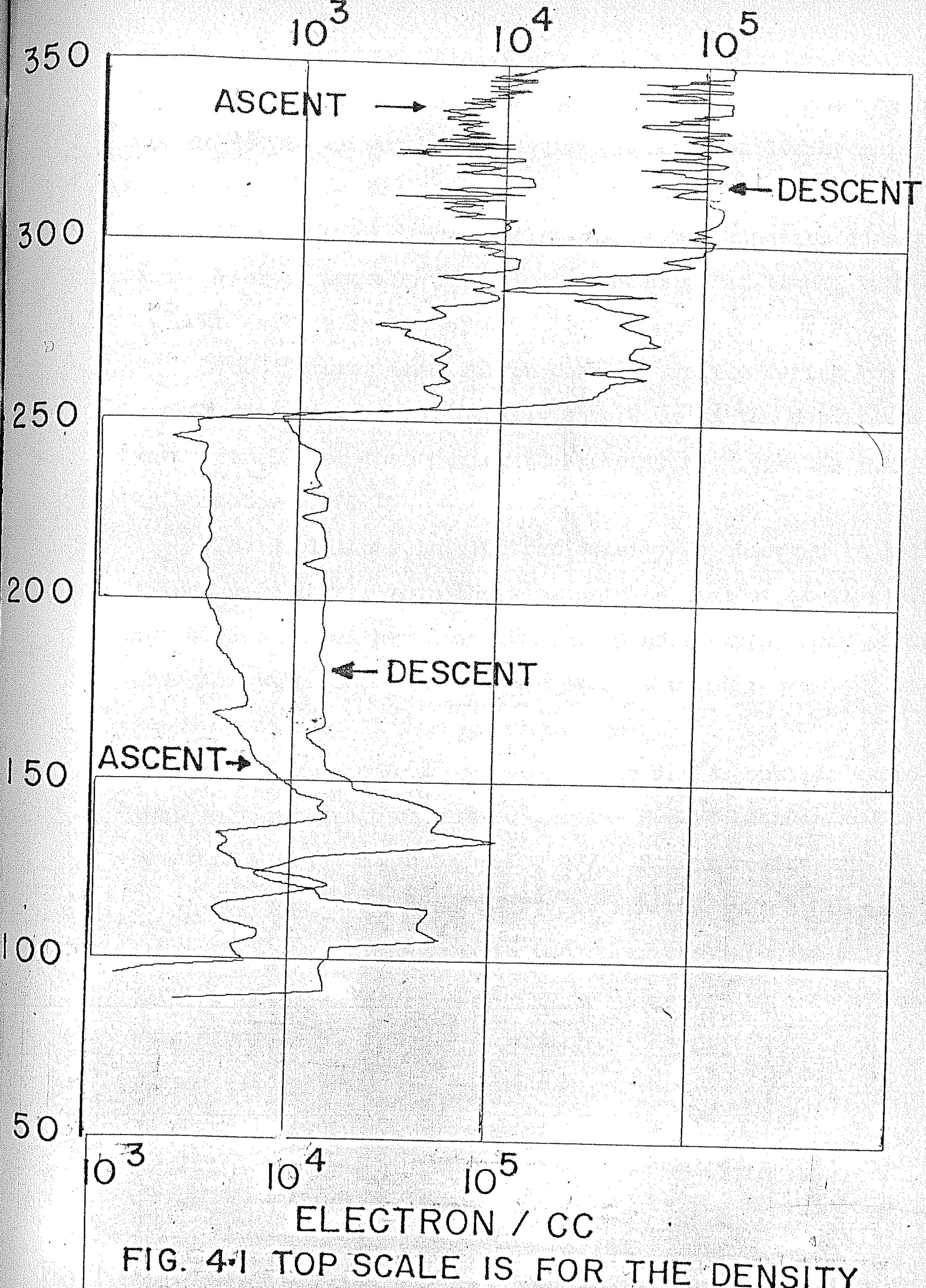

FIG. 4·1 TOP SCALE IS FOR THE DENSITY DURING THE ROCKET DESCENT

250 km with electron density around 5 x 10^3 electron/cc.

(iii) Large structures in the electron density in the region 100 to 150 km in which the electron density varied by more than a factor of 2 to 3.

(iv) Above 250 km, large depletions in the electron density were observed wherein the electron density, at times, varied as much as by a factor of 4.

The factures in electron density profile during the rocket descent were essentially same. Some of the depletions were even larger than during the ascent, with density varying by a factor of 8.

The depletions in electron density as observed in this flight were larger than those reported by Kelley et al (1976). But AE Satellites have observed the density depletions of three orders of magnitude. This discrepancy between rocket and satellite measurements, still remains unresolved.

Ion composition measurements inside the bubbles indicate that they originate at altitude below F peak (Hanson and Sanatani 1971 , Mclure et al 1977 , Szuszezcevicz 1978) .

Based on the ground based and insitu studies, it is found that the plasma density irregularities with scale sizes ranging from hundreds of km down to a few cm are associated with spread F phenomena. A number of theories have been proposed to explain the generation of this wide scale size range of irregularity spectrum.

4.4 Theoretical studies

The theories which have been proposed rely either on the plasma instability or neutral wind induced processes.

4.4.1 Plasma Instability mechanism

With the observations of Woodman and LaHoz (1976) interest in the Rayleigh-Taylor instability as a causative mechanism for the spread F irregularities was revived. Scannapieco and Ossakow (1976) performed a nonlinear computer simulation of the collisional Rayleigh Taylor instability for the equatorial spread F geometry. In this, a few percent perturbation on the bottom side developed due to collisional Rayleigh Taylor instability and generated bubbles there. These bubbles then rose up due to non linear polarization induced E x B motion. Extension of this work (Ossakow et al, 1979) showed that a high altitude of the F layer peak and or steep bottom side gradient facilitated faster growth rate and large rise velocity of these bubbles. This way they could show the production of irregularities on the bottomside as well as on the top side where a linear instability would not predict any irregularities. Thus when the peak of the F region was lifted from 350 to 430 km, the bubble rise velocity was found to be about 160 m/sec which was an order of magnitude larger than that obtained earlier by Scannapieco and Ossakow (1976). With these computer simulations, Ossakow et al (1979) could produce bubbles of spatial size of the order of a km in the east-west direction. Although the meter scale size irregularities could not be produced through this mechanism, they expected that the steepening bubbles; rising through the F-peak will bifurcate and produce shorter and shorter wavelength irregularities either by a cascade or by a two step mechanism.

4.4.2 Neutral winds induced processes

Chiu and Strauss (1979) have examined the Rayleigh - Taylor instability in the equatorial ionosphere using the effects due to an east-west neutral wind and nighttime polarization fields as suggested by Rishbeth (1971). They argue that the basic criterion of Rayleigh-Taylor instability is satisfied by nighttime bottom side conditions of the equatorial F layer virtually all the time, yet the occurrence of spread F is extremely variable not only on the time scale of days **but** also shows strong seasonal-longitudinal effects. They found that an east ward neutral wind, rather than the gravitational drift, in the bottom side F region can drive Rayleigh - Taylor instability. They further argue that since the dominant neutral wind in this region is solar semi diurnal tide whose amplitude varies with season, solar cycle and local orographic conditions, the spread F occurrence also shows these dependences. Thus they suggest that the ionospheric bubbles originate considerably below the bottom side F layer, and appear as deep density bite outs when they propagate into the F region.

They find that the nighttime polarization field which drives an eastward ionospheric drift, is primarily stabilizing. Since $\underline{E} \times \underline{B}$ drift is of same order of magnitude, the effect of the eastward $\underline{E} \times \underline{B}$ drift is to stabilize the wind driven instability throughout most of the night. This implies that the instability is most likely to occur when the ionospheric drift changes from the daytime westward pattern to the nighttime eastward pattern.

Rottger (1976), Kloster meyer (1978) and Booker (1979) have suggested that gravity wave travelling ionospheric disturbances (TID), i.e., a neutral atmospheric phenomena, are a cause of equatorial spread F. The hundreds of km irregularity patches and patch separation observed in the east-west direction during the equatorial spread F may be suggestive of a long wavelength gravity wave arrangement of the plasma (Rottger, 1976). Kloster meyer has done detailed calculations using the spatial resonance mechanism (Whitehead 1971). The ionosphere must be travelling downward to come into spatial resonance with the gravity waves. However, equatorial spread F is often observed to begin when the ionosphere is moving upward and so this mechanism can not account for those observations. Klostermeyer's non linear calculations show that downward and eastward moving plasma density depletions could be produced by the gravity waves. The results could not explain the upward and westward bubbles, but Klostermeyer has suggested that this TID effect could provide the seed for spatially large bubbles which are then lifted by the nonlinear collisional R-T mechanism (Scannapieco and Ossakow, 1976).

Booker (1979) argues that under evening conditions in the equatorial regions, there is a band of TID frequencies for which the phase trace speed in the direction of plasma drift can be approximately equal to the drift speed. When this happens, the band of TIDs is amplified. This band of TID is then pulled out of the noise and is amplified until it breaks. When it breaks, many types of plasma instabilities, including the Rayleigh-Taylor, are excited.

4.5 Shortcomings in the earlier mechanisms

From the foregoing discussion it is clear that there are two schools of thoughts to account for the spread F phenomena. While one of these entirely relies on the plasma instability mechanism, the Rayleigh - Taylor instability, the other ascribes it entirely to the neutral atmospheric dynamics, winds, the acoustic gravity waves. There exists a persuasive evidence to justify both the approaches. It seems unlikely that either of these two approaches can explain all the observations. The plasma instability processes alone become a weak case due to

(1) spread F occurrence statistics

(2) requirement of large initial amplitude perturbations in electron density.

Observations have shown that although the basic criterion for the excitation of Rayleigh - Taylor instability is satisfied almost on all the nights, spread F is not observed on all the nights. Also, if the Rayleigh - Taylor instability is to grow from the thermal fluctuation level, it will require several e-folding growth time to grow to an appreciable and detectable amplitude; whereas spread F is observed soon after the sun set.

At this stage it is worthwhile to comment on the initial perturbation magnitude of the irregularities as used by Ossakow et al (1979). They have used initial perturbation, in the electron density, to be ± 5% for irregularities of scale sizes $\leqslant$ 1.6 km in the east-west direction, and ± 2.5% for irregularities of scale sizes greater than 1.6 km but less than 3.2 km. These perturbations, after some 30 minutes, grew to give a maximum depletion (enhancement) of 27% (23%). There is however, no justification to assume such large initial perturbation magnitudes for the instability which should grow from the thermal fluctuation level. Evidently, such large initial perturbations on which the Rayleigh - Taylor instability grows, requires some other mechanism to produce them. We will return to this point later.

Spatial resonance theory (Klostermeyer, 1978, Booker 1979) also suffers from a predetermined direction of the zero order electrostatic field for the gravity wave phase velocity to come into a spatial resonance with the drifting plasma whereas the observations of Farley et al (1970) show that spread F occurrence does not relate to any preferred direction of the electrostatic field.

To account for the topside spread F the bubble theory has been put forward. In which regions of low density plasma rise due to nonlinear polarization induced $\underline{E} \times \underline{B}$ drift. Since the F region plasma is incompressible, transport of the plasma from other regions has to take place to account for the large structures in the plasma density. The bubbles thus have to be generated in the bottom side. But the question which remains to be answered is as what initiates the bubble formation, whether the Rayleigh Taylor instability or the gravity waves? Anderson and Haerendel (1979) have calculated the polarization electric field, inside a bubble using the flux tube integrated electron density and conductivity. The bubble, as defined by them, is a region of depleted plasma density along the flux tube. This definition of bubble stems from the Aloutte 2 and ISIS-I Satellite measurements of Dyson and Benson (1978). The expression for the polarization field inside a bubble is given by

$$\underline{E}_1 = \frac{\Sigma_0}{\Sigma_1}\,\underline{E}_0 + \frac{e g_0 L}{\Omega_0 \Sigma_1}\left(N_0 - N_1\right) \qquad (1)$$

where $\Sigma_0(\Sigma_1)$, $N_0(N_1)$ are the flux tube integrated Pedersen conductivity and electron density outside (inside) the bubble, L the background density gradient length, g_c is the gravitational acc^n and Ω_0 is ion neutral collision frequency. This expression emphasises the importance of background electric field $\underline{E}_0$ (which was taken to be due east) and the density gradient length scale for the acceleration of a bubble. An eastward background electric field (when $N_1 < No$) facilities faster rise velocity of a bubble. In the initial stages, $\underline{E}o$ is very important for large rise velocity of the bubble. When $\underline{E}_1$ exceeds a limiting value, direction of $\underline{E}$ is no longer of great significance and even if $\underline{E}$ reverses, the bubble may continue to rise.

Thus it is clear that both the background field and the density gradient scale length play an important role.

4.6 Spread F irregularities due to the gravity waves induced fields:

In the previous chapter we have shown how the fluctuating electric fields can be generated due to the gravity wave winds during different periods of the day and what fraction of these fields can be transmitted to different regions of the ionosphere. In what follows, we examine the role of gravity wave induced electric fields in the production of spread F irregularities through plasma transport.

It was found that the gravity wave induced electric fields (GWEF) are generated most efficiently if the region where $R_x \sim 0$ overlaps the region of maximum Pedersen conductivity. Depending upon the conductivity profile, it was found that the gravity waves can produce electric fields not only in the E region but in the F region also. Since the GWEF have practically no variation along the field line and hence can be represented as

$$E_{y,z} = E_{oy,oz} \exp\{i(k_y y + k_z z - \Omega t)\} \qquad (2)$$

where k_y and k_z are components of the gravity wave vector in the y and z directions and $E_{oy,oz}$ are the peak amplitudes of the electric fields in the respective directions, Ω is the wave frequency. Eqn.(2) shows that the GWEF do not have any component along the magnetic field.

The coordinate system is such that the x axis is along B, y axis towards magnetic west and z axis is upward and perpendicular to both x and y axes.

4.6.1 Theory

The ion velocity in presence of an electric field E and wind $\underline{W}$, is given by (Macleod, 1966)

$$\underline{V}_i = \frac{1}{B(1+R_i^2)}\left\{R_i \underline{E}^W + \frac{1}{B}(\underline{E}^W \times \underline{B}) + \frac{1}{B^2 R_i}(\underline{E}^W \cdot \underline{B})\underline{B}\right\} + \underline{W} \qquad (3)$$

$$\underline{E}^W = \underline{E} + \underline{W} \times \underline{B} \qquad (4)$$

and $\underline{E}$ is the polarization field. Rest of the terms have their usual meanings.

In eqn.(3), background d.c. electric field has not been included. However, its effect can be taken into account at will.

Using eqn.(2) and also that $R_i \ll 1$ above 150 km altitude, eqn.(3) reduces to

$$\underline{V}_i = \frac{1}{B^2}(\underline{E} \times \underline{B}) + \hat{i} W_x \qquad (5)$$

Eqn.(5) contains both the GWEF and local gravity wave wind terms. We first discuss the irregularity production due to the GWEF alone, neglecting the wind term for the time being.

Calculating the divergence of ion flux in rest frame we get,

$$\nabla\cdot(N\underline{V}_i) = \frac{N}{B^2}\nabla\cdot(\underline{E}\times\underline{B}) + \frac{E_z}{B}\frac{\partial N}{\partial y} - \frac{E_y}{B}\frac{\partial N}{\partial z} \qquad (6)$$

since the electric field is electrostatic, the first term on the r.h.s of eqn.(6) is equal to zero. Thus it is clear that the electric field by itself does not produce the ionization irregularities but requires an electron density gradient.

At this stage it is quite illustrative to understand the nature of F region plasma using the ion continuity equation which is

$$\frac{\partial N}{\partial t} + \nabla\cdot(N\underline{V}_i) = q - L \qquad (7)$$

where the terms have their usual meanings. In the nighttime, the production and loss terms in the F region ionosphere can be ignored, and transforming the equation in the frame which moves with the plasma we get,

$$\frac{dN}{dt} + n\,\nabla\cdot\underline{V}_i = 0 \qquad (8)$$

In this case, since $\underline{V}_i$ is solely due to the **E** x **B** drift and **E** a is electrostatic, divergence of $\underline{V}_i$ is equal to zero hence

$$\frac{dN}{dt} = 0 \qquad (9)$$

Thus in the F region, density in an element of plasma remains unaltered with time. This implies that the plasma is incompressible in the F region. Coming back to eqn.(6) which is expressed in the rest frame

$$\nabla\cdot(N\underline{V}_i) = \frac{E_z}{B}\frac{\partial N}{\partial y} - \frac{E_y}{B}\frac{\partial N}{\partial z} \qquad (10)$$

The ion density N consists of background density n_o, which has large scale gradients, the perturbation density n, having same variational form as the GWEF and another perturbation density n_1 which does not have the variational form of the GWEF and is ascribable to other effects. Thus

$$\frac{\partial N}{\partial y} = \frac{\partial n_o}{\partial y} + i k_y n + i k_{y1} n_1$$

$$\frac{\partial N}{\partial z} = \frac{\partial n_o}{\partial z} + i k_z n + i k_{z1} n_1 \qquad (11)$$

where k_{y1} and k_{z1} are the wave numbers assignable to the perturbation which does not have the variational form of the GWEF. Substituting for various terms in eqn.(10) from eqn.(11) we get,

$$\nabla\cdot(N\underline{V}_i) = \frac{1}{B}\left(E_z\frac{\partial n_o}{\partial y} - E_y\frac{\partial n_o}{\partial z}\right) + \frac{i n_1}{B}\left(E_z k_{y1} - E_y k_{z1}\right)$$
$$+ i\frac{n}{B}\left(k_y E_z - k_z E_y\right) \qquad (12).$$

since the fields are electrostatic, the last term in eqn.(12) is zero indicating that the irregularity production due to a given field does not depend on the perturbation it produces in the electron density. Defining the electron density scale length,

$$\frac{1}{L_z} = \frac{1}{n_o}\frac{\partial n_o}{\partial z}, \quad \frac{1}{L_y} = \frac{1}{n_o}\frac{\partial n_o}{\partial y} \qquad (13)$$

eqn.(12) reduces to

$$\nabla\cdot(N\underline{V}_i) = \frac{n_o}{B}\left(\frac{E_z}{L_y} - \frac{E_y}{L_z}\right) + \frac{i n_1}{B}\left(E_z k_{y1} - E_y k_{z1}\right) \qquad (14)$$

In chapter III we have found that the amplitude of the

the GWEF is given by

$$E_{oz} = B W_{oy} \psi \qquad E_{oy} = -B W_{oz} \psi \tag{15}$$

where the terms have been defined in chapter III. Using eqns.(2) and (15), eqn.(14) becomes,

$$\nabla \cdot (N \underline{V}_i) = n_0 \psi (W_{oy}/L_y + W_{oz}/L_z) \exp\{i(k_y y + k_z z - \Omega t)\} + i n_1 \psi (W_{oy} k_{y1} + W_{oz} k_{z1}) \exp\{i(k_y + k_{y1}) y + i(k_z + k_{z1}) z - \Omega t\} \tag{16}$$

The second term of eqn.(16) shows that irregularities smaller or larger than the scale sizes associated with the given gravity wave are produced depending on whether the wave vectors are in the opposite or in the same direction. Also, it can be seen from eqn.(16) that irregularities produced due to this mechanism are field aligned as terms in eqn(16) are independent of x. While L_z is dominant all the time, the term containing L_y may be significant only during presunrise and past sunset hours.

4.6.2 Production of irregularities

In chapter III it was found that the value of ψ depends on the conductivity profile, location of the source region and also on the gravity wave parameters, like vertical wavelength. For a gravity wave with a vertical wavelength of

16 km, the value of ψ at the equator, in different situations is given in table 4.1. It can be seen from table 4.1 that for a field line apogee at 200 km, the value of ψ is always larger when the gravity waves are present in the E region. In the case when the field line apogee is at 300 km, the value of ψ during the evening time is more for the gravity waves in the E region than that due to the gravity waves in the F region. Converse is true in the night. As the convergence rate is proportional to ψ, its value will be in accordance with the value of ψ.

In the following section, we examine the irregularity production at the bottom of the F layer, at an altitude of 250 km. We choose this altitude because the in-situ measurements of the electron density during strong spread F have shown that the gradient in the electron density were largest in the 250 km altitude region. If we consider a situation when the field line apogee is at 250 km, the values of ψ at 250 km can be assumed to be the mean between the values at 200 and 300 km. These values are also given in table 4.1. It may pointed out that the daytime, eveningtime and nighttime situations are represented by the conductivity profiles given in chapter III, and should not be mistaken otherwise.

For the formation of irregularities, the convergence rate should be larger than the recombination or the attatchment like recombination rate. With a given electron density N, the loss rate due to the attachment is 10^{-4}N/cc /sec. Assuming

Table 4.1

Field line apogee at	Winds in the E region			Winds in the F region		
	Value of ψ at the equator during the			Value of ψ at the equator during the		
	Daytime	Eveningtime	Night-time	Daytime	Evening time	Night-time
300 km	0.41	0.21	0.05	0.05	0.19	0.35
200 km	0.35	0.28	0.235	0.075	0.12	0.175
250 km	0.38	0.25	0.12	0.06	0.15	0.26

W_{oz} = 20 m/sec, L_z = 100 km during the daytime, and 10 km during the eveningtime and nighttime when the winds are in the E region, convergence rate is 7.6 x 10^{-5}N, 5 x 10^{-4}N and 2.4 x 10^{-4} N/cc/sec. during the day, evening and nighttime, respectively. Thus the electron density irregularities can be produced both during the evening and nighttime.

If the gravity wave winds are in the F region, around 250 km altitude, the convergence rates (using the value of ψ given in table 4.1) during the day, evening and nighttime is 2 x 10^{-6}N, 3 x 10^{-4}N and 5.2 x 10^{-4}N/cc/sec, respectively. Hence, the gravity waves in the F region can produce irregularities in the F region, both during the evening and nighttime.

For a given value of convergence rate, the amplitude of the irregularity depends on the period for which it can grow. The growth period depends on the period of the GWEF, in plasma frame of reference.

Besides the GWEF, the large scale electric fields (E_L) are also present in the equatorial F region. These large scale electric fields give rise to the general drift of the plasma. If the plasma is not drifting, i.e. E_L = 0; the ion convergence due to the GWEF at a given place would take place for half the wave period. In the other half of the wave period the irregularity will annihilate, and the cycle repeats itself.

If the plasma is drifting due to non zero E_L, this time period would be half the Doppler shifted time period which would be larger when the phase velocity of the GWEF is close to, and in the direction of plasma drift velocity. In such a situation, the amplitude of the irregularity will grow for a longer length of time. If the phase velocity of the GWEF is in direction opposite to the plasma drift, the growth period would be much smaller.

The phase velocity of the GWEF would be in accordance with the phase velocity of the gravity waves generating them. Thus the phase velocity of the GWEF would be in downward or upward direction, depending on whether the gravity wave is propagating upward or downward. The F region plasma is known to drift both in upward and downward directions. Irrespective of the direction of the plasma drift and the direction of the phase velocity of the gravity waves, the proposed mechanism will generate the electron density irregularities.

A rough estimate of the percentage amplitude of the irregularities due to the GWEF can be made. If the Doppler shifted time is such that 5 minute (say) are available, for the growth of the irregularities, then the percentage amplitude of the irregularities during the eveningtime when the gravity waves are in the E region is (after putting for various terms in the continuity equation and neglecting the production term)

$$\frac{\delta N}{N} = (5 \times 10^{-4} - 10^{-4}) \times 5 \times 60 = 0.12$$

That is irregularities with 12% amplitude (peak to peak 24%) over the background electron density can be produced. If the

Doppler shifted time period is large, the amplitude of the irregularities would be even larger. But this is a linear estimate which should fail for larger amplitude. Rather nonlinear growth would take place which may result in the generation of smaller scale irregularities due to breaking of such large amplitude irregularities.

Growth of the irregularities due to the GWEF is linear with time and unlike the Rayleigh Taylor instability mechanism, it does not require a pre-existing irregularity amplitude. Hence in the initial stages, it grows faster than the R - T instability which, in the absence of other irregularities, should start from the thermal fluctuation level and thereafter grows exponentially. Before growing to appreciable magnitude, the RTI would therefore require several growth periods to produce irregularities of appreciable magnitude. Hence only after reaching a certain level, the exponential growth of the RTI would be faster than the linear growth provided by the GWEF mechanism. As the irregularities produced by the GWEF are larger in amplitude in the initial stages, they would act, very effectively, as a seed for the growth of the Rayleight - Taylor instability.

In the following we discuss the relative importance of the gravity waves in the E and in the F region in generation of the irregularities by noting some facts about these in the two regions.

Beer (1974) has presented theoretical estimates of minimum vertical wavelength of the gravity waves in different altitudes. At an altitude of about 100 km, the minimum vertical scale size is about 10 km while it is about 50 km at an altitude of 150 km. The minimum scale size increases with the altitude because of the following two reasons.

Gravity waves, during their transmission from lower regions to upper regions of the atmosphere suffer attenuation and reflection (Pitteway and Hines 1963, 1965). Attenuation of the gravity waves is due to the molecular viscosity and thermal conduction. Evidently, the gravity waves with smaller scale sizes should be more attenuated. Attenuation of the waves in the lower regions results in a restricted scale size spectrum of the waves in the upper regions.

Reflection of the gravity waves is due to the gradients in neutral gas temperature and the wind shears which have a larger value in the lower regions. Hence most of the waves are reflected below an altitude of about 200 km. Thus in the E region, gravity waves with both upward and downward phase propagation exist. This implies that in the E region, the gravity waves have a richer scale size spectrum with both upward and downward propagating waves.

The aforesaid arguments on the scale size of the gravity waves in the F region rule out the possibility that the gravity waves with 15-20 km λ_z are present in the F region. In-situ measurements of electron density in the equatorial F region (e.g.Prakash et al, 1981) reveal that the large scale irregularities have vertical wavelengths of the order of 10 km.

It has been pointed out in chapter III that the generation of the GWEF (which in turn give rise to the electron density irregularities in the F region) depends on the Pedersen conductivity, σ_p . σ_p depends on the electron density and the ion neutral collision frequency. Hence any increase in the electron density in the source region would result in the generation of larger electric field, and the transmitted field will also be larger. The layers of ionization in the altitude range 100 to 120 km during the evening and nighttime is quite a common feature. In such cases, if the source is in the E region, the generated field would be even larger than those calculated in chapter III.

Hence all the aforesaid arguments are in favour of the E region gravity wave winds in producing the irregularities in the F region. Also the evening and nighttime are more suitable for their generation.

The vertical gradient scale length used in our calculations is 10 km during the evening and nighttime. Recent rocket measurements (Prakash et al 1981) reveal that L_z could be as small as 4 km at an altitude of 250 km. Hence the convergence rate could be larger than calculated earlier. Therefore, the irregularities of even larger amplitude can be produced through the mechanism proposed here. Or in otherwords, if the Doppler shifted period were less than the assumed period of 5 minute, irregularities with the same amplitude can be produced.

There is a radical difference between the mechanism proposed here for the production of the spread F irregularities and that proposed by Booker (1979) and Klostermeyer (1978) using the gravity wave winds. In their theories, the irregularities are produced by the gravity wave directly through the interaction with the ambient plasma over sufficiently long period of time. This requires that the gravity waves should be present in the region where the irregularities are produced. Also, these theories do not explain the production of spread F irregularities before the reversal of the background filed. The mechanism proposed here is based on the interaction of the gravity wave winds with the ionospheric plasma. resulting in the generation of electric field. These fields, in presence of the background electron density gradients, produce the electron density irregularities. For the production of irregularities in the equatorial F region, the mechanism does not require that the gravity waves be present in the F region. Instead, the gravity waves in the E region, during the evening and nighttime can produce the irregularities in the F region more efficiently **than** the gravity waves in the F region.

Conclusions:

In this chapter, the electron density irregularities in the equatorial F region have been discussed. A new mechanism for the generation of the spread F irregularities has been proposed using the gravity wave induced electric fields (GWEF). The salient features of the studies carried out in this chapter are as follows:

(i) The GWEF, in presence of the background electron density gradients, are capable of producing the electron density irregularities. The production of the irregularities through this mechanism does not require the pre-existing electron density irregularities.

(ii) The irregularities thus produced have a somewhat sinusoidal shape and these may grow nonlinearly depending on the direction of the background electric field. If the background electric field is such that the plasma drifts in the direction of the phase velocity of the gravity wave, and that the two velocities are nearly same for sometime, the irregularities can grow to a very large amplitude. Even if the two velocities are not in the same direction, irregularities of smaller amplitude would still be produced.

(iii) Unlike the other mechanisms using the gravity wave winds for the production of the irregularities in the F region, in our case, the gravity waves need not be in the region where the irregularities are produced. For the case when the field line apogee is at 200 km, the gravity waves in the E region will be more effective than those in the F region (at 200 km) both during the evening and night. In the case when the field line apogee is at 300 km, the gravity waves in the E region during the eveningtime will be more effective in producing the irregularities. In the case when the field line apogee is at 250 km, gravity waves in the E region during the evening and nighttime are more effective.

(iv) Since the growth of the irregularities due to the GWEF is linear with time, they grow faster than the ones produced by the Rayleigh-Taylor instability mechanism. As the irregularities generated through the R-T mechanism should grow from the thermal fluctuation level, hence they would require several e-folding growth times to be of significant amplitude.

(v) The irregularities due to the GWEF may facilitate the growth of the R-T instability by acting as a seed to the latter.

CHAPTER V

ELECTRIC FIELDS AND ELECTRON DENSITY MEASUREMENTS IN THE EQUATORIAL E REGION

This chapter contains the experimental studies on the measurements of electric fields and electron density in the equatorial E region. The experiments were conducted from Thumba, India when the electrojet was strong; as confirmed by the appearance of type I echoes observed using the groundbased VHF backscatter radar.

While the electric field experiment was solely a PRL project, the electron density experiment was carried out as a part of ISRO-CNES collaborative programme.

The rocket with the electric field payload was launched from Thumba, India on December 1, 1978 at 1236 hrs IST.

The set of rockets each carrying Indian and French payloads, for the measurement of electron density were launched on August 25, 1979 at 1151 hrs IST and August 31, 1979 at 1121 hrs IST, respectively.

These studies are presented in section A and in section B. Section A is devoted to the electric field measurements while section B is on the electron density measurements. Contents of this chapter are as follows.

Section A - Electric Fields Measurements

5.1 Introduction

Besides being ambient parameter of the medium, electric fields in the ionosphere and magnetosphere are very important to various physical processes operative in these regions. In the equatorial E and F region, they are responsible for the equatorial electrojet, equatorial anomaly and maintenance of nighttime E layer. Also, they are basic to various plasma instabilities in the equatorial E and F regions, giving rise to electron density irregularities.

Importance of electric fields was realised long time ago and since then, attempts have been made to measure these using different techniques. However, the efforts to measure the electric fields using the insitu probes, at the equator, are few. The reason for a limited number of attempts being the difficulties in measuring these fields, as will be discussed later.

The present knowledge of electric fields in the equatorial electrojet region is mainly derived from the phase velocity measurements of the electron density irregularities using the VHF backscatter radars at Jicamarca, Peru and Thumba, India. But these measurements suffer on account of low height resolution, and also since these measurements are indirect, have certain limitations.

An estimate of the electric fields in the electrojet region was made by Subbaraya et al (1972) from the electrojet currents, calculated using the data of rocket borne magnetometers, and from the electron density measurements using the Langmuir probes. It was found that the electrojet peak (determined by the current density profile) was at 106 km, which was consistently above the σ_3 peak. The σ_3 profile was calculated using the neutral density model and the observed electron density profiles. Since the electrojet current is given by $\underline{J} = \sigma_3 \underline{E}_p$ where $\underline{E}_p$ is the primary east-west field. If one assumes $\underline{E}_p$ to be independent of height, σ_3 peak should coincide with the peak in the current $\underline{J}$. The observed difference in the height of the two peaks would mean that actual conductivity profile is different from what had been evaluated. This could be due to inadequacies in the neutral atmospheric model used. Quite a drastic change in the atmospheric models would be needed to lift the σ_3 profiles upwards by about 5 km and make the peak in σ_3 profile and the current profile coincide.

The other argument to explain the discrepency in the peaks of $\underline{J}$ and σ_3 was based on the vertical variation of the primary east-west field. Thus the electric field measurements are very essential to the development of electrojet models.

Rocket borne studies of the electron density irregularities at Thumba, India, showed that when the electrojet currents were strong, the amplitude profile of small scale (1-15 m) irregularities was very well correlated with the profile of the drift velocity of electrons (Prakash et al, 1971). As has been pointed out in Chapter III, the only mechanism put forward for the direct generation of small scale irregularities in the equatorial electrojet is the two stream instability mechanism which requires a threshold value of the electron drift velocity relative to the ions. The rocket borne studies (loc.cit) have shown that although the threshold criterion was not satisfied, irregularities were observed. For these studies, the currents were derived from the measurement of proton precession magnetometers which had a height resolution of a few km. In addition, the currents derived from the magnetometers are based on the assumption that the currents are constant over a large distance in the north south direction. Hence, the studies carried out earlier, do not rule out the possibility of the threshold criterion being satisfied in the localised regions. In fact, there are indications of the threshold criterion for the excitation of two stream plasma instability getting satisfied in the localised region, as the small scale irregularities were observed in the form of bursts. This would imply that fluctuating electric fields of large amplitude are present in the localised regions.

Thus a comprehensive study of both large scale (dc) and small scale (ac) electric fields in the equatorial electrojet region is essential.

5.2 Measurement Techniques:

The electric field measurement techniques can broadly be classified under two heads,

(a) Bulk flow method

Of this, the most widely used methods at the equator are

(i) Artificial Barium cloud method

(ii) Dopplershifts of radar backscattered signals.

In the bulkflow method of measurements, the plasma bulk flow velocity V_B, is determined and the electric field is calculated using the relation $\underline{V}_B = (\underline{E} \times \underline{B})/B^2$ (1)

(b) Langmuir double proge technique

In this, potential difference between a pair of sensors that are placed in the ionosphere is measured. The electric field is obtained by dividing the potential difference with the separation distance between the two sensors.

We now discuss briefly, these techniques and their applicability to measuring the electric fields in the ionosphere.

5.2.1 Artificial Barium Cloud Method:

In this method of measuring electric fields, ionizable vapors are released at suitable altitude in the sunlit ionosphere. The Sun's ultraviolet radiation ionizes these vapors and these ions resonantly scatter the sunlight at several wavelengths which is visible in the red part of the visible spectrum. By following the subsequent motion of ions by groundbased optical techniques, the electric field is obtained by using the trajectory of these clouds. There is a complex relationship between the cloud velocity and the perpendicular electric field which, under certain assumptions, is given by (e.g. Mozer 1972)

$$\underline{V}_B = \frac{2}{(1+\lambda^*)}\left\{(\underline{E}\times\underline{B})/B^2 + (\underline{E}_{\perp}/B + (V_n\times\underline{B})/B^2))/K\right\} + \frac{\lambda^*-1}{\lambda^*+1}\,\underline{V}_{\parallel} \qquad (2)$$

where λ^* = ratio of height integrated Pedersen conductivities in the presence and absence of the cloud

K = ratio of gyration to collision frequency of the Barium ions.

$\underline{V}_n, \underline{V}_{n\perp}$ = neutral cloud velocity in the reference frame fixed with the earth and its perpendicular component.

$\underline{E}, \underline{E}_\perp$ = the ionospheric electric field in the fixed frame of reference and its perpendicular component.

This technique is useful only for the measurements of large scale electric fields. The major disadvantage of this technique is that the field measurements can be made only at the twilight hours. In addition, this technique can not be used to measure the electric fields in the electrojet region as the technique is usable only above 130 km altitude.

Electric field measurements at the equator have been made by Reiger (1971) and Anandarao et al (1976 b) using this technique.

5.2.2 Dopplershifts of radar backscattered signals:

This method is based on the scattering of an electromagnetic wave. Electromagnetic waves of frequencies, much higher than the plasma frequency of the medium are backscattered Incoherent scattering occurs if the electron mean free path exceeds the radio wavelength and also the scale size of the irregularities, occuring satistically owing to the random thermal motion.

In the absence of the irregularities (other than those due to the thermal motion), the Dopplershift in the backscattered signal (compared to the transmitter frequency) gives the bulk velocity of the ionosphere. The electric field can be calculated using the eqn.(1).

In the presence of the irregularities, the Doppler shift in the backscattered signal gives the phase velocity of the irregularities in the medium. If the mechanism for the generation of irregularities is identified, this velocity can be related to the bulk velocity of the medium.

The major drawback of the technique is that the Doppler-shift can be caused by the motions other than the $\underline{E} \times \underline{B}$ drifts; such as, the motion of the neutral atmosphere, gravity waves, contraction of the F layer etc. Also, with one given setting of the antenna, only one component of the field can be deduced. Hence, simultaneous measurement for various components of the electric field cannot be made using this technique.

At the equator, the electric fields have been deduced using this technique by Balsley (1965, 1969), Carru et al (1967), Woodman and Hagfors (1969), Farley et al (1970) and Prakash and Muralikrishna (1979) etc.

5.2.3 Langmuir double probe technique:

This is an insitu technique of measuring electric fields. This technique has widely been used on board balloons, rockets and satellites.

The voltage between a pair of isolated conductors on board a space vehicle, separated by a distance d in the ionospheric plasma is given by (Mozer, 1968)

$$\Delta V = \left\{ \frac{\underline{E}' \cdot \underline{d} + (V_1 - V_2) + (WF_1 - WF_2)}{1 + (R_1/R) + R_2/R} \right\} \qquad (3)$$

where $\underline{E}'$ is the electric field in the moving frame of reference and is related to the field ($\underline{E}$) in the earth fixed frame by

$$\underline{E}' = \underline{E} + \underline{V} \times \underline{B} \tag{4}$$

$\underline{V}$ is the velocity of the moving frame with respect to the earth. R_1 and R_2 are the sheath impedances for the sensors one and two respectively. R is the input impedance of the measuring device. V_1 is the floating potential of sensor one when $R = \infty$. WF_1 is the work function of sensor one. Thus ($WF_1 - WF_2$) is the difference in contact potentials of the two sensors.

While it is desired to measure $\underline{E}$, the rest of the terms appearing in eqn(3) are the error terms. In the following, we investigate the importance of each term of eqn.(3).

V x B field

A conductor moving with a velocity $\underline{V}$, in presence of magnetic field ($\underline{B}$), developes an induced electric field $\underline{V} \times \underline{B}$. In the ionosphere, the induced electric field can be very much larger than the ambient electric field $\underline{E}$. In the equatorial E region, the horizontal and vertical fields have been estimated to be about 0.5 mV/m and 10-15 mV/m, respectively. Thus, in case of a rocket moving with a vertical velocity of 1 km/sec and horizontal velocity of 300 m/sec, the induced electric field in the horizontal and vertical direction is 30 mV/m and 9 mV/m, respectively. Hence the errors due to the $\underline{V} \times \underline{B}$ effect is 60 times the ambient horizontal field, while it is of the same order of magnitude in case of the vertical electric field.

The $\underline{V} \times \underline{B}$ field can be calculated if the velocity vector and the orientation of the rocket with the geomagnetic field are known very accurately. To measure the horizontal electric field with an accuracy of 0.1 mV (the peak electric field is, say, 1mV/m), the aspect information at the equator, should be available with an accuracy better than 1/5 of a degree. This requires a highly sophisticated aspect sensing device to measure the horizontal electric field. The requirements for the measurements of vertical electric fields are not so stringent.

$WF_1 - WF_2$ term

The error field due to the difference in contact potentials of the sensors is, to first order, a dc field . This difference could be as large as a few hundred millivolts if proper precautions are not taken. Rotation of the rocket can be made use of to eliminate this error field, as this would appear as a dc offset voltage in the output. However, this method can be used only to correct the field perpendicular to the spin axis of the rocket.

Another difficulty in the measurements arises if the work function on the surface of the sensor is not uniform. An ac signal would be generated when a sphere having differing work functions on its surface rotates in an anisotropic medium. This signal may be even larger compared to the fields present in the medium.

To minimise the effects due to the difference in contact potentials of the sensors, the sensors are coated with carbon to have a surface with uniform work function. Laboratory experiments have shown that this type of coating gives quite satisfactory results.

$V_1 - V_2$ term

Ionospheric plasma is anisotropic due to the presence of the geomagnetic field. The anisotropic character of the medium may result in differing floating potentials of the two sensors. To minimise this effect, the sensors are made symmetric and are mounted symmetrically with respect to each other and the axis of the rocket. The major source of error arises due to the rocket wake which can not be accounted for or predicted. The only way to surmount the problem is to mount the sensors on booms which are appreciably long so as to keep the sensors away from the rocket body.

The denominator term:

This term arises due to the fact that the input device which measures the difference in potentials of the two sensors does not have an infinite input impedance (R). The errors arising due to this can be made small by using the input device which has a very high input impedance or by decreasing the sheath impedance (R_1 and R_2). This decrease can be affected by feeding a small, finite electron current to the sensors. The value of the current should be small enough to keep the potentials of sensors in the vicinity of the floating potential and that it should never become positive. The theory of this technique has been given by Falheson (1967) and has been employed on several experiments (e.g.Falheson et al, 1970).

5.3 Measurements with Langmuir Double Probes at Thumba, India:

The Langmuir double probes technique has been used to measure the electric fields in the auroral zones (e.g.Mozer and Falheson, 1970). While the ambient electric fields in the auroral zone are large compared to the low latitude fields, the error fields due to the $\underline{V} \times \underline{B}$ effect are smaller. Attempts to measure the electric fields over the equator, at Thumba,India have been made (Sartial, 1972). The values of the horizontal electric field from this experiment were an order of magnitude larger than those estimated theoretically. Results on the fluctuating horizontal electric fields have been reported by Sampath and Sastry (1979). They observed the fluctuating fields in the altitude range 87 to 103 km. However, they did not carry out any quantitative studies of these fields.

Because of the uncertainties in the contact potentials of the sensors, it is very difficult to measure the large scale (dc) vertical fields. However, fluctuations and the large scale variation in the vertical field with the altitude can be measured using the "Sample and hold" method described in section 5.3.3. To eliminate the $\underline{V} \times \underline{B}$ effect, we had proposed a new technique, which was also put to test. Thus the aims of the experiment were

(i) To put to test a technique to eliminate the $\underline{V} \times \underline{B}$ effect

(ii) To measure the small and large scale variations in the vertical electric field.

5.3.1 The present approach:

As has been pointed out earlier, the main difficulty in the measurements of electric field arises due to the fact that the induced electric field is much larger than the ambient electric field $\underline{E}$. $\underline{V} \times \underline{B}$ term can not be measured and hence has to be calculated. For an accuracy of 10% in the horizontal electric field (nominal value be 1 mV/m) measurements at the equator, the factor $\underline{V} \times \underline{B}$ should be known with an accuracy of 0.3%. The principle of the technique, proposed by us, is as follows.

As shown in fig.5.1, let C and D be two sensors introduced into the plasma on two booms extended on either side of the rocket. The two sensors will develop the potentials depending on the plasma parameters and the ambient electric field. The potential difference between C and D when they are stationary is

$$V_C - V_D = \underline{E} \cdot (\underline{l}_1 + \underline{l}_2) \qquad (5)$$

where $(l_1 + l_2)$ is the separation distance between the two sensors. If C and D move with the rocket with a velocity $\underline{V}$, the potential difference between them is given by

$$(\underline{E} + \underline{V} \times \underline{B}) \cdot (\underline{l}_1 + \underline{l}_2) \qquad (6)$$

The same expression can be derived in the following way. In practice, to determine $V_C - V_D$, the outputs have to be brought to common point in the rocket. In the process of

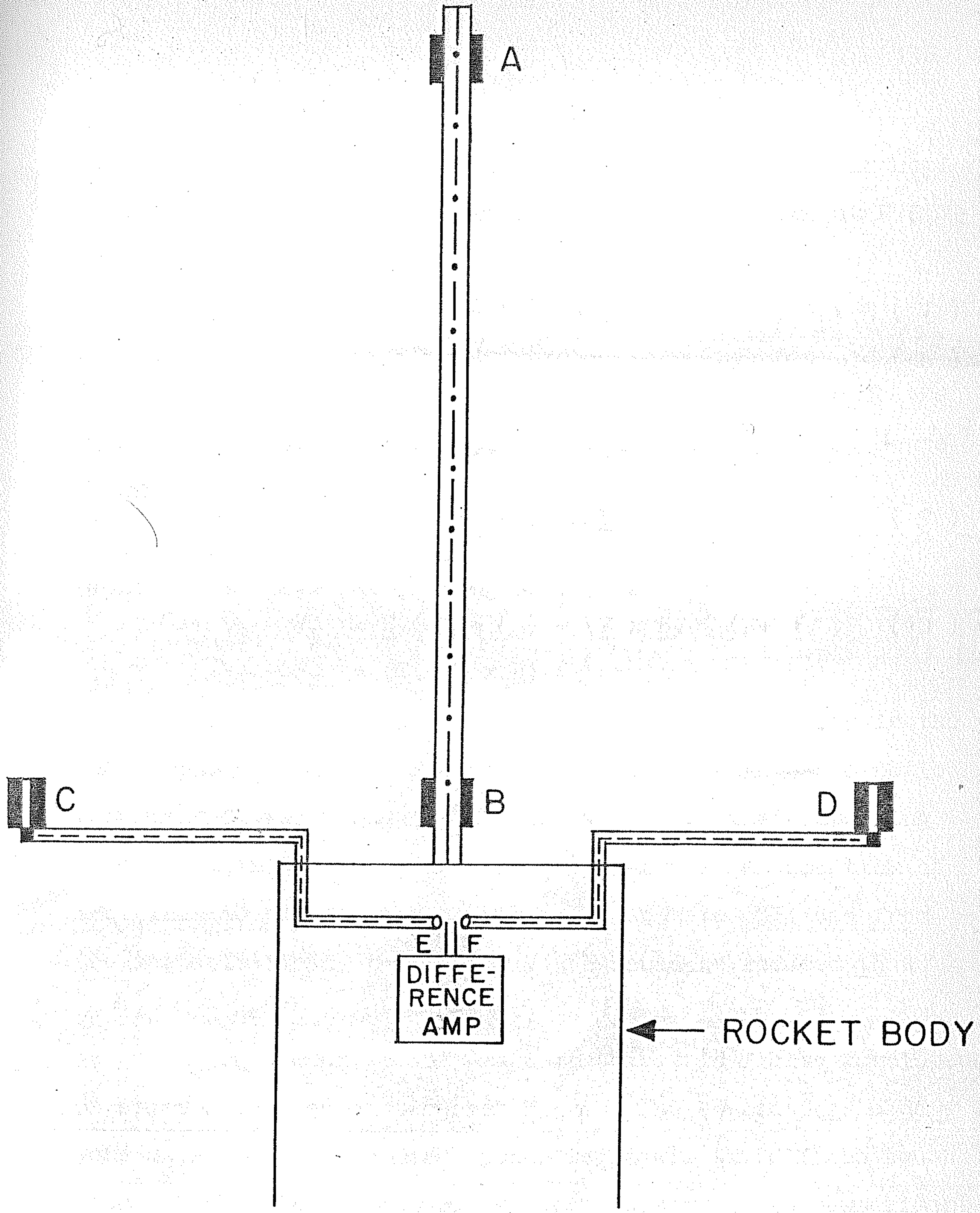

FIG. 5.1. SCHEMATIC OF SENSOR MOUNTING
E-FIELD EXPERIMENT

bringing the signal from C to E and from D to F, the induction field gets added up. The potential at E (V_E) and at F (V_F) are given by the expressions

$$V_E = V_C + (\underline{V} \times \underline{B}) \cdot \underline{l}_1 \qquad (7)$$

$$V_F = V_D - (\underline{V} \times \underline{B}) \cdot \underline{l}_2 \qquad (8)$$

The negative sign in eqn.(8) arises because in this case the sense of the distance is opposite to that in eqn.(7). Hence we get,

$$V_E - V_F = V_C - V_D + (\underline{V} \times \underline{B}) \cdot (\underline{l}_1 + \underline{l}_2) \qquad (9)$$

which can be re-written using eqn.(5) as

$$V_E - V_F = \underline{E} \cdot (\underline{l}_1 + \underline{l}_2) + (\underline{V} \times \underline{B}) \cdot (\underline{l}_1 + \underline{l}_2) \qquad (10)$$

$$V_E - V_F = (\underline{E} + \underline{V} \times \underline{B}) \cdot (\underline{l}_1 + \underline{l}_2)$$

Therefore, it can be seen that the $\underline{V} \times \underline{B}$ effect arises in the leads connectiong C to E and D to F. Using high μ magnetic material, it was thought practical to shield the connecting leads from the ambient magnetic field with an attenuation of more than 60 dB. If the connecting leads are shielded from the magnetic field, the factor $\underline{V} \times \underline{B}$ could be reduced to a negligibly small value.

Our rechnique of measuring electric fields consisted of sensors mounted on two side booms. The connecting leads were shielded with μ metal tubes to reduce the $\underline{B}$ field by about 60 dB. This technique was put to test in the experiment discussed here.

5.3.2 Sensor mountings

As shown in fig.5.1, two cylindrical sensors A and B mounted on a boom, along the spin axis of the rocket were used to measure the vertical electric field. The distance between the sensors was about 1 meter. Since our arrangement of sensors is spin symmetric, the potential of the sensors would not depend on the spin of the rocket.

Another set of cylindrical sensors (C and D) mounted on two side booms was used to measure the horizontal electric field. The booms were deployed sideways during the course of the rocket flight. Connecting lead of the sensor D to the electronics of the payload was shielded using high μ metal tubes. The distance between the side sensors was about 1 meter.

5.3.3 Payload

Electronics of the system was very simple and straight forward. Hence the individual circuits are not discussed here. Fig. 5.2 shows the block diagram of the electric field payload detailing various measurements made in this experiment.

Vertical electric field:

Both d c and a c field measurement were carried out. Potential of the sensors A and B were measured with respect to the body using high impedance input operational amplifiers in the emitter follower mode. The voltage follower outputs were telemetered alternately using a channel selector, after suitable amplification and level shifting. The level shifting

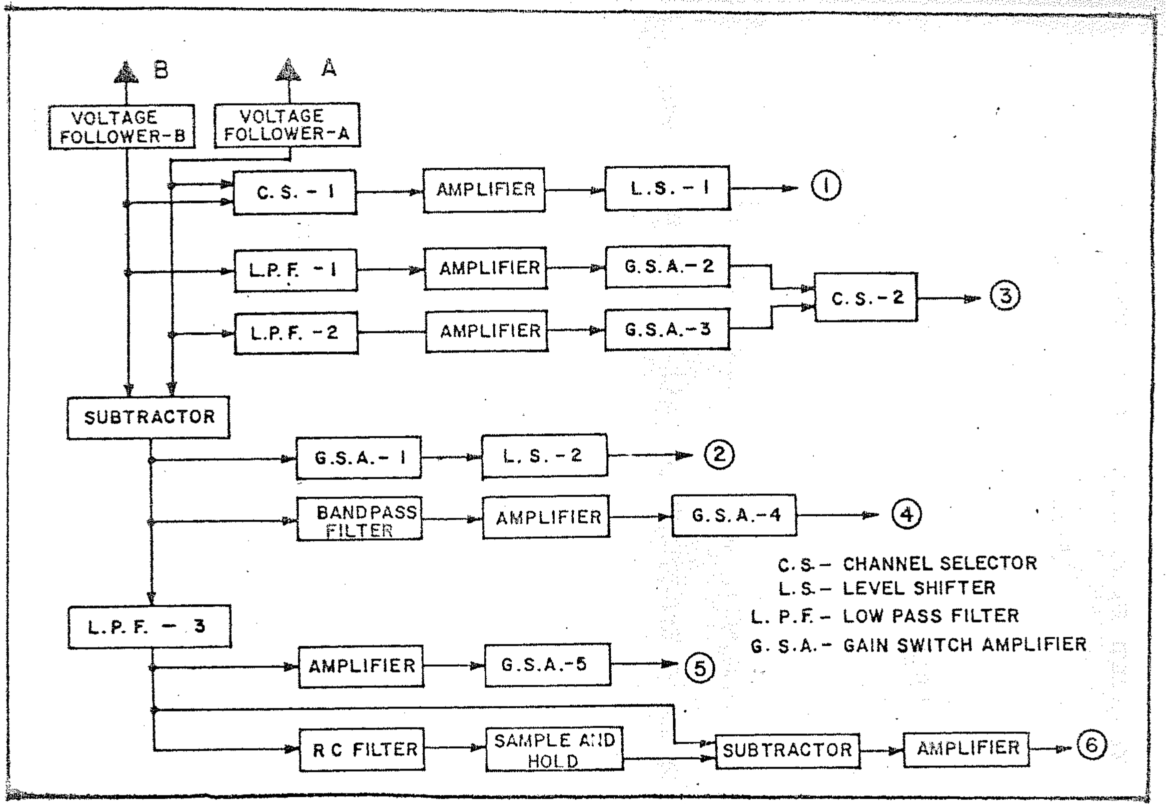

FIG. 5. 2. BLOCK DIAGRAM OF ELECTRIC FIELD EXPERIMENT

was such that the signal varied about 2.5 V level. This level shifting was done to cover both negative and positive potentials of the sensors. This output was telemetered on 10.5 KHz telemetry channel, marked 1 in the diagram.

Vertical d c field was measured by subtracting the potential of B from that of A in subtractor. The subtractor output was given two gains, alternately, in the gain switch amplifier (G.S. A-1). This output was again level shifted with respect to 2.5 V in the level shifter (LS. 2) and telemetered on 14.5 KHz channel, marked 2 in the diagram.

Fluctuations in the potentials on the sensors A and B were measured in the frequency range upto 20 Hz using the low pass filters (L.P.F-1 and L-P.F-2 respectively). The filter outputs were suitably amplified by amplifying with different gains (G.S.A-2 and G.S.A-3). The outputs of the gain switch amplifiers were telemetered alternately by a channel selector (C.S-2) on 30 KHz channel marked 3. The channel selector also level shifted the output to be around 2.5 volt level. A maximum signal of ±10mV was thus handled.

Fluctuations in the vertical field in frequency range (10-100)Hz were measured by passing the subtractor output through a band pass filter (10-100 Hz). The filter output was suitably amplified, giving two gains alternately and telemetered on 52.5 KHz channel, marked 4. The signal was level shifted with respect to 2.5 volt level in the gain switch amplifier (G.S.A-4) to measure ± 5 mV fluctuations was such that the signal varied about 2.5 V level. This level shifting was done to cover both negative and positive potentials of the sensors. This output was telemetered on 10.5 KHz telemetry channel, marked 1 in the diagram.

Vertical d c field was measured by subtracting the potential of B from that of A in subtractor. The subtractor output was given two gains, alternately, in the gain switch amplifier (G.S. A-1). This output was again level shifted with respect to 2.5 V in the level shifter (LS. 2) and telemetered on 14.5 KHz channel, marked 2 in the diagram.

Fluctuations in the potentials on the sensors A and B were measured in the frequency range upto 20 Hz using the low pass filters (L.P.F-1 and L-P.F-2 respectively). The filter outputs were suitably amplified by amplifying with different gains (G.S.A-2 and G.S.A-3). The outputs of the gain switch amplifiers were telemetered alternately by a channel selector (C.S-2) on 30 KHz channel marked 3. The channel selector also level shifted the output to be around 2.5 volt level. A maximum signal of ±10mV was thus handled.

Fluctuations in the vertical field in frequency range (10-100)Hz were measured by passing the subtractor output through a band pass filter (10-100 Hz). The filter output was suitably amplified, giving two gains alternately and telemetered on 52.5 KHz channel, marked 4. The signal was level shifted with respect to 2.5 volt level in the gain switch amplifier (G.S.A-4) to measure ± 5 mV fluctuations in the vertical field.

Fluctuations in the vertical field upto a frequency of 20 Hz and input level ± 10 mV were also measured. This was done by passing the subtractor output through a low pass filter (L.P.F-3). The filter output was given two different gains in the gain switch amplifier (G.S.A-5). The gain switch amplifier provided a level shift also and hence the signal was measured with respect to 2.5 volt level. This output was telemetered on 40 KHz channel, marked 5 in the diagram.

Large scale variations upto 8 mV/km in the vertical electric field were also measured. This method of measuring large scale variations has been referred to as Sample and hold" here. For this purpose, the low pass filter - 3 output was rectified and its d c level was obtained every 2 sec. This d c voltage was subtracted from the output of L.P.F-3 and suitably amplified. The output was telemetered on 22 KHz channel, marked 6 in the diagram.

Horizontal electric field:

Since the main aim was to test our idea of shielding, no detailed measurements were planned. Unshielded and shielded outputs of sensors C and D respectively, were measured by high input impedance operational amplifiers. These outputs were passed separately through two low pass filters and amplified. The amplified outputs were level shifted in the gain switch amplifiers and telemetered alternately through a channel selector on 7.35 KHz channel. This channel is not shown in the block diagram. The channel was similar to the one used for the fluctuating potential of sensor A or B (Channel-3).

5.4 Results and Discussions:

Fig. 5.3 gives the telemetry record of the flight. In this figure, the channel output marked H gives the results of the horizontal electric field measurements. It has been pointed out earlier, the connecting lead of sensor D alone was shielded using the high μ metal tube. If the shielding were effective in reducing the $\underline{V} \times \underline{B}$ field, the outputs corresponding to the potential of the two sensors should have been of different magnitudes. For one of the sensors (D), the magnitude should have been small. But, it can be seen from fig.5.3 that theoutputs of the two sensors are of equal amplitude.

Hence it can be concluded that the $\underline{V} \times \underline{B}$ effect cannot be eliminated by shielding the connecting leads from the sensors to the electronics of the payload. The lacuna in the logic proposed here for the elimination of $\underline{V} \times \underline{B}$ effect is not yet clear.

The results on the measurement of small scale vertical electric fields are quite encouraging. Fig.5.4 gives the telemetry record in which channel marked V gives the measurements on small scale vertical electric fields. It can be seen from fig.5.4 that large fluctuations in the vertical electric field are present.

Such fluctuations were observed in the altitude range of 90 km to 104 km in the frequency range of 2 Hz to 20 Hz.

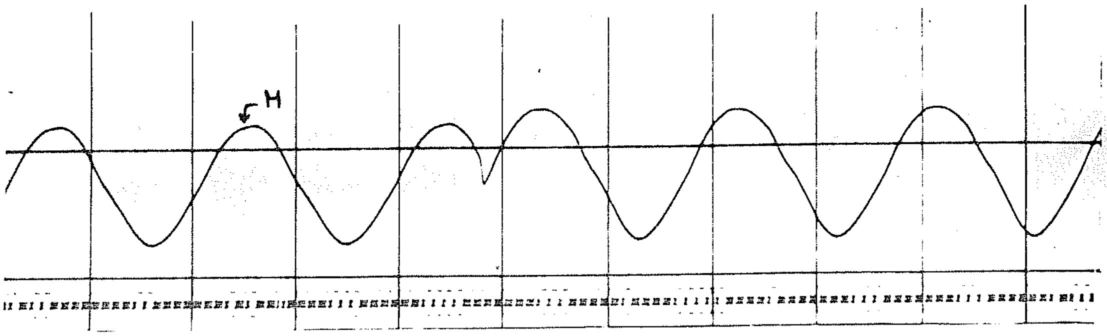

FIG. 5·3

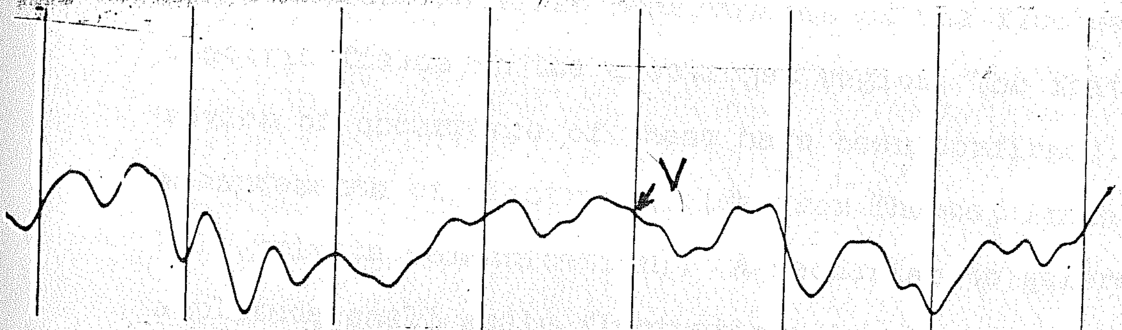

FIG. 5·4

The fluctuating fields were measured both during the rocket ascent and descent.

Due to drift of the electronic circuits, an estimate of the amplitude of these fluctuations could not be made with confidence. Hence quantitative estimates are not presented here.

This is the first measurements of the fluctuating vertical electric fields in the electrojet region. The features and region of occurrence of these have been confirmed by recent measurements of electric fields from Thumba, India (Prakash and Pal, private communication). A mechanism to generate such large amplitude small scale fluctuations in electric field is not available. However, these may arise due to the cross field instability mechanism or due to the acoustic waves (not the acoustic gravity waves) in the neutral medium (Prakash, private communication).

Section B - Electron Density Measurements

5.5 Introduction

In this section, the results on the measurements of electron density in the equatorial E region at Thumba, India, using different techniques is discussed. The experiments were a joint venture of Indo-French Scientists under the auspicies of ISRO-CNES collaborative programmes. The experiments were aimed at measuring the electron density and electron density irregularities using the Langmuir Probe (LP), mutual admittance probes (MAP) and the self oscillating probes (SOP). The SOP was developed by IUT Bourges (University of Orleans) France while the other two payloads were developed at Physical Research Laboratory, India.

Extensive studies on the electron density and electron density irregularities have been made at Thumba, India, using mostly the Langmuir Probes. These studies have resulted in the identification of the causative mechanisms and also in the classification of these irregularities (Prakash et al, 1970, 1971 a,b, 1973, 1976, 1979). The Langmuir Probe technique for these measurements has been discussed by Prakash and Subbaraya (1967).

The current collected by L.P sensor is converted into the electron density by calibrating the current measurements with the help of ground based ionosonde data. This calibration is not very accurate because of the limitations of the ionosonde technique in determining the electron density. Hence a factor which is not yet known properly is the ratio between ambient electron density and the current collected by the L.P. This factor has to be determined experimentally, as the theories of the LP in the lower E region are not yet known satisfactorily.

It is well known that any medium has certain natural modes of oscillation. Similarly, plasma has many modes of oscillations which can be excited by impressing upon it the required frequencies. The plasma is inductive below the plasma frequency and is capacitive above this frequency. Hence the characteristic frequencies of the ionospheric plasma can be obtained using the radio frequencies.

Radio frequency probes (r.f probes) have been used in the ionospheric research for many years. The r.f. probes which have been employed for such studies can be categorized as

(i) Resonance relaxation probe
(ii) Resonance rectification probe
(iii) Admittance probe
  (a) Mutual admittance probes
  (b) Self admittance probe
(iv) Capacitance probe.

In the resonance relaxation probe system, an r.f frequency sweep (in the desired range) is pulsed at a fixed rate and is transmitted for a short time (usually a few tens of μ sec.). The receiver system is made to lag behind by a few μ sec to observe the resonances of very short duration. Such systems have been used onboard satellites and given information on the plasma waves in the ionosphere.

The resonance rectification probe uses an r.f voltage on a sensor and by measuring the changes in the d c potential of the probe, electron density can be determined. The d c potential changes because of the flow of a rectified current.

Admittance probes are based on the measurement of self admittance of a probe or the mutual admittance between two probes.

The method of self admittance probe is based on the application of a radio frequency sweep on a sensor. The amplitudes of the in-phase and quadrature components of the r.f. current are measured by phase sensitive detectors. Thus the conductance and susceptance characteristics of the sensor can be used to determine the plasma frequency of the medium which , in turn, can be used to calculate the electron density in the medium.

In the mutual admittance probe system, a swept frequency r.f. signal, transmitted by an onboard (space vehicle) transmitter is picked up by an onboard receiver. The received signal contains the information on the mutual admittance of the medium, which can be used to determine the electron density in the medium. The effects arising due to the self admittance may complicate the observations if the two antenna are not separated by a large distance. Hence, the two antenna should be as far as possible.

The capacitance probe technique utilizes the capacitance of the sensor in the tank circuit. Since the plasma is a dielectric medium, whose dielectric constant is a function of the electron density in the medium, the capacitance of the probe (sensor) varies depending on the electron concentration of the medium. By noting the change in frequency of the tank, due to a change in density, the electron density can be determined.

Hiekkilla et al (1968) have reported the results of an intercomparison campaign of various r.f.probes. These experiments have established the suitability of r.f.probes to measure the electron density. Their suitability has been established by the topside sounders on board Alouette satellite (Calvert and Goe, 1963, Fejer and Calvert, 1964). Since then several satellite observations have confirmed these features and added new information on the plasma waves in the ionospheric plasma.

A new version of the mutual admittance probes system was developed by Prakash et al (1972). This system is superior to the mutual admittance probe system reported by Hiekkilla et al (1968), as they had to use long booms, deployed sideways, for their experiment. The electron density can be determined very accurately by observing the resonance at the upper hybrid frequency using the M.A.P. The MAP system (Prakash et al, 1972) have been flown successfully from Thumba earlier and have given various types of resonances, besides that at the upper hybrid frequency, f_T (Rao and Prakash, 1977). The electron density profile obtained using the MAP can be used to calibrate the LP.

The electron density can also be determined using the self oscillating probe. This system had been flown earlier from the Heyss Island in the polar region to confirm the theory of SOP. Results of this flight have been reported by Beghin et al (1976). The oscillation frequency f_R, of the SOP, when the earth's magnetic field is aligned with the cylindrical antenna of the SOP, is related to the plasma frequency f_p, of the medium by

$$f_p^2/f_R^2 = 2\,(1 - f_H/f_R) \qquad (11)$$

where f_H is the gyrofrequency of the electrons. By calculating f_p, the electron density can be determined. The SOP can measure the electron density for $n_e \geq 8 \times 10^3$ electrons/cc.

Hence a comparative study of the three techniques was aimed at to findout the suitability of each of these for the measurements of electron density. Irregularity measurements using the LP and SOP were also aimed at. Such studies were not carried out earlier.

Since the SOP system was not ours, we shall discuss the LP and MAP systems only. Of these two, the LP system and its electronic circuitary have been discussed in detail earlier (Prakash and Subbaraya 1967; Gupta 1970; Sinha 1976).

5.6 Mutual Admittance Probe System:

The MAP system was a modified version of the earlier system (Rao, 1981). Hence we shall discuss only the block diagram and the few modifications incorporated for the studies reported here.

The MAP system consisted of an exciter and a receiver antenna, concentric with the spin axis of the rocket. Hence the observations made by this system were independent of the rocket spin. Physical separation between the exciter and receiver antenna was about one meter. Fig.5.5 shows the schematic arrangement of the experiment. Geometry of the MAP system was such that the lines of equipotential force field had to traverse a distance in the medium, which was much larger than the physical separation between the two antennae; and away from the rocket body. Hence the information carried by them was free of the disturbances in the medium, produced by the rocket nearby its body.

SCHEMATIC OF THE ARRANGEMENT OF THE L.P, MAP AND SOP EXPERIMENTS

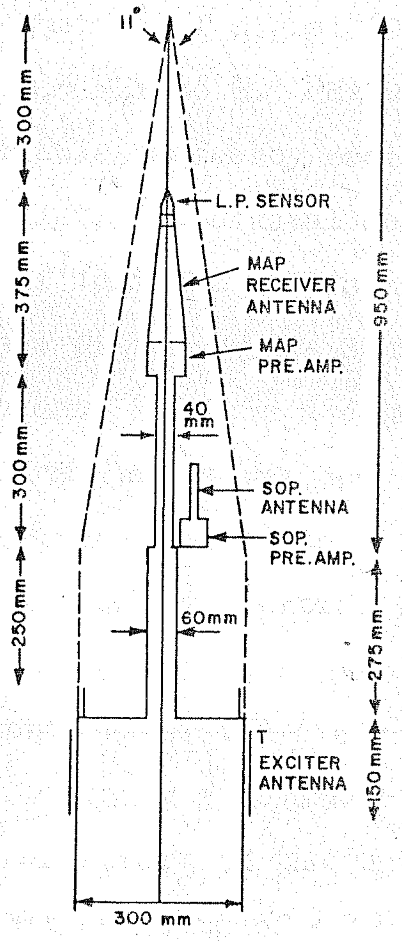

FIG. 5.5

The system consisted mainly of two parts, a swept frequency transmitter and superhetrodyne receiver, synchronous with the transmitter. Block diagram of the electronic system is shown in fig. 5.6 .

5.6.1 Transmitter:

A swept frequency r.f signal (0.5 V peak to peak) in the frequency range 0.5 MHz to 6.5 MHz was generated by mixing the outputs of a variable frequency oscillator (VFO) or local oscillator with that of a crystal oscillator, oscillating at a fixed frequency of 13.1 MHz. This mixed signal was passed through a low pass filter ($f_c \simeq$ 8 MHz) to remove the higher frequency side hands. To have a constant amplitude transmitter signal, the filtered output was fed to an automatic gain control circuit which detected the filtered output. The detected output was used to control the overall output by feeding it back to the wide band mixer.

The VFO circuit generated a signal in the frequency range 13.6 to 19.6 MHz by using a reversed biased variable capacitance diode (varicap) as a part of the tank circuit of the local oscillator. A voltage sweep of + 12 V to 0.5V was applied across the varicap diode which varied the capacitance in the tank to generate the signal in the required frequency band. The repetetion cycle of the voltage sweep was about 1 sec.

5.6.2 Receiver

The receiver system was designed to cover a dynamic range of about 90 dB. Various units of the receiver system are

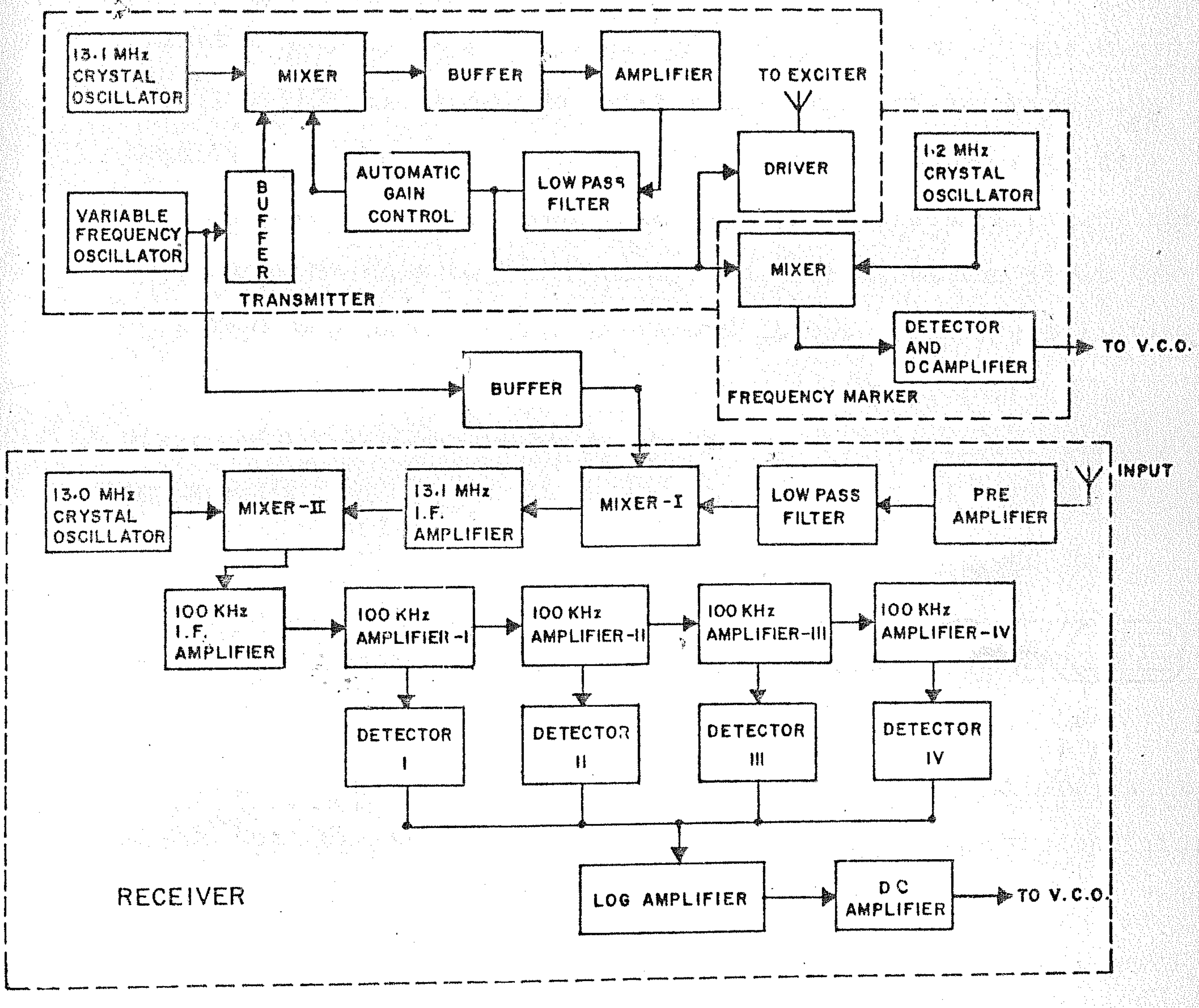

FIG. 5.6. BLOCK DIAGRAM OF M.A.P. SYSTEM

briefly discussed below.

The received signal was amplified in a preamplifier and passed through a low pass filter ($f_c \simeq$ 8 MHz) to remove any unwanted high frequency signal. The filtered output was mixed with the VFO signal in the first mixer. The mixer output was amplified in the first intermediate frequency tuned amplifier (I.F.amplifier) at 13.1 MHz. Since it is impractical to detect the signal at this high frequency, the output of the first I.F amplifier was mixed with crystal oscillator signal, oscillating at a fixed frequency of 13.0 MHz, in the second mixer. The mixer output was amplified in the second I.F amplifier tuned at 100 KHz.

To cover a dynamic range of 90 dB, the output of the second I.F.amplifier was amplified in four identical stages, each having a gain of 7, and tuned at 100 KHz. Output amplitude of each stage was limited to 5 V using zener diodes.

Fig. 5.7 gives the circuit diagram of the amplifiers (tuned at 100 KHz) and the log amplifier. Input of the first amplifier, in the diagram, is the output of the second I.F amplifier. The four amplifiers, shown in the diagram, are in easecade. Tunning of the each amplifier was such that the overall band width of the 100 KHz amplifiers was about 5 KHz.

Detected output of each amplifier stage was added and amplified using a logarithimic amplifier. The log amplifier output was telemetered in the voltage range of 0 to 5V.

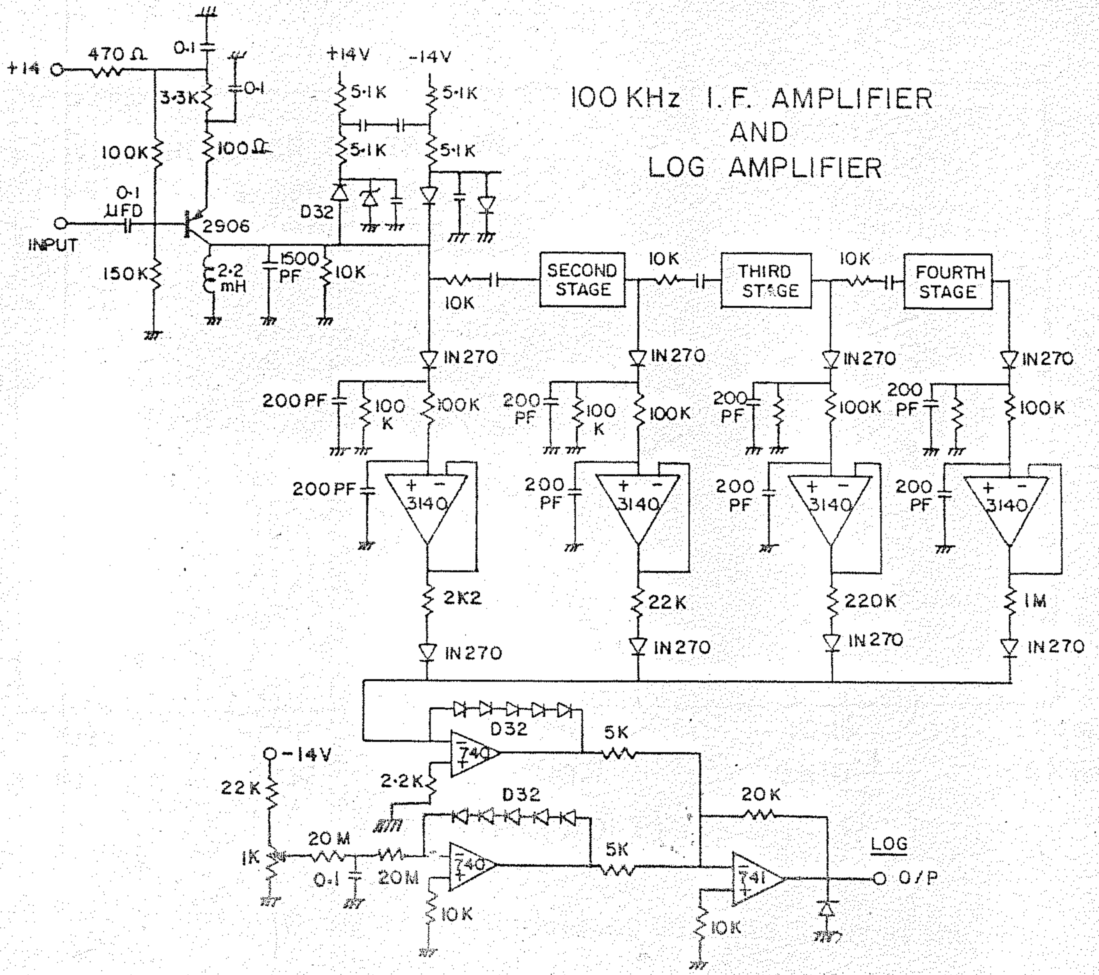

100 KHz I.F. AMPLIFIER AND LOG AMPLIFIER

Fig. 5.7

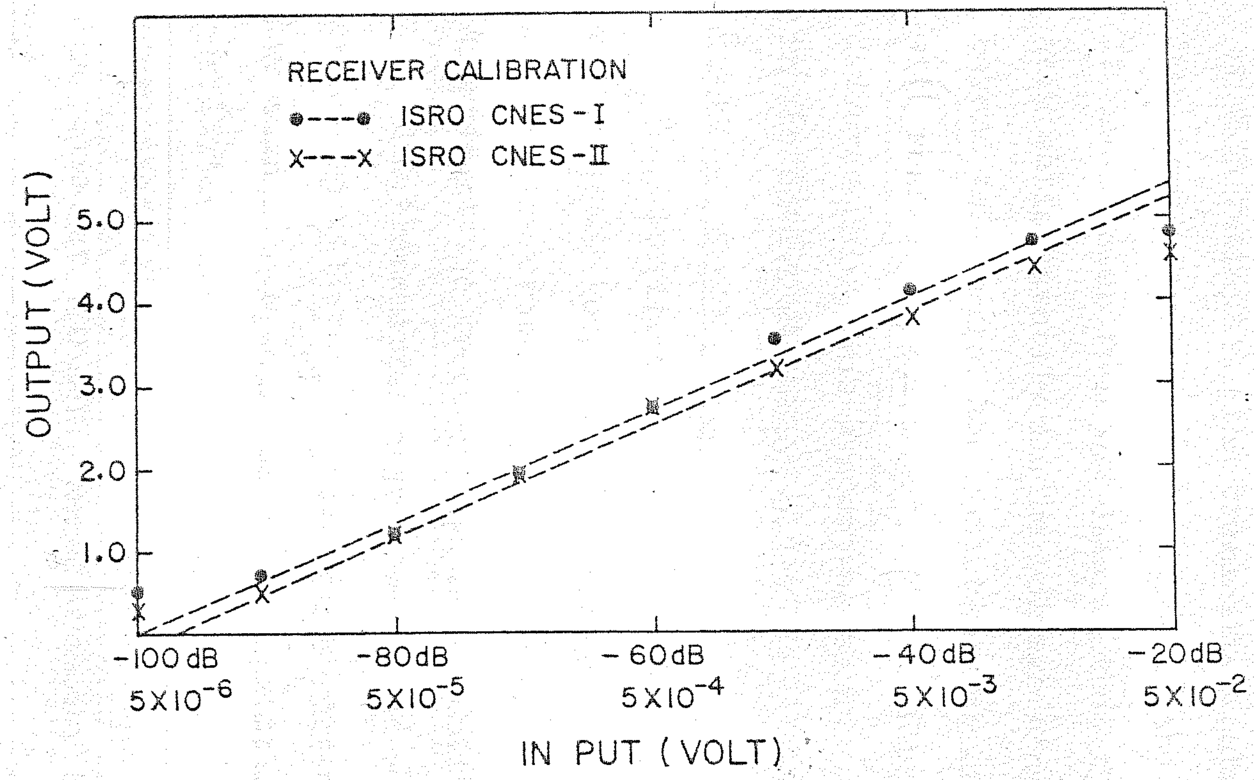

Fig. 5.8: Variation of log amplifier output with the input at the preamplifier.

Fig.5.8 gives the overall receiver performance of the payloads flown. In this diagram, the output of the log amplifier is plotted against the signal at the input point of the preamplifier. The dB level of the input signal at the preamplifier is with respect to the transmitter output (0.5 V peak to peak). The signal level, corresponding to the dB level is also given. It can be seen from the diagram that the log amplifier worked very satisfactorily in the voltage range of 10 μV to 25 mV. Beyond this range, the output is not linear (on a log scale) with respect to the input. The minimum signal which could be detected using this system was about 8 μV , as the noise level in the output was about 0.2 V d.c.

5.6.3 Frequency marker circuit:

To identify the frequency at which various resonances occur, the receiver output was calibrated using a set of frequency markers, generated by a frequency marker circuit. The block diagram of the frequency marker circuit is also shown in fig.5.6.

The transmitter signal was mixed with the output of a crystal oscillator, oscillating at 1.2 MHz. Mixing of these two signals was achieved by feeding transmitter and the crystal oscillator outputs at the base and emitter respectively, of a transistor. The transistor had a tank circuit in the collector arm, tuned at 100 KHz. Hence whenever the difference between the two signals was 100 KHz, it was preferentially amplified. The mixer output was detected, d c amplified and telemetered.

The dc output contained spikes whenever the difference in two signals was 100 KHz. To generate a large number of frequency markers, both the oscillator and transmitter outputs were overdriven in the mixer.

The frequency at which a marker is obtained, can be calculated using the relation

$$n f_1 - m f_2 = \pm 0 \cdot 1 \qquad (12)$$

where n and m are integers, and f_1 and f_2 are the transmitter and crystal oscillator frequencies respectively, in MHz. Hence we get

$$f_1 = (m f_2 \pm 0 \cdot 1)/n \qquad (13)$$

If n = 1 and m = 1, 2, 3, 4, 5,... The markers occur at

f_1 = 1.2 ± 0.1, 2.4 ± 0.1, 3.6 ± 0.1, 4.8 ± 0.1, 6.0 ± 0.1

If n = 2 and m = 1, 2, 3, 4, 5,... The markers occur at

f_1 = 0.6 ± 0.05, 1.2 ± 0.05, 1.8 ± 0.05, 2.4 ± 0.05, 3.0 ±0.05

5.7 Data Analysis

The real time data was recorded on a paper chart, running at a speed of 10 inch/sec.

The data analysis technique of Langmuir probe has been discussed in detail by Sinha (1976). For the purpose of obtaining the electron density profile from the LP data, the LP output was read at every one second interval for both the flights. Since the electron density varies by more than four orders of magnitude in the altitude range of interest, the LP system was provided with different feed back resistances for predetermined ranges of the input current. The information about these values of resistances for various input currents was telemetered, together with the LP output, on a different telemetry channel. These "gain levels" were used to obtain the current to the LP.

The electron density, from the observations of the MAP, was determined by calculating the plasma frequency from the observations of the resonance at the upper hybrid frequency using the relation

$$f_T^2 = f_P^2 + f_H^2 \qquad (14)$$

Thus the electron density was calculated using the relation

$$N_e = 1\cdot24\, f_H^2 \; ; \; f_H \simeq 1\,\mathrm{MHz},\; N_e = 1\cdot24(f_T^2 - 1\cdot0) \qquad (15)$$

The frequency of the upper hybrid resonance was determined using the frequency calibration, telemetered on a different channel. The main frequency markers were obtained at frequencies 0.6 ± 0.05, 1.8 ± 0.05, 3.0 ± 0.05, 4.2 ± 0.05 and 1.2 ± 0.1, 2.4 ± 0.1, 3.6 ± 0.1, 4.8 ± 0.1, 6.0 ± 0.1. All the frequencies are in MHz.

Fig.5.9 shows the frequency calibration for both the flights. The abscissa in the diagram is the frequency in MHz while the ordinate is the distance of the centre of a pair of markers, with respect to the centre of the marker around 0.6 MHz. Since $f_H = 1\,\mathrm{MHz}$, the f_T resonance was always at a frequency, above 1.2 MHz. [illegible]

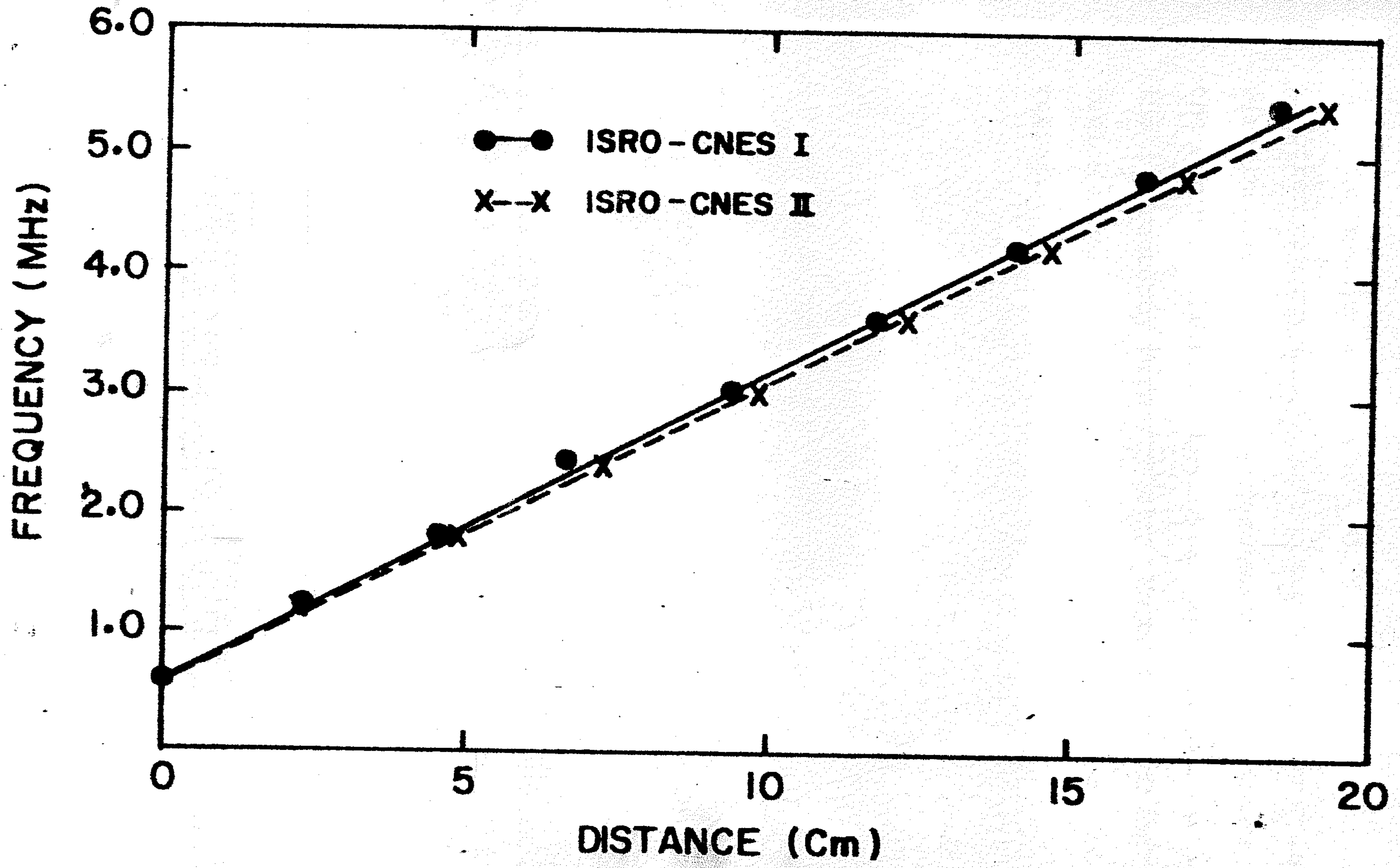

FIG. 5.9. FREQUENCY CALIBRATION. DISTANCE OF THE CENTRE OF THE MAIN MARKERS IS MEASURED FROM THE CENTRE OF THE MARKERS AT 0.6 MHz

The reading error was ± 0. 5 mm. Hence the error in electron density determination due to this error is variable with the frequency of f_T resonance. If f_T occurs at 4.0 MHz, the error in electron density is about 0.8 %. While it 4% if the f_T frequency were 1.5 MHz. Hence in the D and lower E region errors are larger compared to that above 100 km altitude region.

5.8 Results and Discussion :

The first rocket (ISRO No.05.55) carrying Langmuir Probe, mutual admittance probe and the self oscillating probe was launched on August 25, 1979 at 1151 hrs IST. The second rocket (ISRO No. 05.56) with the same payloads was launched on August 31, 1979 at 1121 hrs IST. The L.P and MAP were exposed to the medium at an altitude of about 65 km after the nose cone ejection and made uninterrupted, simultaneous measurements till the rocket tumbled.

The MAP detected several resonance features during the course of the rocket flight. The principal resonance observed in the experiment was identified with the upper hybrid resonance as per the considerations mentioned by Rao and Prakash (1977). The various resonance features were nearly identical in both the flights and hence an account of these is given for the first flight only. Also for the purpose of clarity, we shall discuss the observations of the f_T resonance from the rocket apogee and downwards.

The principal resonance, identified as f_T, was observed from the rocket apogee down to an altitude of about 137 km. Its shape was consistently same throughout this altitude range. Thereafter, another resonance feature started developing on the higher frequency side of the f_T resonance. At about 131.0 km, the two resonance became of equal magnitude. The f_T resonance was identified from its shape in the higher altitude region.

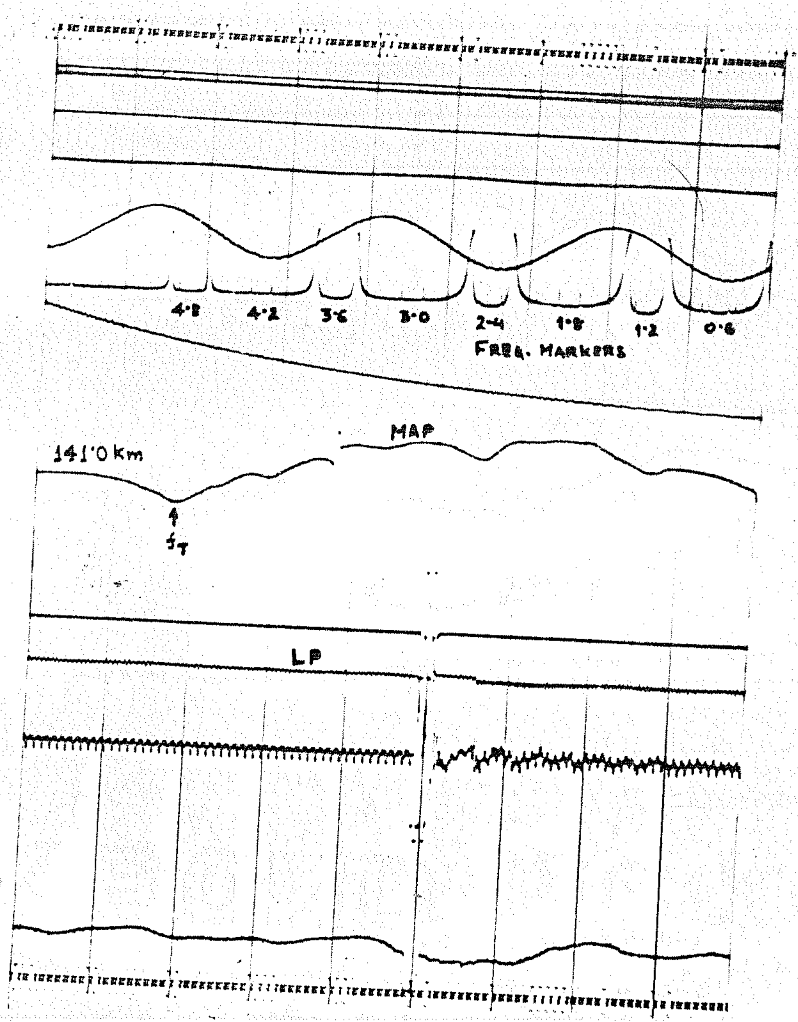

FIG. 5·10

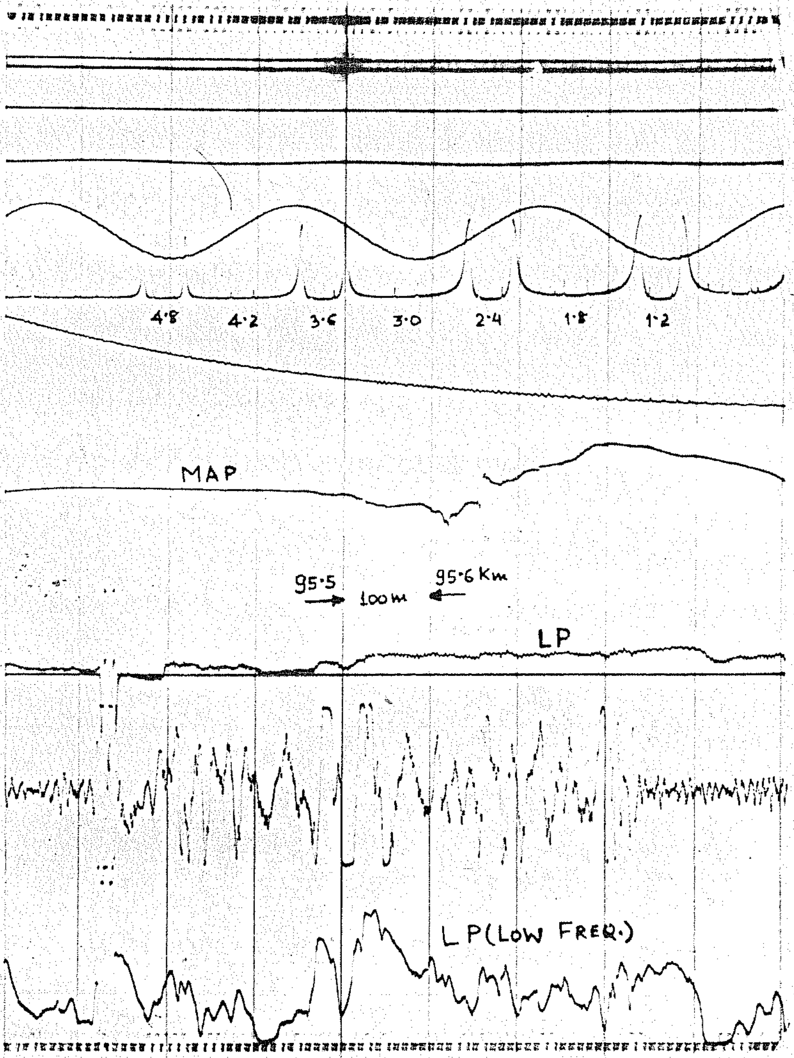

FIG. 5·11

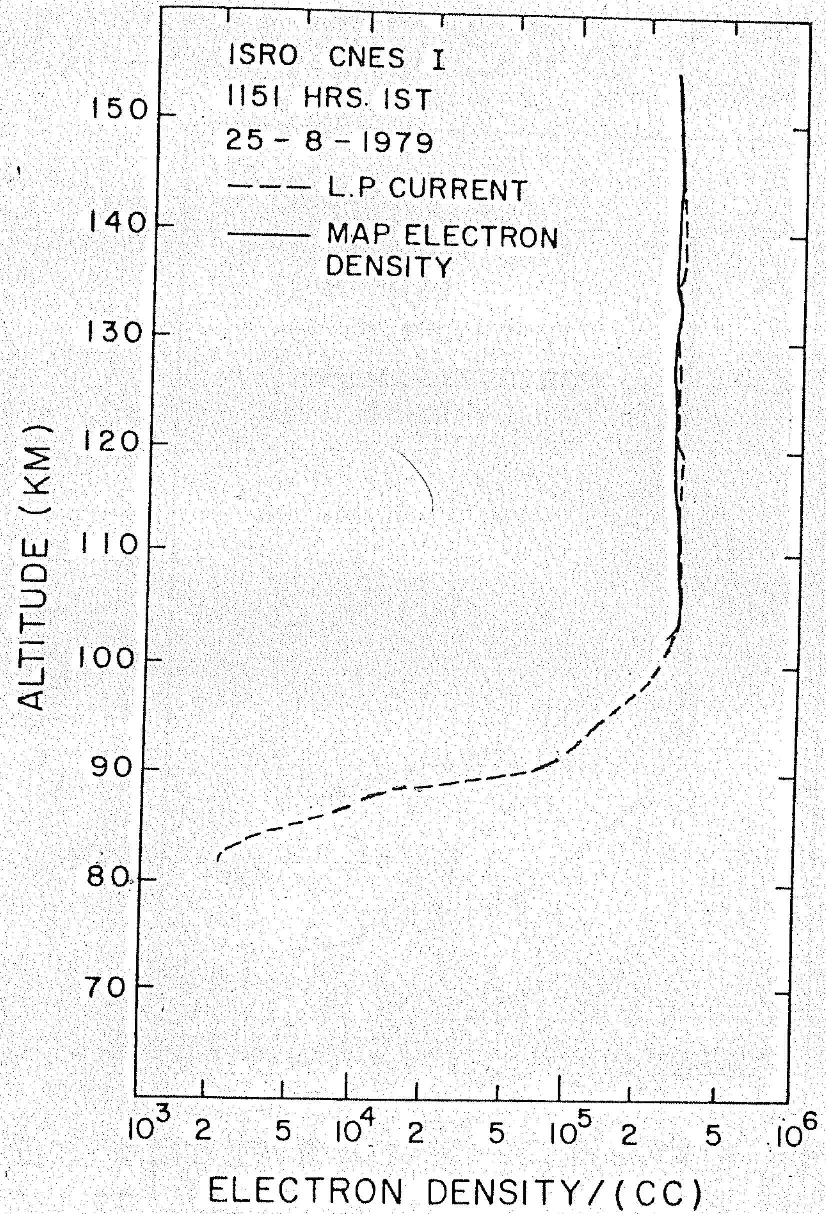
ISRO CNES I
1151 HRS. IST
25 - 8 - 1979
L.P CURRENT
MAP ELECTRON DENSITY
ALTITUDE (KM)
150
140
130
120
110
100
90
80
70
10^3
2
5
10^4
2
5
10^5
2
5
10^6
ELECTRON DENSITY/(CC)

FIG. 5·12

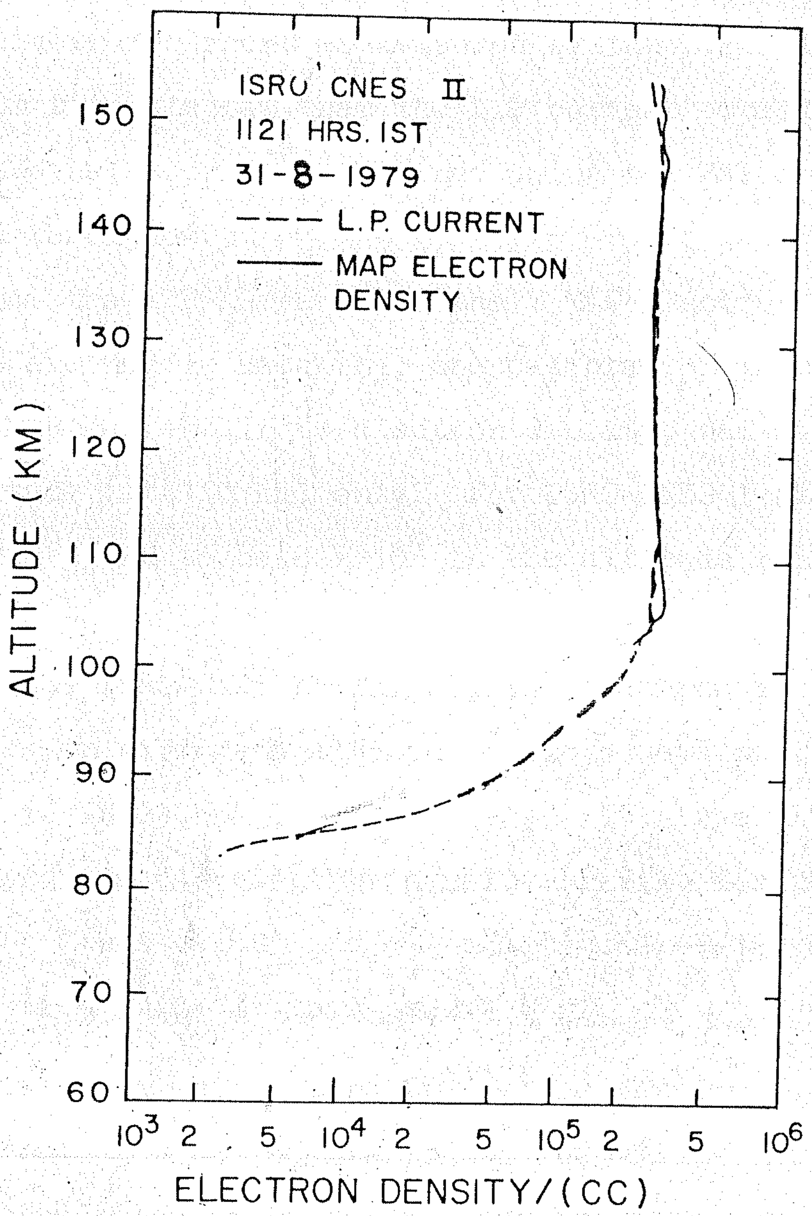
ISRO CNES II
1121 HRS. IST
31-8-1979
L.P. CURRENT
MAP ELECTRON DENSITY
ALTITUDE (KM)
150
140
130
120
110
100
90
80
70
60
10^3
2
5
10^4
2
5
10^5
2
5
10^6
ELECTRON DENSITY/(CC)

FIG. 5.13

above 108.0 km altitude using the frequency of the f_T resonance. Fig.5.12 gives the electron density profile (solid curve) as obtained from the MAP measurements. Dashed curve in the diagram is the electron current as measured by the L.P. It can be seen from this diagram that the L.P current profile and the electron density profile obtained using the MAP are identical in shape throughout.

Since the L P current and the MAP electron density profiles are nearly matching, the calibration factor K, to convert L P current in to electron density, was calculated at one altitude (at 110 km) only. For ISRO-CNES I flight, the factor was found to be 8 x 10^9 in the altitude range 100 to 155 km.

For the ISRO-CNES II flight, the features of the f_T resonances in different altitude regions were nearly similar as observed in ISRO-CNES I flight. Fig.5.13 gives the L P electron current and the MAP electron density profile for this flight. The factor K was calculated at an altitude of 120 km and was found to be 9 x 10^9 in this case.

Since the electron density profile obtained using the MAP does not show any scattering of the values, identification of the f_T resonance using the MAP has been consistent. Hence the MAP is quite suitable for the measurements of electron density in the E region.

CHAPTER VI

SUMMARY

In this chapter we give the summary of the work presented in this thesis and also the direction of future research work.

Theoretical studies:

Theoretical investigations on the role of three dimensional winds of gravity wave origin, at the equator, have brought out several new features. These are

(i) The value of wave length λ_x (of the gravity wave winds), along the geomagnetic field line is very important to the development of the wind induced electric fields. For the wave parameters assumed in the calculations, it is found that above 90 km the polarization fields are substantially shorted even at the equator.

(ii) Hither to, it has not been possible to explain satisfactorily, the generation mechanism of the small scale (type Ss) irregularities measured using the rocket borne probes. These irregularities are believed to be due to the two stream plasma instability mechanism which requires a threshold value of the drift velocity of electrons relative to ions. But the in-situ studies [illegible] show that the threshold criterion was not met, yet the irregularities were observed.

It is found that the east west electric currents driven due to the gravity wave winds are a significant fraction of the main electrojet current even at the peak of the electrojet. Since the gravity wave driven currents are sinusoidal in nature, they may satisfy the threshold criterion for the excitation of the two stream plasma instability in localised regions.

(iii) The gravity wave winds can give rise to the ionization layers. Contrary to the earlier belief, the ion convergence rate in the lower E region, at the equator, is found to be larger than in the mid latitudes. However, the convergence rates are not large enough to produce the ionization layers during the daytime. Nighttime stratification of ionization can be explained satisfactorily using the gravity wave winds.

(iv) If the curvature of the geomagnetic field lines is taken into account, k_x varies rapidly with the dip angle, undergoing a change of sign. If the gravity waves are present everywhere on a given field line, the electric fields are generated mainly around the region where $k_x = 0$. In the regions away from it, the fields due to the local winds (with finite k_x) are shorted within a wave length. Thus the region around the point where $k_x = 0$ is the source region and the rest of the region of the ionosphere connected by the geomagnetic field line acts as a load to this source region.

(v) The electric fields in the source region are generated most efficiently, if the source region overlaps the region of maximum Pedersen conductivity, σ_p. Thus in the daytime when σ_p is maximum in the E region, the source of the electric field would be situated there. It is equivalent to saying that the effective dynamo is situated in the E region during the daytime. Similarly, in the nighttime, whenever is maximum in the F region, the effective dynamo is situated in the F region.

(vi) The source region electric fields can be transmitted to the other regions of the ionosphere via the geomagnetic field lines. Attenuation of electric fields during transmission is dependent on the vertical wavelength λ_Z, of the gravity waves. The attenuation increases with the decreasing λ_Z.

(vii) The gravity wave induced electric fields (GWEF) can give rise to the spread F irregularities. It is found that the gravity waves in the E region during the evening and nighttime are more suitable for the generation of spread F irregularities. Further, it is found that the growth of the irregularities due to the GWEF is linear in the initial stages and hence they grow faster than those due to the plasma instability processes. Thus they could act as a seed to the plasma instabilities which may grow faster in the latter stages.

For the lack of sufficient observations on the gravity wave winds, only model calculations could be made in this thesis. Hence there is a need to include the observed wind profiles in these calculations to have a better understanding of various physical processes operative in the ionosphere. To measure the gravity wave winds, high sensitivity incoherent backscatter and meteor trail radars are needed to be established.

To test the theories proposed in this thesis, correlative studies on the large scale electron density irregularities on a given field line, connecting E and F regions are very essential. Also, simultaneous measurements of the electric fields and the winds are very essential.

Experimental studies:

The experimental studies on the measurements of electric fields and on the performance of various techniques for the measurement of electron density have been very encouraging. The highlights of these studies are the following:

(i) The $\underline{V} \times \underline{B}$ effect arising in the electric field measurements can not be eliminated by shielding the connecting wires, from the sensors to the input of the measuring device, by the μ-metal tubes. The lucana in the logic proposed is, however not resolved.

(ii) A new arrangement of the sensors for the measurements of vertical electric field has been developed and flown successfully. The observations indicate, very clearly, that fluctuations in the vertical field are of the order of a few millivolt per meter in the electrojet region.

(iii) Comparative studies to measure the electron density, using the mutual admittance probes and the Langmuir probes show that the MAP can be used to measure the absolute electron density in the ionosphere. Hence the calibration factor, to convert the Langmuir probe current into the electron density can be calculated.

There is a need to measure the electric fields and electron density, simultaneously, in the equatorial E and F regions. Such studies will throw light on the generation mechanisms of the electron density irregularities. Power spectrum calculations of the fluctuations in the electric fields and the electron density irregularities will further our understanding of such processes.

Regions of depleted electron density (bubbles) have been proposed to explain the spread F irregularities. The electric fields inside the bubble are believed to be larger than the background fields. Measurements of the electric fields and their direction will be helpful in confirming whether the Rayleigh-Taylor plasma instability mechanism is the cause of the equatorial spread F.

We have proposed a multiprobe experiment, to be flown on a 150 km class Indian Satellite, to study the spread F phenomena. These studies are aimed at measuring the electron density irregularities (both large scale and small scale);

small and large scale electric fields both in the horizontal and vertical directions; the 6300 A^{o} air glow emissions to determine the location and orientation of the bubbles and to find roughly the location of the F region peak by determining whether the satellite is above or below it; and to measure the Mg^{+} ion concentration to study the dynamics of the E and F regions and also to study the ionization layer formation during the daytime.

REFERENCES

Alfven H and Falthammer C G (1963)

Cosmical electrodynamics (Oxford: Clarendon Press)

Anandarao B G (1976)

Geophys.Res.Lett. 3, 545

Anandarao B G, Raghavarao R and Reddi C R (1977)

J.Geophys.Res. 82, 1510

Anandarao B G, Raghavarao R, Desai J N and Haerendel G (1978)

J.Atoms. Terr. Phys. 40

Anderson D N and Haerendel G (1979)

J.Geophys. Res. 84, 4251

Aono Y, Hirao K and Miyazaki S (1961)

J. Radio Res. Lab. Japan 8, 441

Appleton E V (1930)

Proc.Roy.Soc. 126 A, 542

Aurby M, Blanc M, Clauvel R, Taieb C, Bowen P J, Norman K, Willmore A.P, Sayers J and Wager J H (1966)

Radio Sci 1, 170

Axford W I (1963)

J. Geophys. Res. 68, 769

Axford W I and Cunnold D M (1966)

Radio Sci 1, 191

Balsley B B (1967)

Ph.D Thesis, Tech. Memorandum, IERTM, ESSA, USA, ITSA-89

Balsley B B (1969)

J.Geophys. Res. 74, 2333

Balsley B B and Ecklund W I (1972)
J.Geophys. Res. 77, 4746

Beer T (1974)
Atmospheric Waves (London: Adam Hilger)

Beer T and Moorcroft D R (1972)
J.Atoms, Terr. Phys. 34, 2045

Beghin C, Berthelier J J, Covinher J, Debrie R, Hemlin M, Renard C, Gonfalone A, Ivanov Y F, Pokhunov A A, Teslenko V P and Tubinov G F (1976)
Space Res. XVI

Berkner L V and Wells H W (1934)
Terr. Magn. Atmos. Elec. 39, 215

Biondi M A (1964)
Ann. Geophys. 20, 34

Booker H G (1979)
J.Atoms. Terr. Phys. 41, 501

Bowhill S A (1966)
Radio Sci. 1, 187

Briggs B H (1964)
J. Atoms. Terr. Phys. 26, 1

Calvert W (1963)
J. Geophys. Res. 68, 2591

Calvert W and Goe G B (1963)
J. Geophys. Res. 68, 6113

Carru M, Petit M and Waldteufel P (1967)

J. Atoms. Terr. Phys. 29, 351

Chandra H and Rastogi R G (1972)

Annls. Geophys. 28, 709

Charney J G and Drazin P G (1961)

J. Geophys. Res. 66, 83

Chapman S and Lindzen R S (1970)

Atmospheric tides, D. Reidel, Hingham, Mass.

Chimonas G and Axford WI (1968)

J. Geophys. Res. 73, 111

Chiu Y T and Strauss J M (1979)

J. Geophys. Res. 84, 3283

Clemesha B R and Wright R W H (1966)

Spread F and its effects upon radiowave propagation and communication ed. P. Newman, Technivision, Maidenhead, England.

Cohen R and Bowles K L (1963)

J. Res. N. B. S 47, 459

Crochet M, Poman C and Hanuise C (1976)

Geophys. Res. Lett. 3, 673

Dagg M (1957)

J. Atoms. Terr. Phys. 11, 139

D' Angelo N (1973)

J. Geophys. Res. 78, 3987

Davis T N, Burrows K and Stolarik J D (1967)

J. Geophys. Res. 72, 1845

Dungey J W (1956)

J. Atoms. Terr. Phys. 8, 39

Dungey J W (1959)

J. Geophys. Res. 64, 2188

Dyson P.L (1967)

J. Atoms. Terr. Phys. 29, 881

Dyson P L and Benson R F (1978)

Geophys. Res. Lett. 5, 795

Egan R D (1960)

J. Geophys. Res. 68, 2343

Elford W G (1959)

Planet. Spa. Sci. 1, 94

Evans J V (1978)

Rev. Geophys. Spa. Phys. 16, 195

Evans J V and Salah J E (1975)

Trans. Am. Geophys. Union, EOS 56, 412

Falheson U V (1967)

Space Sci. Rev. 7, 238

Falheson U V, Kelley M C and Mozer F S (1970)

Planet. Spa. Sci. 18, 1551

Farley D T (1959)

Cornell Univ. Res. Rep. EE 454

Farley D T (1960)

J.Geophys. Res. 65, 869

Farley D T (1963)

J. Geophys. Res. 68, 6083

Farley D T, Balsley B B, Woodman R F and McClure J P (1970)

J. Geophys. Res. 75, 7199

Fejer B G, Farley D T, Balsley B B and Woodman R F (1975)

J. Geophys. Res. 80, 1313

Fejer J A (1965)

Physics of the earth's upper atmosphere, eds.Hines C O and Colleagues, Prentice-Hall, Englewood Cliffs, N.J

Fejer J A and Calvert W (1964)

J. Geophys. Res. 69, 5049

Fellous J L, Bernard R, Glass M, Massebeuf M and Spizzichino A (1975)

J. Atoms. Terr. Phys. 37, 1511

Forbes J M and Garrett H B (1976)

J. Atoms. Sci. 33, 2226

Forbes J M and Lindzen R S (1976)

J. Atoms. Terr. Phys. 38, 897

Francis S H (1973)

J. Geophys. Res 78, 2278

Francis S H (1975)

J. Atoms. Terr. Phys. 37, 1011

Geisler J E (1966)

J. Atoms. Terr. Phys. 28, 703

Geisler J E (1967)

J. Atoms. Terr. Phys. 29, 1469

Glass M and Spizzichino A (1974)

J. Atoms. Terr. Phys. 36, 1825

Greenhow J S and Neufeld E L (1956)
Phil. Mag. 1, 1157

Greenhow J S and Neufeld E L (1961)
Quart. J. R. Met. Soc. 87, 472

Groves G V (1969)
J. Brit. Interplanet. Soc. 22, 285

Gupta S P (1970)
Ph.D thesis, Gujarat Univ. India

Hanson W B and Sanatani S (1971)
J. Geophys. Res. 76, 7761

Hanuise C and Crochet M (1977)
J. Atoms. Terr. Phys. 39, 1097

Hanuise C and Crochet M (1978)
J. Atoms. Terr. Phys. 40, 49

Hanrwitz B (1956)
Meteorol Pap. 2, New York Univ. New York

Herman J R (1966)
Rev. Geophys. 4, 255

Heikkila W J, Eaker N, Fejer J A, Tipple K R, HugillJ, Schneible D E and Calvert W (1968)
J. Geophys. Res. 73, 3511

Hines C O (1960)
Can. J. Phys. 38, 1441

Hines C O (1963)
Quart. J. Roy. Meteorol.Soc. 89, 1

Hines C O (1964)

J. Geophys. Res. 69, 1018

Hines C O (1974)

Upper Atmosphere in Motion, American Geophys. Union, Washington D.C

Hoh F C (1963)

Phys. Fluids 6, 1184

Hong S S and Lindzen R S (1976)

J. Atoms. Soi. 33, 135

Hooke W H (1969)

Planet Space. Sci. 17, 749

Kato S (1965)

Space Sci. Rev. 4, 223

Kato S (1966)

J. Geophys. Res. 71, 3201

Kato S (1973)

J. Geophys. Res. 78, 757

Kato S, Reddy C A and Matsushita S (1968)

Paper presented at the II seminar on the cause and structure of Temperate-Lalitude Sporadic E, voil, Colorado

Kaw P K (1972)

J. Geophys. Res. 77, 1323

Kelley M C, Haerendel G, Kappler H, Valenzula A, Balsley B B, Carter D A, Ecklund W L, Carlson C W, Hausler B and Torbert R (1976)

Geophys. Res. Lett. 3, 448

Kelvin W H (1882)

Proc. Roy. Soc. Edinburgh 11, 396

Klostermeyer J (1978)

J. Geophys. Res. 83, 3753

Knetch R W and Schlitt D W (1961)

Ann. IGY, 11, 213

Knox F B (1964)

J. Atoms. Terr. Phys. 26, 239

Kochanski A (1966)

Mon. Weather Rev. 94, 199

Kochanski A (1973)

Ann. Geophys. 29, 77

Kohl H and King J W (1967)

J. Atoms. Terr. Phys. 29, 1045

Lamb H (1910)

Proc. Roy. Soc. Ser. A 84, 551

Layzer D J (1964)

J. Geophys. Res. 69, 1853

Lee K, Kennel C F and Coroniti F V (1974)

J. Geophys. Res. 79, 249

Lindzen R S (1967)

Quart. J. Roy. Meteorol Soc. 93, 18

Lindzen R S (1974)

In structure and Dynamics of the upper atmosphere ed. Franco Verniani, Elsevier scientific publishing Company, Amsterdam, Oxford, New York

Lindzen R S and Hong S S (1974)

J. Atoms. Sci. 31, 1421

Lysenko A I et al (1972)

J. Atoms. Terr. Phys. 34, 1435

Mac Leod M A (1966)

J. Atoms. Sci. 23, 96

Maeda K, Tsuda K and Maeda H (1963)

Phys. Rev. Lett, 11, 406

Martyn D F (1955)

in physics of the ionosphere, physical soc.London, 163.

Martyn D F (1959)

J. Geophys. Res. 64, 2178

Matsushita S (1951)

J. Geomag. Geoelec. 3, 44

Maynard N C (1967)

J. Geophys. Res. 72, 1863

Maynard N C, Cahill L J and Sastry T S G (1965)

J. Geophys. Res. 70, 1241

Mayr H G and Harris I (1977)

J. Geophys. Res. 82, 2628

McClure J P, Hanson W B and Hoffman J F (1977)

J. Geophys. Res. 82, 2650

Mc Donald B E, Coffey T P, Ossakow S L and Sudan R N (1974)

J. Geophys. Res. 79, 2551

Mc Donald B E, Coffey T P, Ossakow S L and Sudan R N (1975)

Radio Sci. 10, 247

Mozer F S (1968)

Small rocket instrumentation techniques, Space Res.XI, 26

Mozer F S (1972)

Space Sciences Laboratory Report, Univ.of California, Berkeley

Mozer F S and Falheson U V (1970)

Planet Space. Sci. 18, 1563

Muralikrishna P (1975)

Ph.D. thesis, Gujarat Univ. India

Murata H (1968)

Rep. Ionos. Space Res. Jap. 22, 213

Murata H (1974)

Space Sci. Rev. 16, 461

Murgatroyd R J (1957)

Quart. J. Roy. Met. Soc. 83, 417

Murphy C H, Bull G V and Edwards H D (1966)

J. Geophys. Res. 71, 4535

Ossakow S L, Zalesak S T, McDonald B E and Chaturvedi P K (1979)

J.Geophys. Res. 84, 17

Pfister W and Ulwick J C (1958)

J. Geophys. Res. 63, 315

Pitteway M L V and Hines C O (1963)

Can. Jnl. Phys. 41, 1935

Pitteway M L V and Hines C O (1965)

Can. Jnl. Phys. 43, 2222

Prakash S (1981)

Private Communication

Prakash S, Gupta S P and Subbaraya B H (1970)

Planet. Space Sci. 18, 1307

Prakash S, Gupta S P, Subbaraya B H and Jain C L (1971)

Nature, 233, 56

Prakash S, Gupta S P, Subbaraya B H, Sinha H S S and Jain C L (1973)

First Lloyd V. Berkner Symposium, AGU, Univ. Texas, Dallas

Prakash S, Jain C L, Balsley B B and Greenwald R A (1974)

J. Geophys. Res. 79, 4334

Prakash S, Gupta S P, Subbaraya B H and Pandey R (1979)

Low latitude Aeronomical Processes, 8, 3

Prakash S and Pal S (1981)

Private communication

Prakash S and Pandey R (1979)

Proc. Indian Acad. Sci. 88 A, 229

Prakash S and Subbaraya B H (1967)

Rev. Sci. Inst. 38, 1132

Prakash S, Subbaraya B H and Gupta S P (1972)

Indian J. Rad. Space Phys. 1, 72

Rao T R (1981)

Ph.D thesis, to be submitted to the Gujarat Univ. India

Rao T R and Prakash S (1977)

Space Res. XVIII, 281

Rastogi P K and Bowhill S A (1975)

Aeronomy Rep No.68, Univ. Illinois, Urbana, USA

Ratcliffe J A (1972)

An introduction to the ionosphere and magnetosphere, Cambridge Univ. Press.

Rawer K (1953)

Comptes Rendus 237, 1102

Rawer K (1960)

Comptes Rendus 250, 1517

Reed R J (1967)

J.Atoms Sci. 24, 315

Reed R J, Oard M J and Sieminski M (1969)

Mon.Weather Rev. 97, 456

Reed D, Bhavsar P D, Desai J N, Gupta S P, Farmer A D and Rounce P (1976)

Space Res. 16, 407

Reddy C A and Devasia C V (1976)

Nature, 261, 396

Reddy C A and Devasia C V (1978)

Nature, 273, 195

Reid G C (1968)

J.Geophys. Res. 73, 1627

Reiger E (1971)

Gerlands Beitr. Geophysik, Leipzig, 80, 243

Richmond A D (1972)

AFCRL - 72 - 0668 Environmental Res.Paper No.421.

Richmond A D (1973)

J. Atoms. Terr. Phys. 35, 1083

Richmond A.D (1976)

J.Geophys. Res. 81, 1447

Rishbeth H (1971)

Planet. Space. Sci. 19, 357

Rishbeth H and Garriott O K (1969)

Introduction to Ionospheric Physics, Academic Press, New York.

Rogister A (1971)

J. Geophys. Res. 76, 7754

Rogister A and D'Angelo N (1970)

J. Geophys. Res. 75, 3879

Rosenberg N W and Edwards H D (1964)

J. Geophys. Res. 69, 2819

Rottger J (1976)

J. Atoms. Terr. Phys. 38, 97

Salah J E, Wand R H and Bernard R (1975)

Radio Sci. 10, 347

Sampath S (1976)

Ph.D Thesis, Gujarat University, India.

Sampath S and Sastry T S G (1979)

J. Geomag. Geoelec. 31, 391.

Sartiel J (1972)

Service d' Aeronomie, C.N.R.S (France) Internel Report No. 30 G.

Sastry T S G (1970)

Space Res. 10, 778

Sato T (1972)

Phys. Rev. Lett. 28, 732.

Scannapieco A J and Ossakow S L (1976)

Geophys. Res. Lett. 3, 451

Schieldge J P, Venkateswaran S V and Richmond A D (1973)

J. Atoms. Terr. Phys. 35, 1045

Schuster A (1908)

Phil. Trans. Roy. Soc. London, A 208, 163

Shimazaki T (1959)

J. Radio Res. Labs. Japan 6, 669

Simon A (1963)

Phys. Fluids, 6, 382

Singleton D G (1960)

J. Geophys. Res. 65, 3615

Singleton D G (1962)

J. Atoms. Terr. Phys. 24, 871

Singleton D G (1968)

J. Geophys. Res. 73, 295

Singer S F, Maple E and Bowen W A (1951)

J. Geophys. Res. 56, 265

Sinha H S S (1976)

Ph.D thesis, Gujarat Univ., India

Sleeper A M and Weinstock J (1972)

Phys. Fluids. 15, 1507

Smith E K (1957)

N B S Circ. 582

Smith E K (1966)

Radio Sci. 1, 129

Smith L G and Mechtly (1972)

Radio Sci. 7, 367

Spizzichino A (1970)

Ann. Geophys. 26, 9, 25

Spreiter J R and Briggs B R (1961)

J. Geophys. Res. 66, 2345

Sprenger K, Greisiger K M and S[illegible]inder R (1971)

Izv. Acad. Sci. USSR. Atoms. Oceanic Phys. English Trans. 7, 479.

Stening R J (1970)

Planet.Spa.Sci. 18, 121

Stewart B (1882)

Encyclopedia Britannica, 9th ed. 16, 159

Subbaraya B H, Muralikrishna P, Sastry T S G and Prakash S (1972)

Planet. Space. Sci. 20, 47

Sudan R N, Akinrimisi J and Farley D T (1973)

J. Geophys. Res. 78, 240

Sudan R N and Keskinen M (1977)

Phys. Rev. Lett. 38, 966

Suguira M and Cain C J (1966)

J. Geophys. Res. 71, 1869

Suguira M and Poros D J (1969)
J. Geophys. Res. 74, 4025

Szuszczewicz E P (1978)
J. Geophys. Res. 83, 2665

Tarpley J D (1970)
Planet. Spa. Sci. 18, 1091

Tsuda T, Sato T, Maeda K (1966)
Radio Sci. 1, 212

Untiedt J (1967)
J. Geophys. Res. 72, 5799

Volland H and Mayr H G (1972)
J. Atoms. Terr. Phys. 34, 1745; 1769

Volland H and Mayr H G (1977)
Rev. Geophys. Space Phys. 15, 203

Wand R H (1976)
Radio Sci. 11, 641

Weinstock J and Sleeper A M (1972)
J. Geophys. Res. 77, 3621

Whitehead J D (1961)
J. Atom. Terr. Phys. 20, 49

Whitehead J D (1970)
Rev. Geophys. Space Phys. 8, 65

Whitehead J D (1971)
J. Geophys. Res. 76, 238

Woodman R F and Hagfors T (1969)

J. Geophys. Res. 74, 1205

Woodman R F and LaHoz C (1976)

J. Geophys. Res. 81, 5447

Zimmerman S P (1964)

J. Geophys. Res. 69, 784

Crochet M (1977)

J. Atoms. Terr. Phys. 39, 1103

Prakash S, Subbaraya B H, Pal S and Pandey R (1981)

To be presented at URSI meeting.